



National Library
of Canada

Bibliothèque nationale
du Canada

Canadian Theses Service Service des thèses canadiennes

Ottawa, Canada
K1A 0N4

NOTICE

The quality of this microform is heavily dependent upon the quality of the original thesis submitted for microfilming. Every effort has been made to ensure the highest quality of reproduction possible.

If pages are missing, contact the university which granted the degree.

Some pages may have indistinct print especially if the original pages were typed with a poor typewriter ribbon or if the university sent us an inferior photocopy.

Reproduction in full or in part of this microform is governed by the Canadian Copyright Act, R.S.C. 1970, c. C-30, and subsequent amendments.

AVIS

La qualité de ce microforme dépend grandement de la qualité de la thèse soumise au microfilmage. Nous avons tout fait pour assurer une qualité supérieure de reproduction.

S'il manque des pages, veuillez communiquer avec l'université qui a conféré le grade.

La qualité d'impression de certaines pages peut laisser à désirer, surtout si les pages originales ont été dactylographiées à l'aide d'un ruban usé ou si l'université nous a fait parvenir une photocopie de qualité inférieure.

La reproduction, même partielle, de cette microforme est soumise à la Loi canadienne sur le droit d'auteur, SRC 1970, c. C-30, et ses amendements subséquents.

UNIVERSITY OF ALBERTA

**A High Speed Optical Data Bus Using
Modified Orthogonal Subcarrier Multiplexing**

by



Kevin P. Benterud

A thesis submitted to the Faculty of Graduate Studies and Research in partial
fulfillment of the requirements for the degree of
Master of Science

Department of Electrical Engineering

Edmonton, Alberta
Spring, 1991



National Library
of Canada

Bibliothèque nationale
du Canada

Canadian Theses Service Service des thèses canadiennes

Ottawa, Canada
K1A 0N4

The author has granted an irrevocable non-exclusive licence allowing the National Library of Canada to reproduce, loan, distribute or sell copies of his/her thesis by any means and in any form or format, making this thesis available to interested persons.

The author retains ownership of the copyright in his/her thesis. Neither the thesis nor substantial extracts from it may be printed or otherwise reproduced without his/her permission.

L'auteur a accordé une licence irrévocable et non exclusive permettant à la Bibliothèque nationale du Canada de reproduire, prêter, distribuer ou vendre des copies de sa thèse de quelque manière et sous quelque forme que ce soit pour mettre des exemplaires de cette thèse à la disposition des personnes intéressées.

L'auteur conserve la propriété du droit d'auteur qui protège sa thèse. Ni la thèse ni des extraits substantiels de celle-ci ne doivent être imprimés ou autrement reproduits sans son autorisation.

ISBN 0-315-66679-X

Canada

UNIVERSITY OF ALBERTA

RELEASE FORM

NAME OF AUTHOR: Kevin P. Benterud

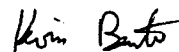
TITLE OF THESIS: A High Speed Optical Data Bus Using Modified
Orthogonal Subcarrier Multiplexing

DEGREE: Master of Science

YEAR GRANTED: 1991

Permission is hereby granted to THE UNIVERSITY OF ALBERTA LIBRARY to reproduce single copies of the thesis and to lend or sell such copies for private, scholarly, or scientific research purposes only.

The author reserves other publication rights, and neither the thesis nor extensive extracts from it may be printed or otherwise reproduced without the author's written permission.



1740 - 36 Street
Edmonton, Alberta
T6L 2P5

Date: 20 DEC 1990

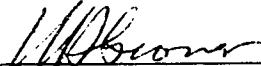
THE UNIVERSITY OF ALBERTA

FACULTY OF GRADUATE STUDIES AND RESEARCH

The undersigned certify that they have read, and recommend to the Faculty of Graduate Studies and Research for acceptance, a thesis entitled **A High Speed Optical Data Bus Using Modified Orthogonal Subcarrier Multiplexing** submitted by **Kevin P. Benterud** in partial fulfillment of the requirements for the degree of **Master of Science**.

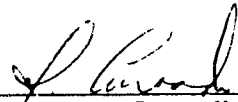


Dr. W. A. Krzymien



Dr. W. D. Grover

Supervisors



Dr. J. Conradi



Dr. A. Basu

Date: 20 Dec. 1990

Abstract

This thesis introduces the technique of modified orthogonal subcarrier multiplexing and estimates capacity of a fibre optic system which uses the technique to extend a computer bus. Modified orthogonal subcarrier multiplexing permits the technique of subcarrier multiplexing to be implemented with simple pulse shapes and does not require guard bands between channels. This technique is moderately complex and attains bandwidth efficiencies of 1 to 2 bit/s/Hz. Transmission capacities for different modified orthogonally multiplexed implementations are estimated by simulating the composite broadband signal in the presence of laser resonance distortion by an eye diagram analysis, and performing BER calculations with expected levels of noise in the worst case. Results indicate that 10 Gbit/s of data may be transported with a BER < 10^{-12} on a single digital subcarrier multiplexed (SCM) optical link over a 100 m distance if a reduction in laser relative intensity noise (RIN) from -140 dB/Hz to -155 dB/Hz is achieved.

The thesis begins by describing the problem of extending the complete bus of a computer through a distance of 100 m and why a solution was sought using digital SCM. The signal impairments of noise and distortion introduced by the analog fibre optic link are then discussed, and techniques of modelling them in the worst case are presented in Chapter 2. Resonance distortion for a modern SCM laser was modelled by numerically solving the laser rate equations. Maximum laser relative intensity noise (RIN) level of -140 dB/Hz was assumed. In order to achieve the required data rate of 20 Gbit/s in this transmission medium, the technique of orthogonal multiplexing was considered. The principles of this technique are discussed in Chapter 3. A modification of allowing simple baseband pulse shaping was introduced and caused some received signal degradation, but allowed it to be suitable for a multiGbit/s application. The performance of different modified orthogonal subcarrier multiplexed implementations is then considered in Chapter 4, first in an ideal transmission medium, then in the presence of signal degradations introduced by laser resonance distortion and expected levels of system noise. Modified orthogonal subcarrier multiplexing appears to be a technique suitable for the multiGHz band available on modern analog fibre optic links, and is more bandwidth efficient than current techniques being employed.

ACKNOWLEDGEMENTS

I would like to thank the following people and institutions for their contributions to this work:

- Drs. W. A. Krzymien and W. D. Grover for proposing and supervising this project,
- the members of the examining committee, for taking time to review this work,
- Dr. Erick Thomson and Mr. Rick Neumann of DEC Canada for stimulating discussions and useful comments on this thesis,
- Mr. George Fraser for introducing me to this project,
- Mr. Darrell Barabash for many fruitful discussions related to this project,
- Dr. R. I. MacDonald for allowing me access to his optical devices and laboratory facilities from which I gained insight required for modelling the optical link,
- the Alberta Telecommunications Research Centre, its sponsors and Dr. W. A. Krzymien for financial assistance,
- the Alberta Telecommunications Research Centre and its staff and students for an environment in which this work could be carried out in an efficient manner,
- Tom, Chris, Jennifer and Robert Lavigne for their constant support and encouragement through the writing of this thesis,
- my family, and in particular my mother who has stood unwavering in support and love,

and more importantly, Miss Wanda Leonard, without whose prayers, patience, support and encouragement, this work would never have been completed. I most importantly want to thank The Engineer Himself, for giving me the key to unlocking a new truth in His creation.

A SPECIAL DEDICATION

I dedicate this thesis to my father, the late Ragnvald O. Benterud, who taught me the character I needed to complete this work.

Table of Contents

Chapter 1	Introduction.....	1
1.1	The Problem.....	2
1.2	Lightwave Subcarrier Multiplexing	4
1.2.1	Applications of Lightwave SCM to Microwave Engineering	5
1.2.2	Broad-Band Distribution Using Lightwave SCM	5
1.2.3	Digital Subcarrier Multiplexing	7
1.3	Thesis Overview	9
Chapter 2	The Lightwave Link	11
2.1	Laser Characteristics and Modelling.....	14
2.1.1	Laser Distortion Characteristics.....	15
2.1.1a	Nonlinearity of the Light Power-Current Curve	17
2.1.1b	Resonance Distortion	18
2.1.2	Approach for Modelling Laser Resonance Distortion	20
2.1.2a	The Semiconductor Laser Rate Equations.....	22
2.1.2b	Resonance Frequency of Laser.....	26
2.1.3	Laser Resonance Distortion Model.....	27
2.1.4	Distortion Characteristics of Laser Model.....	35
2.1.5	Dominant Source of Distortion From Laser Model with a Fifty Channel Modified Orthogonal SCM Signal Present.....	41
2.1.6	Laser's Relative Intensity Noise Characteristics.....	45
2.2	Passive Optical Components.....	49
2.3	Summary of Noise Contributions and System Assumptions	54
Chapter 3	Modified Orthogonal Subcarrier Multiplexing Transmission Techniques for a Digital Lightwave System	57
3.1	Orthogonal Subcarrier Multiplexing	60
3.1.1	Chang's Criteria for Orthogonal SCM.....	60
3.1.2	An Orthogonal SCM-QAM System (O-QAM).....	62
3.2	Modified Orthogonal SCM	67
3.2.1	Orthogonality Analysis of Nonbandlimited Channels	68
3.2.2	Baseband Pulse Shapes Suitable for Modified Orthogonal SCM	73
3.2.2a	Half Sine Shaped Pulse.....	74
3.2.2b	Rectangular Shaped Pulse.....	75
3.2.2c	Sine Square Shaped Pulse.....	76
3.2.2d	Butterworth Low Pass Filter Shaped Pulses	77
3.3	System Implementations of Modified Orthogonal SCM	78
3.3.1	Modified Orthogonal SCM System with No Quadrature Subchannels.....	79
3.3.2	Modified O-QAM.....	81
3.4	Possible Carrier and Clock Recovery Techniques at Receiver.....	83
Chapter 4	Simulation Experiments and Results.....	85

4.1 Simulation and Performance of Modified Orthogonal SCM Signals in an Ideal Transmission Medium	87
4.1.1 Modified Orthogonal SCM Signal- No Quadrature Subchannels	88
4.1.1a Half Sine Shaped Symbols	89
4.1.1b. Rectangular Pulse Shape	93
4.1.1c. Sine Square Pulse Shape	96
4.1.1d. Butterworth Low Pass Filter Shaped Pulses	98
4.1.2 Modified O-QAM	99
4.1.2a. Half Sine Pulse Shape	100
4.1.2b. Rectangular Pulse Shape	102
4.1.3. Performance Summary of Proposed Modified Orthogonal SCM Schemes in an Ideal Transmission Medium	104
4.1.4 Eye Closure Penalties Caused by Phase Errors	105
4.1.5 Signal Statistics of Fifty Multiplexed Active Data Streams	109
4.2 Simulation and Results of Modified Orthogonal SCM Signals transmitted through the Lightwave Link	116
4.2.1 Simulation Experiments of the Digital SCM System	117
4.2.1a Method of Determining Modulation Depth (MOD)	121
4.2.1b Calculation of Signal to Noise Ratio and System Margin	122
4.2.2 Results of Simulated Transmission of Orthogonal SCM Signals on Lightwave Link	125
Chapter 5 Summary and Conclusions	132
5.1 Thesis Summary	132
5.2 Conclusions	135
5.3 Further Work	137
References	139
Appendix 1- Derivation of Received Channel Spectra	143
A1.1 Interference from a Cosine Subchannel	143
A1.2 Interference from a Sine Subchannel	144
Appendix 2- Eye Diagrams for Determining MOD	145
A2.1 Eye Diagrams with MOD= 0.20	146
A2.2 Eye Diagrams with MOD= 0.25	147
A2.3 Eye Diagrams with MOD= 0.30	148
A2.4 Eye Diagrams with MOD= 0.35	149
A2.5 Eye Diagrams with MOD= 0.40	150
Appendix 3- BOSS System Model of a 10 Gb/s Modified Orthogonal SCM Digital Lightwave Link Using Rectangular Shaped Pulses	151
A3.1 System BOSS Block Diagram, Description and Parameters	153
A3.2 Description of 10 Channel Groups in BOSS	162
A3.3 Description of Single and 5 Channel Groups in BOSS	167
A3.4 Description of Laser Model in BOSS	175
A3.4 Description of Demodulator in BOSS	179

List of Figures and Captions

Chapter 1

Figure 1.1- Block Diagram of General Digital Subcarrier Multiplexed System	8
--	---

Chapter 2

Figure 2.1- Resonance Distortion Characteristic of a Typical InGaAsP-BH Laser.....	20
Figure 2.2a- BOSS Representation of AC Laser Rate Equation Module	30
Figure 2.2b- Large Signal Laser Rate Equation Module	31
Figure 2.2c- Euler Forward Integration Module of Carrier Density Equation.....	31
Figure 2.2d- Euler Forward Integration Module of Photon Density Equation.....	32
Figure 2.3a- Current Step Response of Carrier Density	34
Figure 2.3b- Current Step Response of Photon Density	34
Figure 2.4- Frequency Response of Laser Model with $f_r = 6.7$ GHz.....	35
Figure 2.5- Time Plot of Sinusoid with Laser Clipping Distortion Introduced.....	36
Figure 2.6- Analytical and Simulated 2HD and IMD_{III-2} Characteristics for $OMD=28\%$ $f_{relax}=10$ GHz.....	38
Figure 2.7- Simulated 2HD and IMD_{III-2} Characteristics for Two OMD Levels, $OMD=14\%$ and $OMD=28\%$ $f_{relax}=6.7$ GHz.....	40
Figure 2.8- Number of IMD_{II} Products Falling in Channel Position m , Where N_m^+ are (f_1+f_2) Products, and N_m^- are (f_1-f_2) Products, and $N_{total}(f_m) = N_m^+ + N_m^-$	42
Figure 2.9- Single $IMD_{II}(f_m)$ Products Observed From Two Tone Distortion Test Simulations with $OMD = 2.83\%$ per Tone, and the Total Projected Distortion With 50 Uncorrelated Channels Spaced According to (2.30).....	44
Figure 2.10- Expected RIN Characteristic of the $1.3 \mu m$ InGaAsP-BH laser characterized by Tucker, with $f_r=10$ GHz	48
Figure 2.11- Interferometric Noise from Multiple Connector Reflections	51
 Chapter 3	
Figure 3.1- A Conventional FDM Spectrum	58
Figure 3.2- An Orthogonal SCM Spectrum.....	59
Figure 3.3- Example of a Suitable Phase Spectrum for $F(\omega)$	61
Figure 3.4- Block Diagram of an O-QAM System, Quadrature Component of Signal Encompassed by the Dashed Line.....	64

Figure 3.6- Spectrum of a Half Sine Pulse.....	74
Figure 3.7- Spectrum of Rectangular Pulse	75
Figure 3.8- Spectrum of Sine Square Pulse	76
Figure 3.9- Phase Spectrum of Three Adjacent Channels with Pulses Shaped by a Butterworth LPF, 3dB Bandwidth= 100 MHz	77
Figure 3.10a- BOSS Module, Random Source of Modulated Half Sine Shaped Pulses, No Quadrature Subchannel.....	79
Figure 3.10b- BOSS Module, Random Source of Modulated Rectangular Pulses, No Quadrature Subchannel.....	79
Figure 3.10c- BOSS Module, Random Source of Modulated Sine Square Pulses, No Quadrature Subchannel.....	80
Figure 3.10d- BOSS Module, Random Source of Modulated Low Pass Filter Pulses.....	80
Figure 3.11- BOSS Module, Demodulator of One Subchannel	80
Figure 3.12a- BOSS Module, Random Source of Modulated Half Sine Shaped Pulses, Modified O-QAM	82
Figure 3.12b- BOSS Module, Random Source of Modulated Rectangular Shaped Pulses, Modified O-QAM	82
Figure 3.12c- BOSS Module of Demodulator, Modified O-QAM.....	82
 <i>Chapter 4</i>	
Figure 4.1a- Eye Diagram for Half Sine Shaped Pulses, Centre One of Three Channels	89
Figure 4.1b- Eye Diagram for Half Sine Shaped Pulses, Single Channel Present.....	90
Figure 4.2 - Eye Diagram for Half Sine Pulse Shapes, Centre of Five Channels.....	90
Figure 4.3a- Influence of ICI and ISI on Eye Opening vs. LPF BW for 3rd, 4th and 5th Order Butterworth Filters Relative to a 3rd Order Butterworth Filter, BW= 100 MHz	91
Figure 4.3b- SNR Performance of Half Sine Shape vs. BW of 3rd, 4th and 5th Order Butterworth Filters Relative to a 3rd Order Filter, BW= 100 MHz.....	93
Figure 4.4- Eye Diagrams for Rectangular Pulse Shape, Channel with No Adjacent Channels Present and a Centre of Three Channels.....	94
Figure 4.5- Eye Diagram for Rectangular Pulse Shapes, Centre of 5 Channels.....	94
Figure 4.6- SNR Performance of Rectangular Shape Using a 3rd Order Filter vs. LPF Bandwidth, Relative to a 3rd Order Filter, Half Sine, Centre of 5 Channels.....	95
Figure 4.7- Eye Diagram of Sine Squared Pulses for Single and Three Channel Tests.....	96
Figure 4.8- Eye Diagram for Sine Square Shaped Pulses, Centre of 5 Channels.....	97

Figure 4.9- SNR Performance of Sine Square Shape vs. LPF Bandwidth, Relative to Half Sine Eye with 3rd Order 100 MHz Filter	98
Figure 4.10- Comparison of Single and Three Channel Eyes for Two Low Pass Filter Shapes (BW= 100 MHz and 200 MHz).....	99
Figure 4.11a- Eye Diagrams for Sine and Cosine Carriers, Half Sine Pulse Shape -Full Quadrature Signal Single Channel.....	101
Figure 4.11b- Eye Diagrams for Sine and Cosine Carriers, Half Sine Pulse Shape -Full Quadrature Signal, Centre of Three Channels.....	101
Figure 4.11c- Eye Diagrams for Sine and Cosine Carriers, Half Sine Pulse Shape-Full Quadrature Signal, Centre of Five Channels.....	101
Figure 4.12a- Eye Diagrams for Sine and Cosine Carriers, Rectangular Shaped Pulses-Full Quadrature Signal, Single Channel.....	103
Figure 4.12b- Eye Diagrams for Sine and Cosine Carriers, Rectangular Shaped Pulses-Full Quadrature Signal, Centre of 3 Channels	103
Figure 4.12c- Eye Diagrams for Sine and Cosine Carriers, Rectangular Shaped Pulses-Full Quadrature Signal- Centre of 5 Channels	103
Figure 4.13- ICI and ISI Penalties for Proposed Pulse Shapes of Modified Orthogonal SCM Using Butterworth LPF in the Receiver.....	104
Figure 4.14a- Eye Closure Penalty vs. Large Transmitter Carrier Phase Errors, The Centre of 5 Channels was Demodulated.....	106
Figure 4.14b- Eye Closure Penalty vs. Small Transmitter Carrier Phase Errors, The Centre of Five Channels was Demodulated.....	107
Figure 4.14c- Eye Closure Penalty vs. Receiver Local Oscillator Phase Errors, The Centre of Five Channels was Demodulated.....	107
Figure 4.15a- Simulated PDF of 50 Channel Modified Orthogonal SCM Signal Employing the Half Sine Shape with No Quadrature Subchannels Present, Overlaid PDF with the Corresponding Gaussian Distribution.....	111
Figure 4.15b- Simulated PDF of 50 Channel Modified Orthogonal SCM Signal Employing the Rectangular Shape with No Quadrature Subchannels Present, Overlaid with the Corresponding Gaussian Distribution	111
Figure 4.15c- Simulated PDF of 25 Channel Modified Orthogonal SCM Signal Employing the Half Sine Shape with Quadrature Subchannels Present, Overlaid with the Corresponding Gaussian Distribution.....	112
Figure 4.15d- Time Plot of $s(t)$ with All Data Symbols Set to a Logical One for Half Sine Shape with Quadrature Subchannels Presente	115
Figure 4.15c- Time Plot of $s(t)$ with All Data Symbols Set to a Logical One for Rectangular Shaped Symbol	115
Figure 4.16- Method of Generating Simulations of a Modified Orthogonal SCM Signal on the SCM Optical Link.....	120

Figure 4.17a- Trade Off Between Payload Size and Link Margin for Half Sine Shape, No Quadrature Component.....	127
Figure 4.17b- Worst Case Eye Diagram for Half Sine Shaped Pulses- No Quadrature Component, 10 Gbit/s.....	127
Figure 4.17c- Eye Diagram with No Laser Distortion Present- Half Sine Shape, No Quadrature Subchannels.....	127
Figure 4.18a- Trade Off Between Payload Size and Link Budget Margin for Rectangular Shape Pulses.....	128
Figure 4.18b- Worst Case Eye Diagram for Rectangular Pulse Shape, 10 Gbit/s	128
Figure 4.18c- Eye Diagram with No Laser Distortion Present-Rectangular Shape	128
Figure 4.19c- Trade Off Between Payload Size and System Margin for Half Sine Pulses, With Quadrature Component.....	129
Figure 4.19b- Worst Case Eye Diagram for Half Sine Shaped Pulses- No Quadrature Component, 10 Gbit/s.....	129
Figure 4.19c- Eye Diagram with No Laser Distortion Present-Half Sine Shape, Full Quadrature Subchannels Present.....	129
Figure 4.20d- Summary Plot of the System Margin vs. Payload Size Tradeoff.....	130
Figure 4.20e- Trade Off Between SNR and Payload Size for All Shapes.....	130
<i>Chapter 5</i>	
Figure 5.1- System Margin Gain as a Function of Laser RIN, Relative to RIN=-140 dB/Hz	136

Chapter 1

INTRODUCTION

Recent advances in silicon VLSI technology have enabled a substantial increase in operating speed of large computers. At present, clock frequencies of up to 500 MHz have been achieved with some advanced designs, and frequencies of 200 MHz are expected in the near future for commercial mainframe computers. The networking of a processor to peripherals such as the file server and printer has been adequately achieved up to now by an Ether-Net or Token-Ring type implementation. This involves one serial transmission pipe to which all peripherals have access by packetized communication. As the data rate requirements have increased, it has become considerably more difficult to provide adequate service using serial transmission. Data exchange would be much faster, if the complete parallel bus of the processor was extended to all peripherals.

Another application of physically extending the bus of a processor is to permit parallel computing with the processors distributed throughout an office environment. This would provide an efficient means of achieving a "super-computer" architecture with a number of mainframe processors distributed throughout an office building (within 100 m distance). Extension of the complete parallel bus of a computer was the motivation for pursuing the work presented in this thesis.

Chapter 1 introduces the background and approach taken to study this problem, and is organized as follows. Section 1.1 discusses the problem of extending the bus, and why lightwave subcarrier multiplexing was chosen as a transmission technique to solve it. Background is given in Section 1.2 regarding the area of lightwave SCM and how digital information may be transmitted. In Section 1.3 an overview of the thesis is presented.

1.1 THE PROBLEM

In this project we are interested in digital subcarrier multiplexing on fibre for transporting a 20 Gbit/s synchronous computer bus point to point over a 100 m distance, e.g. in an office environment. Discussed in this section is the problem of extending this bus and justification of why digital subcarrier multiplexing was chosen as the method of transmission.

Physically extending the entire computer bus is a difficult task because of the massive amount of data which is exchanged through it. For a conventional 32 bit central processing unit, a 64 bit address bus and 32 bit data bus, plus some control lines are used, resulting in 100 parallel bus lines. Operating at a bus clock frequency of 200 MHz, or a bus transmission rate of 200 Mbit/sec then yields a 20 Gbit/sec payload of parallel, synchronous data which must be transported up to 100 m away.

Transferring the data simply by physically lengthening each bus line is not feasible for distances of 100 m. Assume that each bus line is assigned a coaxial cable, cut to exactly the same length and routed to the point of interest 100 m away. To expect the transit time between channels to be within 10% of the period of one bit (0.5 nsec) for proper bus operation, is unreasonable. This would imply that the difference in time of flight between any two bus lines would be equivalent to a 10 cm long path difference. Considering only time dependent temperature difference between adjacent cables, the resulting velocity variations may cause differential delay's in the order of a bit period over a 100 m distance. Transporting the parallel data by 100 parallel transmission lines is therefore not possible since phase alignment between bus lines cannot be maintained. Therefore the parallel data must be multiplexed in some manner for the bus to be successfully transmitted.

In order to handle 20 Gbit/s of data it is necessary that fibre optic technology be used. The most obvious approach is to use conventional time division multiplexing (TDM) of the payload onto a fibre optic link. Since the total data rate is greater than 16 Gbit/sec (a recent maximum data rate published using TDM) [1] at least two parallel TDM links would be required. Assuming two links, a rate of 10 Gbit/s is needed. At present 10 Gbit/s optical systems are not commercially available, but they do exist. Alternatively ten 2 Gbit/s TDM optical links may be used since they are commercially available.

The difficulty with using more than one optical TDM link in parallel arises from each link having its own data transit time. This is due implicitly to the cascaded time division multiplexers combined with clock recovery and demultiplexing at the receiver. Bit time skew between groups of data lines then becomes difficult if not impossible to manage in a real system. As with physically extending the bus lines, the implementation difficulty arises because synchronism between bus lines cannot be maintained.

The real problem is that of multiplexing the data in a manner such that tight phase alignment is maintained between the data lines in different parallel optical links. This is important if the full payload of 20 Gb/s cannot be transported using one optical link. Alternatively then we consider multiplexing in frequency of digitally modulated signals for transmission over an analog optical fibre system, or digital lightwave subcarrier multiplexing. Since all channels are present simultaneously in the FDM signal, phase alignment is inherently maintained between all channels unless it is passed through a dispersive device or transmission medium. In that case, the medium with nonlinear group delay will cause some channels to arrive sooner or later than others, resulting in an inherent degradation of synchronism between channels. Now if the differential group delays are in the order of less than one cycle at multi-GHz range frequencies, the relative channel delays will be less than 10% of the data symbol period. This is not an unreasonable requirement for microwave devices. Therefore the use of more than one digital SCM optical link operating in parallel may provide adequate phase alignment for proper operation between

channels in different physical transmission links. Thus it appears feasible to use a number of optical SCM links in parallel, because their phase alignment may be maintained better than for a number of parallel optical links using TDM, where it is very difficult to achieve.

Another consideration is the cost of the system. Assuming that it was somehow possible to maintain synchronous data with parallel TDM optical links, presently it is very expensive to build time division multiplexers at data rates up to 10 Gbit/s. The task of multiplexing the data may be alternatively accomplished by using conventional microwave frequency division multiplexing (FDM) techniques which are well developed and use components that are less expensive. Physical and technological reasons are the reasons for seeking a solution using digital lightwave subcarrier multiplexing.

1.2 LIGHTWAVE SUBCARRIER MULTIPLEXING

We will consider in this section the background information for the area of lightwave subcarrier multiplexing (SCM). In general the term lightwave subcarrier multiplexing describes the transmission of a microwave signal which contains subcarriers modulated with either analog or digital information, via an optical carrier to one or more destination points. At the receiver, a photodiode provides direct detection of the modulated optical power and outputs an electric current directly proportional to the instantaneous optical power of the received lightwave. The optical link is therefore carrying an intensity modulated-large carrier signal, AM-LC.

There has been an interest in transmitting microwave signals directly over optical links for a number of years now. Most of the experiments and studies up to the early 1980's were geared towards military applications. Since then, considerable improvements in electro-optic components have resulted in links with over 20 GHz of direct modulation bandwidth, having high linearity and low laser relative intensity noise (RIN) [2]. The interest spurring this development forward has been its potential for many new commercial

applications. In particular a lot of effort has been put into examining this technique as a means of broad-band video and data distribution to local and metropolitan area networks [2] & [3]. This application is a very important one for the telecommunications industry and consequently most of the advances in subcarrier multiplexing technology have been directly related to or have resulted from work done towards this objective. Another significant application for SCM has been in the area of conventional microwave engineering. Its characteristic of low loss in the microwave frequency range make it ideal for transporting microwave signals to remote points in a system (signal remoting).

1.2.1 Applications of Lightwave SCM to Microwave Engineering

An interesting application of SCM has been the direct transport of microwave signals to remote antenna sites. Way et. al. in [4] showed that a C-band satellite signal could be directly transmitted through a distance of 35 km via a lightwave SCM link. Since Way's paper in 1987 more applications in this area of microwave signal remoting have emerged, particularly in radar and avionics systems. From a microwave system engineering viewpoint, lightwave SCM offers operation at very high data rates and at high radio frequencies without creating opportunities for interception and detection. The light weight and small size of the fibre optic cables allow introduction of highly redundant paths between microwave devices which improves reliability. This makes it ideal for avionic applications. Lightwave SCM also offers EMI immunity between cables, from electrical power transients and from radio frequency noise. As lightwave SCM technology continues to improve there will be further cost effective applications for it in microwave systems [5].

1.2.2 Broad-Band Distribution Using Lightwave SCM

A major objective of the telecommunications industry has been to seek a low cost means of providing broad-band distribution of voice, data, and video to local and metropolitan area networks using optical fibres. In order to justify the cost of installing

such a fibre optic network it must be commercially competitive with the existing services of copper wire plain-old-telephone-service (POTS) and the CATV network. Since the existing CATV network can provide up to 50 video channels at present, the fibre network must be able to carry at least that number along with data and voice services. The network must also be flexible enough to be upgraded to meet the advancing consumer demand for broadband services as well as any future developments in video technology such as digital or high definition video [2].

The possibility of using baseband signalling by time division multiple access (TDMA) has been examined extensively to provide this combination of services, particularly by Bellcore. It is technically possible to provide fully digital switched services, however because each uncompressed video channel requires 100 Mbit/s it results in expensive multi-gigabit/s feeders to a remote and an additional high speed transmission to each subscriber for this technique to even begin to compete with the CATV network [6].

Other recent concepts to accomplish broadband distribution include high density optical wavelength division multiplexing (WDM) [7], multichannel coherent systems [8], and subcarrier multiplexing. Subcarrier multiplexing has a number of very attractive features for broadband distribution. It supports both digital and analog transmission simultaneously. SCM takes advantage of the full bandwidth capability of single mode fibre and electro-optic components. Since all payload channels are present simultaneously without any TDM, there is great flexibility in adding new services and adapting to consumer demands [2]. The technique accesses well established and hence low cost microwave technology to multiplex and demultiplex microwave signals transmitted via the optical SCM link. Also the spectral properties of the laser are not as important as in coherent systems, so a multimode laser may be used. The major drawback with SCM however is a reduction in receiver sensitivity at the subscriber as compared with robust TDM signalling. If the user selects only a few channels at a time, narrowband low noise amplifiers may be used to increase sensitivity [9]. As a result, considerable work has been

put forward in developing SCM links to efficiently carry both analog and digital signals to the broadband subscriber.

1.2.3 Digital Subcarrier Multiplexing

Of interest to this work from the area of broadband distribution are digital SCM systems developed primarily for digital television transmission [10]-[15]. The digitally modulated microwave signal in these systems is generated by conventional FDM techniques. These techniques are now considered for our point to point transmission application that was described earlier.

The general digital subcarrier multiplexed system block diagram for our point to point transport application is shown in Figure 1.1. A description of this system is now given. The parallel bank of synchronous data streams on the left of the diagram, is divided into groups where the number of lines determines the number of levels in the digital modulation scheme. At the output of the microwave mixer, a digitally modulated microwave signal is present at the carrier frequency assigned to it. Spacing between adjacent channels is set such that acceptable levels of inter-channel interference (ICI) result. Generally this spacing involves a guard band between the main spectral lobes of adjacent channels, the size of which is determined by the type of modulation scheme and performance required.

The digitally modulated sinusoidal carriers are then scaled and summed together yielding a microwave signal. This intensity modulates the laser diode. The laser is biased at some optimal point above threshold such that there is a maximum possible signal swing between the "turn-on-knee" and "saturation" conditions of the light power-drive current characteristic. The signal swing or optical modulation depth (OMD) defined as half the ratio of the peak to peak modulated optical power to the dc optical power, is optimized to provide maximum signal power while ensuring that laser distortion does not severely limit performance. The output of the laser is then coupled into the optical fibre for transmission

to the single destination point. At the receiver the light is coupled from the fibre into a photodetector which outputs a current directly proportional to the incident light power. The current is converted to a voltage which is electrically amplified using a low noise wideband preamplifier followed by cascaded amplifiers providing necessary gain to drive the demodulation circuitry.

Each channel is then demodulated. In the system shown in Figure 1.1 homodyne downconversion is used to bring each channel directly to baseband and each channel is then low pass filtered to attenuate undesired adjacent spectral terms. A decision circuit then decides what symbol was transmitted and outputs the appropriate bit or combination of bits.

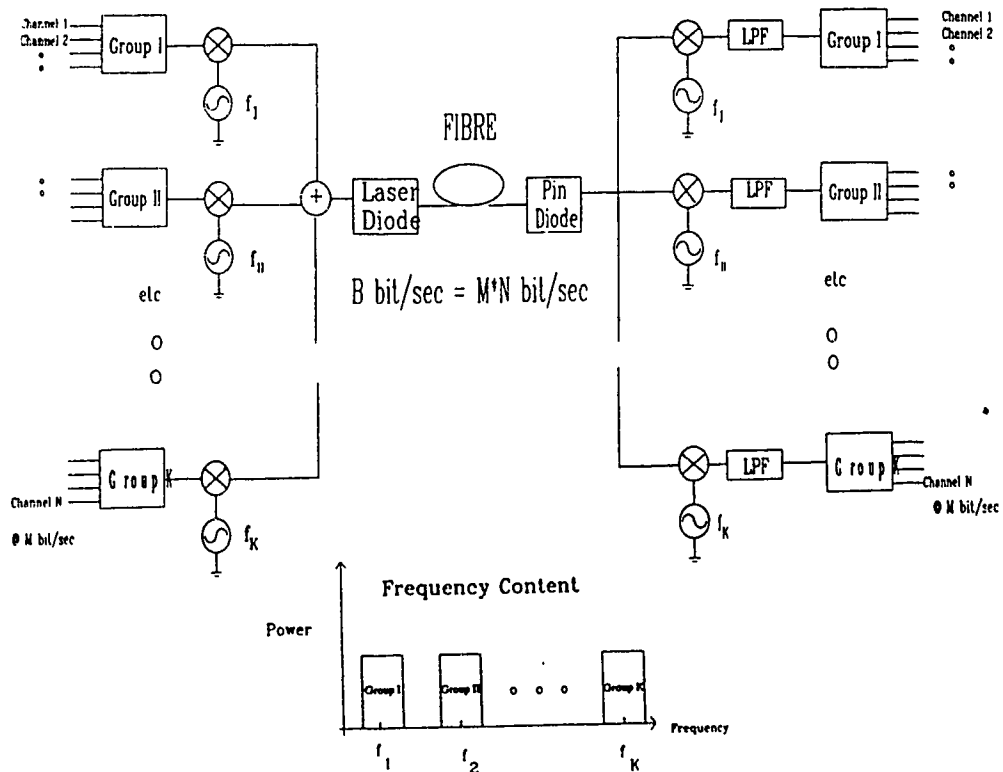


Figure 1.1- Block Diagram of General Digital Subcarrier Multiplexed System

The optical SCM link inherently is characterized by a wide modulation bandwidth and a limited power budget. As a result, digital modulation formats such as binary frequency shift keying (BFSK) [10] or binary phase shift keying (BPSK) [11] & [14] have been used which are simple and robust but bandwidth inefficient (typically have 0.5 bit/s/Hz bandwidth efficiency). These digital modulation formats may be used in our application, however, they are undesirable because they are not very bandwidth efficient. To increase the bandwidth efficiency and hence point to point transport capacity, we have considered in this work the new technique of modified orthogonal subcarrier multiplexing and what transmission capacities may be achieved by it on a modern SCM link.

1.3 THESIS OVERVIEW

Presented in this work is a new frequency division multiplexing technique where sinusoidal carriers are modulated with simple nonbandlimited baseband pulse shapes and the resulting channels spaced with no guard bands. This technique is called modified orthogonal subcarrier multiplexing (or modified orthogonal SCM) and achieves bandwidth efficiencies of 1 to 2 bit/s/Hz. The transport capacity of different modified orthogonal SCM implementations is determined by simulation in the presence of laser resonance distortion and expected levels of noise at the receiver. The thesis is organized as follows.

To estimate maximum transport capacity using modified orthogonal multiplexing, modelling of the transmission medium is first discussed. In Chapter 2 the lightwave link is examined to identify the most significant source of distortion and noise. A worst case approach is outlined which simplified our analysis to consideration of only laser resonance distortion and the system noise. Modelling of laser resonance distortion was accomplished by numerically solving the coupled single mode rate equations whose parameters represented a multimode InGaAsP SCM laser. This model was benchmarked with predicted analytical expressions and was found to be conservative. The passive optical

components were considered distortionless and an expected dc photo-current from the photodetector was calculated. From this photo-current, the system noise was estimated.

Keeping in mind the optical transmission medium, the bandwidth efficient and moderately complex technique of modified orthogonal subcarrier multiplexing (or modified orthogonal SCM) was developed and is presented in Chapter 3. This technique uses simple or no baseband pulse shaping and permits the multiplexing of double sideband channels with no guard bands, if all channels carry synchronous data. The technique yields bandwidth efficiencies of 1 to 2 bit/s/Hz depending on the particular implementation selected.

In Chapter 4 the simulation experiments and results are presented. Given in Section 4.1 are the intersymbol interference, interchannel interference, phase error and statistical characteristics of different modified orthogonal SCM configurations. In Section 4.2 the transport capacity versus system margin of each modified orthogonal SCM configuration on the optical link is presented. These simulation results were obtained by multiplexing 5 to 10 Gbit/s of random data to create a broadband composite signal using modified orthogonal SCM, and passing it through the laser resonance distortion model. This was because data rates higher than 10 Gb/s were not feasible. An eye diagram analysis was performed on channels which experienced the most distortion. The maximum eye opening was scaled in simulations to result in an equivalent current, to which the system noise could be referenced directly and the BER calculation could be made.

In Chapter 5 conclusions, suggested further work and other applications for this technique are given. It was concluded that 10 Gbit/s per link may be possible with a reduction in laser RIN from -140 dB/Hz to -155 dB/Hz. This transmission capacity would be best achieved using a rectangular baseband pulse shape.

Chapter 2

THE LIGHTWAVE LINK

Transmission of the frequency multiplexed broadband microwave signal to the receiver is via an analog fibre optic link. The optical transmission system, including electro-optic components is noisy and nonlinear. To estimate performance or transmission capacity of any signal being passed through this link, distortion arising from nonlinearity and addition of random noise must be considered in our analysis. Considering the intentions and scope of this study it was decided that only the worst case distortion and noise is to be considered in our analysis. This approach accounts for only the dominant signal degradations for components of the signal which experience the most distortion and noise, and transmission capacity estimates for the system then are the worst case ones. This simplifies our analysis to a manageable size and gives room for optimization in a real system.

Distortion arises in the form of products which appear in frequency at positions dependent on the source frequencies and with a power related to the source's power. The relationship between the amount of power appearing in the distortion products and the power at the source frequencies is determined by the nature of the nonlinear device and the statistics of the signal. If the signal is reasonably well behaved, estimates of distortion power appearing at the distortion product frequencies may be calculated analytically. In the case of a signal which is not well behaved statistically, time domain effects of signal distortion may be accurately observed by generating the composite broadband signal in a simulation and applying it to a numerical model which has the same distortion characteristics as the nonlinear device of interest. By taking this approach, distortion caused by statistical irregularities of the signal is accounted for by passing this broadband signal through the distortion model, and may be measured by demodulating a number of

channels and observing the distorted symbols. Due to the unusual statistics of our composite broadband signal (which are discussed in Section 4.1.5) we chose to pursue this route to account for distortion in estimating transmission capacity of our SCM link.

Distortion may arise from many different elements in the system, however the most difficult to model in this analysis is the behaviour of the laser. This is because distortion arises from two distinct effects: resonance distortion where the amplitude of the distortion products appear as a function of frequency, and nonlinearity of the light power - drive current curve where the amplitude of the distortion products is independent of frequency [2]. Another source of distortion is fibre dispersion, which is small over distances less than 1 km but still necessary to consider. A simple dispersion calculation for a multimode laser outlined in Section 2.2 shows that dispersion is not significant in this system and hence was ignored. All other system components were defined to be distortionless in this analysis because they are well understood and may be accounted for independently by subtracting a penalty from the system margin. Therefore only laser distortion was considered in our distortion analysis.

The second source of signal degradation necessary to consider to estimate transmission capacity arises from addition of random noise appearing at all points in the system. The sum of noise contributions from all distributed sources in the system may be replaced by an equivalent system noise at one point. In our system the point of reference was chosen to be the output of the photodetector, see Figure 1.1. The noise is expressed at that point as noise current power spectral density (in A^2/Hz) and may be calculated by adding the noise (on a power basis) from all distributed sources as each would appear at the reference point.

The sources of noise in our system which are significant enough to consider include the following: laser relative intensity noise (RIN), photodetector shot noise, and preamplifier thermal noise. The levels of RIN and photodetector shot noise appearing at the reference point are dependent on the photocurrent output from the photodetector which

is directly proportional to the power of the received lightwave, while the preamplifier thermal noise is not dependent on the received optical power. Therefore it is necessary to estimate a received light power in our system. To accomplish this, specific assumptions about the system's electro-optic and optical components must be defined which include the following: power output from the laser, coupling efficiency into the fibre from the laser, optical loss due to fibre attenuation and connector losses, and coupling efficiency into the photodetector. A calculation of the level of system noise at the reference point may then be done.

Chapter 2 is organized as follows. A modern semiconductor laser designed for SCM applications and its characteristics are discussed in Section 2.1; the elements required for proper modelling in our worst case analysis are summarized. The distortion characteristics of the directly modulated semiconductor laser are considered in Section 2.1.1, with the explanation of both nonlinearity of the light current curve, and resonance distortion (expressions are also given which benchmark our laser model) in subsections 2.1.1a and 2.1.1b. In Section 2.1.2 the approach for modelling laser's resonance distortion is presented, along with an explanation in subsections 2.1.1a and 2.1.1b of the laser's resonance behaviour. Presented in Section 2.1.3 is our model for laser resonance distortion followed by its distortion characteristics in Section 2.1.4 which are benchmarked with analytical expressions given in [27] and [28]. For the purpose of identifying what type of distortion product will be dominant and where the most distortion will appear in the composite broadband signal described in Chapters 3 and 4, a qualitative analysis to determine this is presented in Section 2.1.5. The final laser characteristic to be considered is the laser's relative intensity noise in Section 2.1.6. The passive optical transmission components and receiver are discussed in Section 2.2, which is followed by a calculation of system noise in Section 2.3 and a summary of the assumptions for the optical link.

2.1 LASER CHARACTERISTICS AND MODELLING

SCM applications use direct detection of the received light power, which resulted in its spectral properties being less important than in coherent optical systems. This consequently allows a multimode laser to be used. Without the constraint of maintaining only a single lasing mode, a family of semiconductor lasers has been developed for SCM applications possessing direct modulation bandwidths in excess of 20 GHz while maintaining good linearity and low noise [15]. The wavelength of operation targeted for many SCM applications has been at 1.3 μm , in the window of low fibre attenuation and dispersion. Consequently a family of InGaAsP buried heterostructure semiconductor lasers at 1.3 μm has evolved to be suitable for many SCM applications [2]. Thus, it is reasonable to choose a laser from the InGaAsP-BH family for the optical source in our particular system model.

To properly characterize and model the intensity modulated laser diode, there are three major laser properties which must be considered. First to consider is the laser's nonlinear distortion characteristics which includes two distinct effects: nonlinearity of the light power-current curve, and resonance distortion which is a function of frequency and arises from the intrinsic mixing of photons and electrons in the laser cavity. Second to consider is the natural resonance frequency of the laser which generally is the same as its maximum modulation bandwidth if the laser's relaxation oscillation frequency is well damped. The laser's resonance frequency is a function of the bias current and was set in our laser model to have a fixed value of 10 GHz. The third consideration is the light output power from the laser. This is inclusive of the average output power level and intensity fluctuations relative to this average which are known as relative intensity noise (RIN). A laser output power of 7.5 mW was assumed. This appears reasonable given that an

average power output of 10 mW from the InGaAsP-BH laser used by Bowers in [36] was achieved. The maximum value for laser RIN was assumed to be -140 dB/Hz.

2.1.1 Laser Distortion Characteristics

Intensity modulation of the laser with an analog signal is accomplished by modulating its drive current with the scaled signal. The resulting light output has some average intensity level modulated with a signal having an optical modulation depth (OMD) defined as half the ratio of the peak to peak modulated optical power to the dc optical power. This may also be expressed in terms of an rms equivalent OMD which is measured in terms of the signal's average power. As the modulation depth increases from zero, the transformation of drive current into optical power becomes non-linear and introduces distortion products.

There are two types of nonlinear distortion products which must be considered here: harmonic and intermodulation. Harmonic distortion products from a single tone at frequency of f_1 appear at $2f_1$ for second order, $3f_1$ for third order and so on. Intermodulation between two frequencies f_1 and f_2 results in second order distortion products appearing at f_2+f_1 and f_2-f_1 . These second order IMD products will be referred to as IMD_{II} in the following sections. Third order two frequency IMD products (defined as IMD_{III-2}) appear at frequencies of $2f_2-f_1$, $2f_1-f_2$, $2f_2+f_1$, and $2f_1+f_2$; of which the first two appear within the source band if f_1 and f_2 are near each other. Third order intermodulation distortion also arises from the interaction between three frequencies f_1 , f_2 and f_3 resulting in products which may appear throughout the source band of interest (defined as IMD_{III-3}). The IMD_{III-3} products appear at frequencies of $(\pm f_1 \pm f_2 \pm f_3)$ [22] and are 6 dB higher in magnitude than IMD_{III-2} products [28].

Distortion products are generated in the laser cavity and arise from two distinct effects: resonance distortion and nonlinearity in the light power-drive current curve. Nonlinearity of the light current curve arises from the nonlinear threshold knee, and from a

decreasing quantum efficiency with increasing bias resulting in a “saturation” or roll off of the curve at higher bias points (called sublinearity). This type of distortion is independent of frequency and may be modelled by a power series expansion about the bias point. It is usually dominant at modulation frequencies in the 100’s of MHz range [23], [24] & [25]. Resonance distortion arises from a resonant interaction between the excited carriers and photons inside the lasing cavity and is a function of frequency. For a modern SCM laser (in particular one from the family of InGaAsP lasers) resonance distortion increases with frequency and becomes dominant for frequencies in the multi-GHz range [23], [24] & [25]. Since resonance distortion is a result of the resonant coupling between the carriers and photons in the laser cavity, it’s behaviour may be modelled by the semiconductor laser rate equations [29]. The rate equations describe how the photon and carrier densities interact to determine the junction photon density (which is proportional to the laser light power output) as a function of time, given a time varying drive current. Our system was assumed to modulate the laser up to near its resonance frequency, therefore we assume that frequency dependent distortion arising from resonance is dominant in our analysis.

Evaluation of system performance was based on a worst case analysis. Therefore considering channels where the most distortion appears is a sufficient condition for modelling only resonance distortion. To optimize performance for all channels, it would be necessary to also consider distortion introduced by the nonlinear light current curve. However, this was thought of as unwarranted because the results of this preliminary system study are only intended to be a first indicator for realizing the transmission capacity for a system of this type in the laboratory. To clarify the difference in distortion mechanisms, a description of both nonlinearity of the light current curve and resonance distortion will be discussed in the following two subsections.

2.1.1a Nonlinearity of the Light Power-Current Curve

There are two regions of the non-linear light power-current curve which cause distortion: the turn on knee just above threshold and a sublinear shape of the light power current curve at high bias points. The nonlinear light current characteristic of the laser near threshold is described by the laser rate equations and is a source of clipping distortion when the instantaneous signal drive current has excursions near or below threshold. At signal drive current levels well above the “turn on knee”, a nonlinear roll off of the light power current curve occurs which is caused by effects that are not accounted for in the rate equations and is called sublinearity. This phenomenon may be described simply by the total quantum efficiency, which is defined as the number of photons output from the junction divided by the number of electrons injected into the junction in a given time interval. This may be stated as

$$\eta_{\text{total}} = qE_g \frac{dP}{dI} \quad (2.1)$$

where:

$$\begin{aligned} q &= \text{charge of an electron} \\ E_g &= \text{bandgap energy of the dominant lasing mode} \\ dP/dI &= \text{derivative of the light power-drive current curve} \end{aligned}$$

It has been observed that the total quantum efficiency of an InGaAsP laser diode decreases with increasing bias above threshold and consequently results in the sublinear shape in the light power-drive current curve [2].

This sublinearity (or saturation) is caused by a number of mechanisms, which include current leakage, intervalence band absorption, and free-carrier absorption [23]. These mechanisms are adequately described by the light power-current curve which is a static characteristic, and therefore may be modelled by a simple power series expansion about the bias point or by a simple AM-AM conversion model. The amplitude of distortion products generated are independent of modulation frequency [24]. As outlined earlier, our laser model used in this work is based on the rate equations, therefore only the nonlinear

power-current curve near threshold is assumed to be linear and gain is

ignored.

2.1.1b Resonance Distortion

Resonance distortion results from nonlinear coupling between the photons and injected carriers in the lasing junction. It is a dynamic phenomenon that is a function of frequency. This coupling process is described by the laser rate equations and consequently characterizes resonance distortion. Given in this section are the analytical expressions derived for 2nd order harmonic (2HD) and 3rd order intermodulation distortion products (IMD_{III-2} & IMD_{III-3}) from the single mode rate equations when driven with small signal, two and three tone distortion tests. These expressions were used to benchmark the resonance distortion model as outlined in Section 2.1.4. Also presented in this section is an illustration of how these particular resonance distortion products appear as a function of frequency for a typical InGaAsP-BH laser.

Lau in [26] performed a small signal analysis on the single mode rate equations (which characterize a laser operating in only one longitudinal mode), excluding the effect of gain compression shown in (2.11), to calculate analytically the second order harmonic (2HD) and third order intermodulation distortion products (IMD_{III-2} & IMD_{III-3} for two and three frequency 3rd order products respectively). He found that both the amplitude of 2HD, IMD_{III-2} and IMD_{III-3} increased with frequency, having a local peak occurring at half the natural relaxation frequency. In [27] and [28] Darcie extended Lau's analysis to include additional distortion terms and damping due to gain compression for InGaAsP semiconductor lasers. The analytical magnitudes of 2HD, IMD_{III-2} and IMD_{III-3} relative to the source carrier(s) magnitude C are given as

$$2HD \equiv \frac{2hd}{C} = OMD \left(\frac{f^2}{f_r^2 g(2f)} \right) \quad (2.2)$$

$$\text{IMD}_{\text{III-2}} \equiv \frac{\text{imd}_{\text{III-2}}}{C} = \frac{1}{2} \text{OMD}^2 \frac{V \omega_r \epsilon}{g(f)g(2f)} \frac{1}{f_r} \quad (2.3)$$

$$\text{IMD}_{\text{III-3}} = \text{IMD}_{\text{III-2}} + 6\text{dB} \quad (2.4)$$

where:

$$g(f) = \sqrt{\left(\left(\frac{f}{f_r}\right)^2 - 1\right)^2 + \left(\frac{2\pi\epsilon f}{g_0}\right)^2} \quad (2.5)$$

when: $\omega \gg \frac{1}{2\pi\tau_n}$ which is in the same decade of frequency as f_r

where: ϵ - gain compression damping factor (m^3)

τ_p - photon lifetime (sec)

τ_n - carrier lifetime (sec)

g_0 - optical gain coefficient (m^3/s)

f_r - natural resonance frequency (Hz) or relaxation frequency

OMD - optical modulation depth (dimensionless)

f - source frequency for the case of 2HD, or the product frequency at ($2f_2 - f_1$)
resulting from intermodulation of two closely spaced subcarriers

The magnitude of distortion products predicted by these analytical distortion formulas were verified experimentally by Darcie using two and three tone distortion measurements on an InGaAsP laser and the results were found to match very closely (2.2) through (2.5) [28]. Darcie also observed that the distortion characteristics were very similar for different types of InGaAsP lasers [27]. This observation validates modelling the resonance distortion properties of only one particular InGaAsP laser by allowing us to suggest that our results may be applied qualitatively to any InGaAsP-BH laser. It has also been observed by Way [30] that optical feedback had a detrimental effect on the resonance distortion levels. Therefore to minimize distortion inducing coherent reflections, an optical isolator was assumed to be inserted between the laser and fibre in our system model.

See Figure 2.1 for a resonance distortion versus frequency characteristic of a typical InGaAsP laser predicted by (2.2) through (2.5). Note that intermodulation products have a local maximum at half the natural relaxation frequency which is a general characteristic of resonance distortion, however the mechanism behind this phenomenon is still unclear [23].

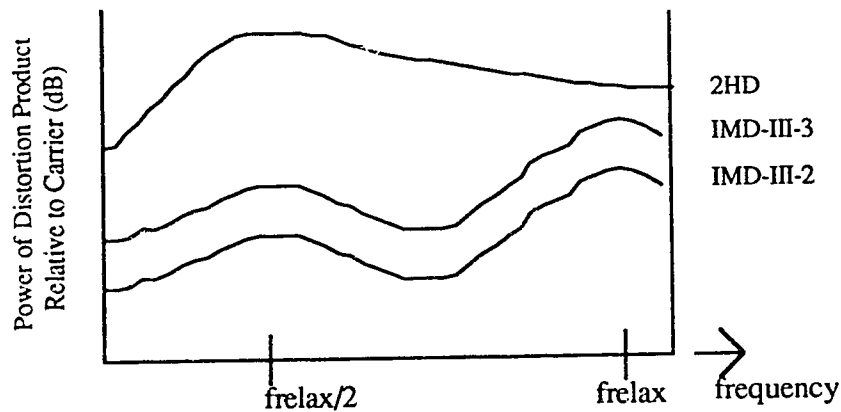


Figure 2.1- General Resonance Distortion Characteristic of a Typical InGaAsP-BH Laser

2.1.2 Approach for Modelling Laser Resonance Distortion

Our approach of using the single mode rate equations to model resonance distortion for a multimode 1.3 μm InGaAsP-BH laser is now explained. In subsection 2.1.2a a background description is given of the rate equations, followed in subsection 2.1.2b by a description of the junction's frequency response and resonance frequency (also known as the natural relaxation frequency) which are determined by the resonant coupling between carriers and photons and is described by the rate equations.

Since resonance distortion is a result of the dynamic coupling process between the photons and electrons in the lasing cavity described by the rate equations, solving the coupled single mode rate equations in time should yield a model of resonance distortion. Tucker modelled a multimode InGaAsP-BH laser diode by developing a large signal equivalent circuit based on the single mode rate equations [20]. He measured the equivalent single mode parameters from the laser of interest and substituted them into the equivalent circuit. His frequency response analysis qualitatively gave the same results as using the multimode rate equations, and with a much simplified analysis [20]. Way used Tucker's large signal equivalent circuit to model the resonance distortion characteristics of a single mode 0.8 μm GaAlAs semiconductor laser [29]. Way measured the equivalent rate equation parameters from the 0.8 μm laser and by substituting them into Tucker's equivalent

distortion levels. In further work [31], Neusy numerically solved the two coupled single mode rate equations by a simple Euler forward integration instead of using Tucker's large signal equivalent circuit. Substituting Way's rate equation parameters, Neusy observed approximately the same levels of resonance distortion. Neusy implemented the model in BOSS (Block Oriented System Simulator) which was the same simulation package used in our work.

We extended Tucker's approximation of using the single mode rate equations for modelling a multimode InGaAsP-BH laser to include resonance distortion. In [20] Tucker measured the equivalent single mode rate equation parameters for a multimode InGaAsP-BH laser for purposes of frequency response analysis. We substituted Tucker's single mode rate equation parameters for a multimode InGaAsP-BH laser into Neusy's BOSS model. This resulted in a model of the resonance and clipping distortion for a multimode InGaAsP-BH laser using the single mode rate equations. This model simulates the resonant nonlinear coupling process between excited carriers and photons which is the source of resonance distortion.

To benchmark the resonance distortion characteristics of our laser distortion simulation model, single, two and three tone distortion tests were performed by giving a certain modulation depth to each tone, passing the sum through the laser model and doing an FFT on the output signal from the model. The 2HD, $\text{IMD}_{\text{III-2}}$ and $\text{IMD}_{\text{III-3}}$ product levels were measured as a function of frequency by varying the frequencies of the tones. The comparison with the amplitude distortion product levels predicted as a function of frequency by (2.2) to (2.5) will be done in Section 2.1.4.

The following subsection will consider the laser rate equations which characterize the large signal lasing process in a semiconductor laser. These equations describe the nonlinear coupling process between injected carriers and photons; consequently they describe the laser's resonant behaviour. This resonance generally limits the available

source of resonance distortion which is the focus of our interest in the distortion model. The frequency response characteristics inherently predicted by the rate equations will be considered subsequently in section 2.1.1b.

2.1.2a The Semiconductor Laser Rate Equations

The optical source chosen for the problem in this work is a multimode InGaAsP-BH semiconductor laser (see Section 2.1) which is pumped into the lasing condition by forward biasing a p-n junction. To analyze the modulation and distortion characteristics of a multimode semiconductor laser it is necessary to consider the rate equations which characterize the photon and carrier interactions internal to the laser cavity of all the lasing modes. To very precisely model the modulation and distortion behaviour in the presence of more than one longitudinal mode in the laser cavity, it is necessary to use the multi-mode rate equations. These equations account for saturation effects in the gain curve versus wavelength which describes behaviour of the optical lasing gain for a particular longitudinal mode in the presence of all other modes [17].

The multimode rate equations are given by Olshansky [18] in a form similar to

$$\frac{dN}{dt} = \frac{I}{eV} - \frac{N}{\tau_n} - \sum_i g_i S_i \quad (2.6)$$

$$\frac{dS_i}{dt} = \Gamma g_i S_i - \frac{S_i}{\tau_p} + \beta_i \Gamma \frac{N}{\tau_n} \quad (2.7)$$

where N is the injected carrier density, I is the drive current, e is the charge of an electron, V is the cavity volume, τ_n is the average carrier lifetime at threshold, g_i is the gain in mode i and is a function of the photon densities, S_i , in all other modes, τ_p is the photon lifetime (related to the optical loss), β_i is the probability of spontaneous emission of light energy being transferred into the energy of lasing mode i , and Γ is the optical confinement factor of the light in the lasing cavity.

multimode lasers not observed in single mode lasers, such as frequency chirping, which enables wider intensity modulation bandwidths [17]. For precise characterization of the mechanisms responsible for various phenomena, it is necessary to use the multimode rate equations. However for frequency modelling of an InGaAsP multimode laser it was suggested by Bowers in [19] that a single-mode rate equation analysis is considerably less complicated and yields qualitatively the same results as using the multi-mode rate equations. This approach was also taken by Tucker in [20] where he directly measured the equivalent single mode rate equation parameters of an InGaAsP-BH laser for purposes of frequency response analysis. His single mode model showed a good fit with measured data and found that the packaging of the particular laser he was measuring limited the frequency response.

Since the primary interest in this section is to approximately model the laser's worst case resonance distortion, described entirely by the rate equations, assume that the single mode rate equations adequately characterize this phenomenon for a multimode InGaAsP-BH laser. This approximation is verified quantitatively in Section 2.1.4. Therefore the above multimode rate equations (with the same constants) simplify to the single mode rate equations by setting the mode index $i=0$:

$$\frac{dN}{dt} = \frac{I}{eV} - \frac{N}{\tau_n} - gS \quad (2.8)$$

$$\frac{dS}{dt} = \Gamma gS - \frac{S}{\tau_p} + \beta \Gamma \frac{N}{\tau_n} \quad (2.9)$$

$$g = g_0 (N - N_{om}) \quad (2.10)$$

where g_0 is the optical gain coefficient, and N_{om} is the transparent carrier density. The optical gain factor "g" is no longer a function of the wavelength of operation but it saturates, and can be represented as a function of the photon density S.

$$g = g_0 \frac{(N - N_{om})}{(1 + \epsilon S)} \cong g_0 (N - N_{om}) (1 - \epsilon S) \rightarrow \text{where } \epsilon S \ll 1 \quad (2.11)$$

the $(1-\epsilon S)$ factor is the first series term in the expansion of $\frac{1}{1-\epsilon S}$. This approximation is valid for $\epsilon S < 0.07$ in our analysis. This approximation was adopted to be consistent with literature [21].

The single mode rate equations then take on the form:

$$\frac{dN}{dt} = \frac{I}{eV} - \frac{N}{\tau_n} - g_0(N-N_{om})(1-\epsilon S)S \quad (2.12)$$

$$\frac{dS}{dt} = \Gamma g_0(N-N_{om})(1-\epsilon S)S - \frac{S}{\tau_p} + \beta \Gamma \frac{N}{\tau_n} \quad (2.13)$$

where: N - carrier density in active region ($1/m^3$)
 S - average photon density in the active region ($1/m^3$)
 I - current injected into the active region (A)
 e - charge of an electron (C)
 V - volume of the active region (m^3)
 τ_n - spontaneous recombination lifetime of the carriers (sec)
 g_0 - optical gain coefficient (m^3/s)
 N_{om} - transparent carrier density ($1/m^3$)
 ϵ - gain compression factor (m^3)
 Γ - optical confinement factor (dimensionless)
 τ_p - photon lifetime (sec)
 β - probability of spontaneous emissions entering lasing mode (dimensionless)

Equations (2.12) and (2.13) characterize the active region's photon and carrier densities as a function of time, given some input drive current. Let us now examine the components of (2.12).

$$\frac{dN}{dt} = \frac{I}{eV} - \frac{N}{\tau_n} - g_0(N-N_{om})(1-\epsilon S)S$$

$$\text{or } \frac{dN}{dt} = \frac{dN}{dt}_{\text{inject}} - \frac{dN}{dt}_{\text{spont}} - \frac{dN}{dt}_{\text{stimul}} \quad (2.14)$$

where $\frac{dN}{dt}$ = the net rate of change of the carrier density

$\frac{dN}{dt}_{\text{inject}}$ = rate at which carriers are injected into active region = $\frac{I}{eV}$

$\frac{dN}{dt}_{\text{spont}}$ = rate at which carriers recombine in spontaneous emission = $\frac{N}{\tau_n}$

$\frac{dN}{dt}_{\text{stimul}}$ = rate that carriers recombine in stimulated emission = $g_0(N-N_{om})(1-\epsilon S)S$

stimulated emission is accounted for by stating that dN_{stimul}/dt is proportional to the carrier population inversion above lasing threshold $(N-N_{\text{om}})$, and the electromagnetic waves energy density or photon density (S) . In other words the rate at which pumped electrons recombine with holes to emit light that is coherent in frequency, phase and direction with the incident light wave is proportional to $(N-N_{\text{om}})$, determined by the population inversion phenomenon, and to the photon density in the active region [16]. To account for effects of gain saturation, the term $g_0(N-N_{\text{om}})S$ is multiplied by $(1-\epsilon S)$ as described earlier.

Let us now examine the components of (2.13).

$$\frac{dS}{dt} = \Gamma g_0 (N - N_{\text{om}})(1-\epsilon S)S - \frac{S}{\tau_p} + \beta \Gamma \frac{N}{\tau_n}$$

or $\frac{dS}{dt} = \frac{dS}{dt}_{\text{stimul}} - \frac{dS}{dt}_{\text{loss}} + \frac{dS}{dt}_{\text{spont}}$ (2.15)

The term $dS_{\text{stimul}}/dt = S/\tau_p$ is equal to $\Gamma (dN_{\text{stimul}}/dt)$ which represents the rate of change of the photon density inside the active region of the laser due to stimulated emission. The proportionality constant Γ represents the optical confinement factor. This is the fraction of the optical power which is confined within the active region.

The second term dS_{loss}/dt represents the rate at which photons are lost due to distributed attenuation and to the end facets (output power). By effectively distributing the loss due to end facets over the entire cavity, the photon density as a function of distance may be represented as [16]

$$S(x) = S(0) \cdot e^{-\alpha_1 x/2} \quad (2.16a)$$

where: $\alpha_1 = \alpha + \frac{1}{2L} \ln \frac{1}{R_1 R_2}$

α = distributed material loss

L = length of cavity

R_1, R_2 = power reflection coefficients of end facets

$$x = v \cdot t \quad \rightarrow \quad S(t) = S(0) \cdot e^{-\alpha_t v t / 2} \quad (2.16b)$$

Taking the expected value of this exponential yields an average photon lifetime.

$$\frac{t}{\tau_p} = \frac{\alpha_t v}{2} t \quad \rightarrow \quad \tau_p = \frac{2}{\alpha_t v} \quad (2.16c)$$

Thus the expected lifetime of a photon, τ_p , is inversely proportional to the total optical loss. This expected photon lifetime may then be used in the rate equations as the average time, t_0 , that photons disappear from the cavity.

$$\frac{dS_{\text{loss}}}{dt} = \frac{S}{\tau} \quad (2.16d)$$

The final term $dS_{\text{spont}}/dt = \beta \Gamma N / \tau_p$ represents the fraction of spontaneously emitted photons, which are emitted into the lasing mode multiplied by the optical confinement factor Γ as in the stimulated emission term of (2.12).

2.1.2b Resonance Frequency of Laser

The optical resonator sustains oscillation when the round trip optical gain is equal to the optical loss. Increasing the supply of carriers (increasing the injected drive current) results in a proportional increase in the output light power. From the rate equations (2.12) and (2.13) it can be shown [20] that the steady-state density of stimulated photons above threshold is given by

$$S_0 = \frac{\Gamma \tau_p}{eV} (I_0 - I_{\text{th}}) \quad (2.17)$$

where: I_0 = dc bias current
 I_{th} = junction threshold current

Therefore the light power-drive current characteristic as described by (2.12) and (2.13) is inherently linear above threshold as described by the laser rate equations.

Once the laser is biased above threshold, a modulating signal may be applied to the drive current to generate an intensity modulated lightwave. Neglecting the packaging of the

$$\frac{M(\omega)}{M(0)} = \frac{(1-\epsilon S_0)\omega_0^2}{(j\omega)^2 + j\omega \left[\frac{\tilde{\beta}}{S_0} + \frac{1}{\tau_n} + S_0 \left(g_0 + \frac{\epsilon}{\tau_p} \right) \right] + \frac{\tilde{\beta}}{\tau_n S_0} + \frac{\beta + \epsilon S_0}{\tau_p \tau_n} + (1-\epsilon S_0)\omega_0^2} \quad (2.18)$$

Where:

$$\tilde{\beta} = \frac{\beta \Gamma I_{th}}{qV}$$

$$\omega_0 = \sqrt{\frac{g_0 S_0}{\tau_p}} = 2\pi \cdot \text{natural resonance frequency}$$

S_0 = average photon density
 I_{th} = threshold drive current

By inspecting this equation it is observed that the frequency response is a second order transfer function with a resonance frequency at ω_0 which is also known as the natural relaxation oscillation frequency.

The natural resonant frequency of a laser (f_r), which generally establishes the laser's modulation bandwidth, can be expressed as

$$f_r = \frac{1}{2\pi} \sqrt{\frac{g_0 S_0}{\tau_p}} \quad (2.19)$$

Where:

$$S_0 = \frac{\Gamma \tau_p}{eV} (I_0 - I_{in})$$

Thus:

$$f_r = \frac{1}{2\pi} \sqrt{g_0 \frac{\Gamma}{eV} (I_0 - I_{th})} \quad (2.20)$$

Therefore the lasers resonance frequency is proportional to the square root of the drive current. Thus to obtain adequate modulation bandwidth for an analog signal the bias point of the laser must be chosen appropriately. In our model it was set at 10 GHz by biasing the laser at 7 times the threshold current.

2.1.3 Laser Resonance Distortion Model

It was stated in Section 2.1.1 that resonance distortion is dominant for frequencies near the laser's resonant frequency. Our analysis was based on a worst case analysis. Consequently we developed a model of resonance distortion based on the rate equations for our worst case analysis. Presented in this section is the laser resonance distortion model as implemented in the BOSS (Block Oriented System Simulator) simulation package using the single mode rate equations. The parameters used in this model along with the step and frequency response characteristics are also presented.

The single mode rate equations ((2.12) and (2.13)) are

$$\frac{dN}{dt} = \frac{I}{eV} - \frac{N}{\tau_n} - g_0(N-N_{om})(1-\epsilon S)S$$

$$\frac{dS}{dt} = \Gamma g_0(N-N_{om})(1-\epsilon S)S - \frac{S}{\tau_p} + \beta \Gamma \frac{N}{\tau_n}$$

where the drive current (I), carrier density (N) and photon density (S) are assumed to be large signal functions of time only, ie. their values are spatially uniform through the entire junction. To solve these two coupled differential equations, multiply both sides of each equation by dt and integrate from t=0 to t=T₀. The continuous integrals are given by

$$N(T_0) = \int_0^{T_0} \left(\frac{I}{eV} - \frac{N}{\tau_n} - g_0(N-N_{om})(1-\epsilon S)S \right) dt + N(0) \quad (2.21)$$

$$S(T_0) = \int_0^{T_0} \left(\Gamma g_0(N-N_{om})(1-\epsilon S)S - \frac{S}{\tau_p} + \beta \Gamma \frac{N}{\tau_n} \right) dt + S(0) \quad (2.22)$$

Now approximate the continuous integral by Euler's forward integration where the integration variable t is made a discrete variable

$$t \Rightarrow t_m = m\Delta T \quad (2.23)$$

and the integrals of (2.21) and (2.22) are approximated by a sum of discrete valued variables I(t_m), N(t_m) and S(t_m) multiplied by the time step between samples, ΔT. The above integrals then reduce to

$$N(t_m) = \sum_m \left(\frac{I(t_m)}{eV} - \frac{N(t_m)}{\tau_n} - g_0(N(t_m)-N_{om})(1-\epsilon S(t_m))S(t_m) \right) \Delta T + N(0) \quad (2.24)$$

$$S(t_m) = \sum_m \left(\Gamma g_0 (N(t_m) - N_{om}) (1 - \epsilon S(t_m)) S(t_m) - \frac{S(t_m)}{\tau_p} + \beta \Gamma \frac{N(t_m)}{\tau_n} \right) \Delta T + S(0) \quad (2.25)$$

In this numerical solution the junction carrier and photon densities are assumed to be a part of causal system driven by the injected current. Starting at $t = 0$ with all variables set to zero and then applying a drive current step disturbs (2.24) causing a change in the carrier density to a nonzero value. In the second time step, this carrier density is fed back to drive (2.24) and disturbs (2.25) which in turn will cause some nonzero condition in the photon density. Then in the third time step a nonzero photon density is fed back to (2.24) affecting the carrier density in the fourth time step. This coupling process between (2.24) and (2.25) continues till the end of the simulation. The carrier density at any given instant is therefore a function of the drive current at that time and all previous time steps (because the system is causal), as well as the carrier and photon densities of all previous time steps. Therefore equation (2.24) must be rewritten as

$$N(t_m) = \left\{ \sum_{m=0}^M \frac{I(t_m)}{eV} + \sum_{m=0}^{M-1} \left(-\frac{N(t_m)}{\tau_n} - g_0 (N(t_m) - N_{om}) (1 - \epsilon S(t_m)) S(t_m) \right) \right\} \Delta T + N(0)$$

or

$$N(t_m) = \left\{ \frac{I(t_m)}{eV} \Delta T + \sum_{m=0}^{M-1} \left(\frac{I(t_m)}{eV} - \frac{N(t_m)}{\tau_n} - g_0 (N(t_m) - N_{om}) (1 - \epsilon S(t_m)) S(t_m) \right) \right\} \Delta T + N(0) \quad (2.26)$$

Similarly the photon density at $t_m = m\Delta T$ is a function of all previous photon and carrier densities, and is given by

$$S(t_m) = \sum_{m=0}^{M-1} \left(\Gamma g_0 (N(t_m) - N_{om}) (1 - \epsilon S(t_m)) S(t_m) - \frac{S(t_m)}{\tau_p} + \beta \Gamma \frac{N(t_m)}{\tau_n} \right) \Delta T + S(0) \quad (2.27)$$

Provided that ΔT is selected to be small enough to satisfy a stable numerical solution, coupling (2.26) and (2.27) will result in a model of the resonance and clipping distortion of an InGaAsP-BH laser.

Equations (2.26) and (2.27) were implemented in a high level communication system simulation package known as BOSS (or the Block Oriented System Simulator)

which generates a FORTRAN program from multiple levels of block diagrams that the programmer constructs on a graphical LISP based interface. Figures 2.2a through 2.2d illustrate the hierarchical programming structure of BOSS and how the laser rate equation model was implemented. Figure 2.2a is the highest level of the laser model where there is an input representing the signal drive current and an output which is the junction photon density scaled by the "optical scaling coefficient" calculated by (2.41). Stepping a level down into the block labelled "LASER (RATE EQN MODEL)" is Figure 2.2b which represents the coupled carrier density (2.26) and photon density (2.27) equations separated by a unit delay which breaks the feedback path. Therefore the calculated carrier and photon densities from time instant $t_m = m\Delta T$ contribute to calculating the new densities in the next time instant $t_{m+1} = (m+1)\Delta T$. Stepping down to level 3 in Figures 2.2c and 2.2d are the block diagram representations of (2.26) and (2.27) respectively where each term is a path on which the input signal is operated on by the appropriate constants, added together and finally summed back on all previous values. In this manner a numerical solution to the laser rate equations was approximated.

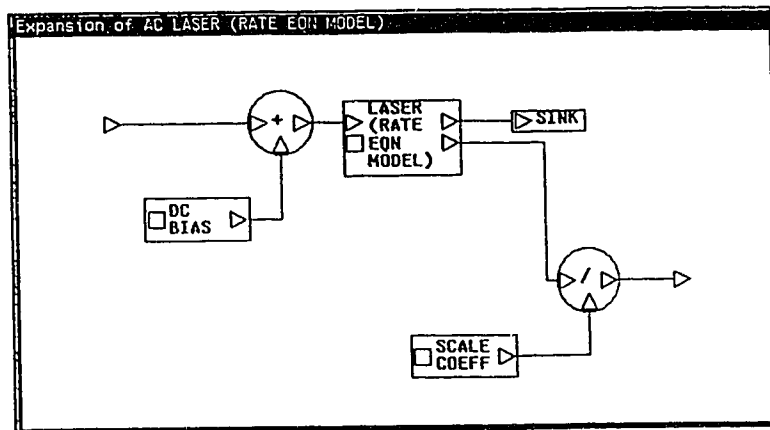


Figure 2.2a- BOSS Representation of AC Laser Rate Equation Module

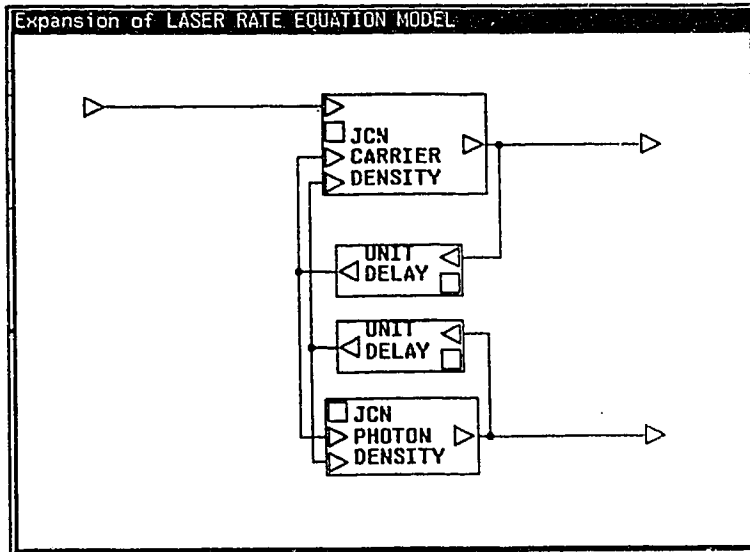


Figure 2.2b- Large Signal Laser Rate Equation Module

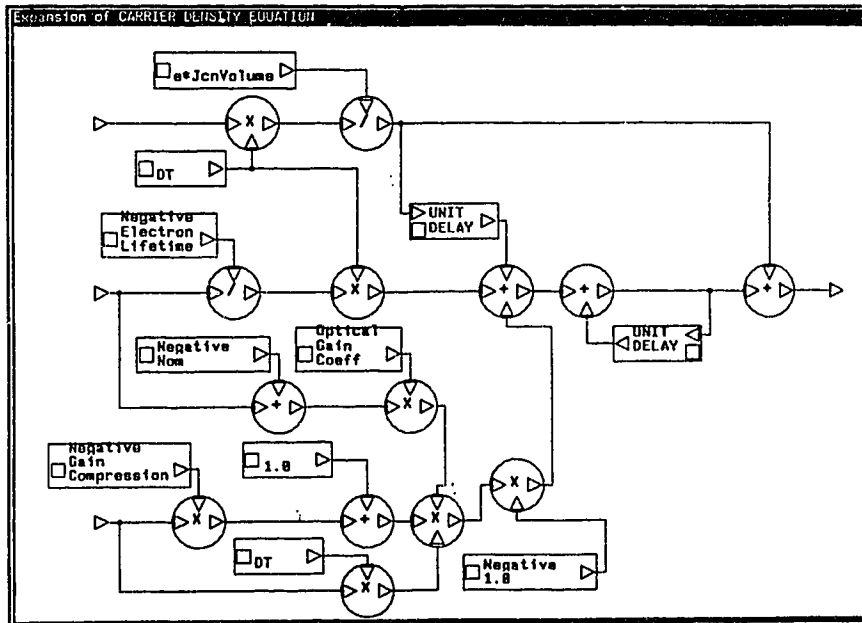


Figure 2.2c- Euler Forward Integration Module of Carrier Density Equation

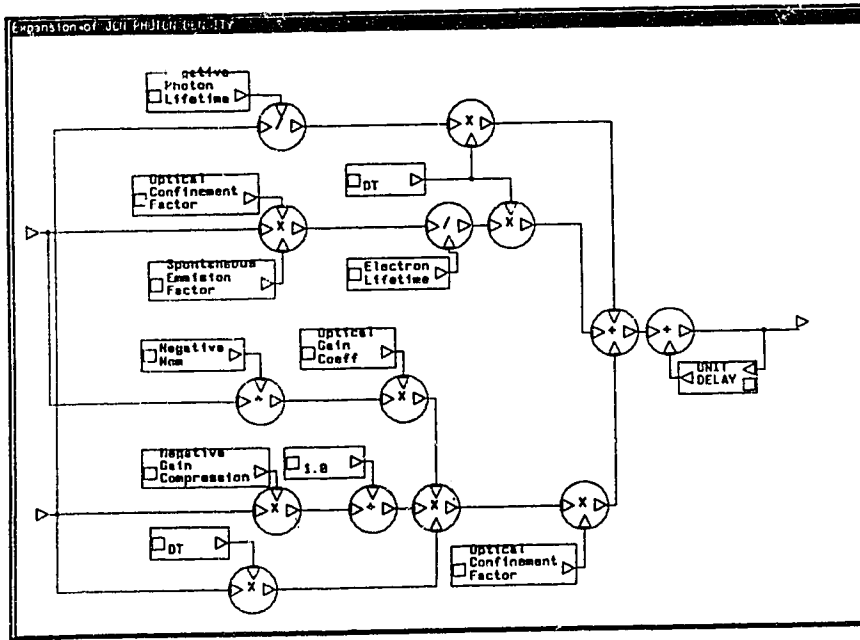


Figure 2.2d- Euler Forward Integration Module of Photon Density Equation

The equivalent single mode rate equation parameters for a multimode InGaAsP-BH laser as measured by Tucker in [20] are as follows

- $eV = 2.2 \cdot 10^{-35} \text{ Am}^3\text{s}$
- $\tau_n = 3.0 \text{ ns}$
- $g_0 = 2.4 \cdot 10^{-12} \text{ m}^3/\text{s}$
- $N_{om} = 10^{24} \text{ 1/m}^3$
- $\epsilon = 4.5 \cdot 10^{-23} \text{ m}^3$
- $\Gamma = 0.4$
- $\tau_p = 1.0 \text{ ps}$
- $\beta = 10^{-4}$

Tucker also observed a junction threshold current of 15 mA which may be derived from the above rate equation parameters. The laser is assumed to have a resonance frequency of 10 GHz for the payload simulations (the reasoning for this is described in Section 2.2). Consequently the photon density bias (S_0) given by solving (2.19) with the above laser parameters, is

$$f_r = \frac{1}{2\pi} \sqrt{\frac{g_0 S_0}{\tau_p}}$$

or:

$$S_0(f_r) = \frac{\tau_p}{\xi_0} (f_r)^2 \rightarrow S_0(10 \text{ GHz}) = 1.6 \cdot 10^{21} \frac{1}{\text{m}^3}$$

By (2.17) this corresponds to a dc drive current of 105 mA to yield a resonance frequency of 10 GHz.

As an entry point to characterize the large signal step and response frequency characteristics of this laser model, a drive current of 55 mA was chosen which corresponds to a theoretical relaxation frequency of 6.7 GHz. A time step of approximately 0.5 psec was initially chosen in the rate equation model. A drive current step of 55 mA ($3.67 \cdot I_{th}$) was applied to the current input of the model and the carrier and photon densities were observed at the output of the laser. The corresponding carrier and photon densities as a function of time are given in Figures 2.3a and 2.3b respectively. Comparing both the carrier and photon density turn on characteristics it may be observed that the carrier density increases approximately in a linear fashion from zero until stimulated emission is sustained. This is the condition that the optical gain is greater than the optical loss. At that point the photon density increases exponentially because the rate of stimulated emission is proportional to the product of the carrier and photon densities. This continues until the carrier density becomes depleted enough to saturate the gain of stimulated emission which in turn causes the photon density to peak. The photon density then decreases because the rate at which photons are lost from the cavity is greater than the rate they are produced because of the reduced gain. This causes the carrier density to increase, which again permits an increase in the photon density. This process continues until a steady state is reached. Therefore given a dc bias current, it is by this gain saturation mechanism that the steady state photon and carrier densities of the laser are determined. The natural resonance phenomenon appears as a “ringing” of the photon density in Figure 2.3b. Similar step response characteristics were given in [31] by Neusy's BOSS model.

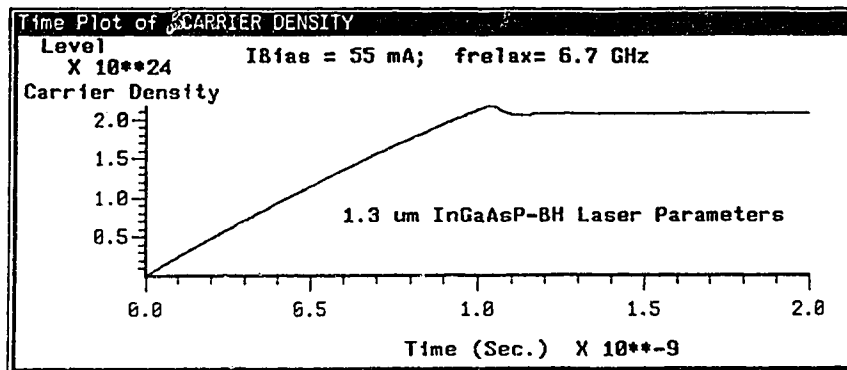


Figure 2.3a- Drive Current Step Response of Carrier Density

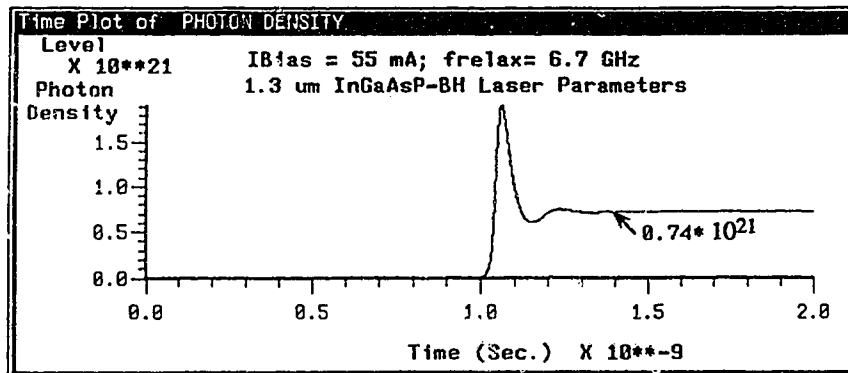


Figure 2.3b- Drive Current Step Response of Photon Density

Once this large signal model is biased, the laser's photon density may be modulated by adding an ac modulating current to the dc bias current. Since the output power is proportional to the photon density, the intensity of the transmitted lightwave carrier is therefore intensity modulated in a large carrier manner, ie AM-LC. The level of modulation is measured by the optical modulation depth (OMD), defined as half the ratio of the peak to peak modulated optical power to the dc optical power. Equation (2.18) predicts that the frequency response of the laser is a second order transfer function with a resonance frequency given by (2.20). This transfer characteristic was observed in simulations and is shown in Figure 2.4. The ac laser model is biased in this case with an injection current of 55 mA (this bias corresponds to a theoretical relaxation frequency of 6.7 GHz) and a single tone was applied sweeping in frequency from 200 MHz through to 12 GHz. The response drops off at the low end of the spectrum because the tone sweep started at 200 MHz (due to simulation reasons); the slight ripple in response was attributed to the FFT Blackman

windowing function. Note the resonant peak occurs at approximately 6.6 GHz which is close to the theoretical resonance frequency.

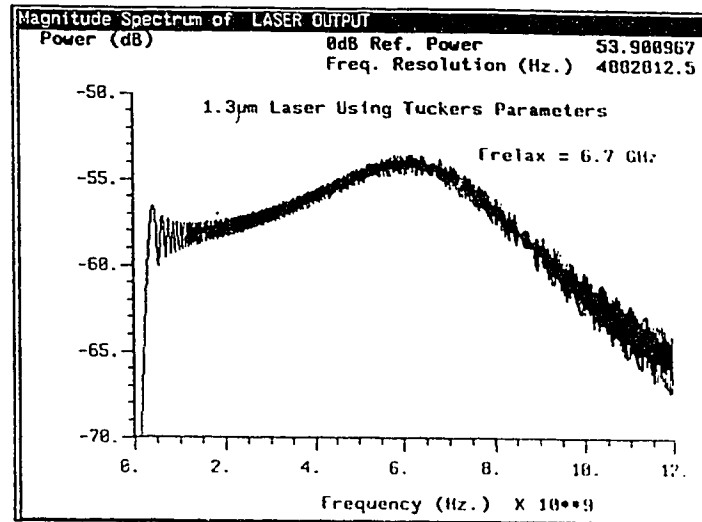


Figure 2.4- Frequency Response of Laser Model with $f_r = 6.7$ GHz.

Therefore a model similar to Neusy's model in [31] (Neusy used Way's parameters characterizing a $0.8 \mu\text{m}$ AlGaAs single mode laser) has been developed using Tucker's parameters to approximately model the step response and resonance frequency properties of a $1.3 \mu\text{m}$ InGaAsP-BH multimode laser. Next, we shall consider the distortion characteristics of this laser model as a function of frequency.

2.1.4 Distortion Characteristics of Laser Model

The distortion model adopted in this work is based on a large signal solution to the coupled rate equations (2.12) and (2.13) and consequently should model large signal clipping and resonance distortion characteristics of the laser. The clipping distortion arises from instantaneous conditions where the signal drive current has excursions to below or near threshold, and is inherently described by the laser rate equations which model its large signal turn on characteristics. This clipping near threshold is clearly observed in Figure 2.5 where the laser was biased above threshold and modulated by a carrier which dropped the drive current below threshold.

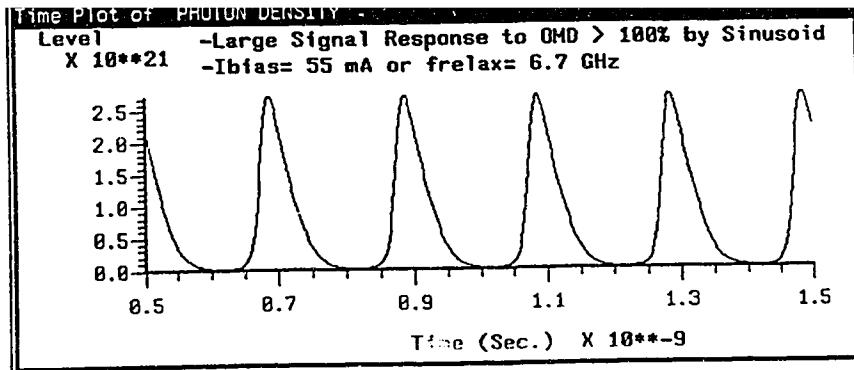


Figure 2.5- Time Plot of Sinusoid with Laser Clipping Distortion Introduced

As explained in Section 2.1.1, laser resonance distortion is described by the rate equations and therefore our laser model based on the single mode rate equations should yield a resonance distortion characteristic with 2HD, IMD_{III-2} and IMD_{III-3} products predicted analytically by (2.2) - (2.5). To benchmark the 2HD, IMD_{III-2} and IMD_{III-3} levels of our model, single, two and three tone simulation tests were performed on our model and plotted with the analytical distortion levels predicted by (2.2) - (2.5). This was done by modulating the laser directly with one, two or three tones, taking a fast Fourier Transform of the lasers output, and observing (relative to the source tone(s)) the appropriate distortion products. The bias point for characterizing the laser's resonance distortion properties was set at $I_{bias} = 105 \text{ mA} = (7 \cdot I_{bias})$ to yield a natural resonance frequency of 10 GHz. This was the bias condition used in the payload simulations. The sampling period for all simulations involving this laser model was selected to be 6.25 psec (or a sampling rate of 160 GHz) because it resulted in distortion levels for 2HD, IMD_{III-2} and IMD_{III-3} reasonably close to those predicted by (2.2) - (2.5) while still providing a stable simulation. This extremely high sampling rate was required because the distortion characteristics deviated significantly for lower sampling rates.

The two products 2HD and IMD_{III-2} (at frequencies $2f_1$ and $2f_2 - f_1$ respectively) measured (relative to source carrier(s)) are shown in Figure 2.6 where the 2HD point is shown at its source frequency, and the IMD_{III-2} product is shown at the frequency where it

appears. This convention was adopted by Darcie in [27] and [28]. The pairs of frequencies f_1 and f_2 were selected by placing f_1 and f_2 together initially at 2 GHz with $f_2 = f_1 + 200$ MHz above for all simulations, and incrementing f_1 in 500 MHz steps. It was found that the magnitude of products at frequencies $2f_1 - f_2$ followed the same distortion vs frequency characteristic as the $2f_2 - f_1$ products, that is the IMD_2 product which appeared at a given frequency appeared to be independent of the two source frequencies. Consequently only the $2f_2 - f_1$ products were plotted.

The optical modulation depth (OMD) is defined to be

$$\text{OMD} = \frac{1}{2} \frac{i_{\text{peak-peak}}}{(I_{\text{bias}} - I_{\text{threshold}})} 100\% \quad (2.28)$$

This is because the output photon density is proportional to the drive current minus the threshold current when operating above threshold as given in (2.17). The OMD was chosen to be 14% per tone which was assumed to correspond to 28% in the two tone test because the tones were coherently related. For the 2HD test, an OMD= 28% was assigned fully to a single tone.

Shown in Figure 2.6 are the distortion levels relative to the source tones predicted by (2.2) and (2.3) with an OMD= 28%, $f_r = 10$ GHz (this relaxation frequency was the same as was used in payload capacity simulations), and Tucker's $1.3\mu\text{m}$ InGaAsP-BH laser parameters. The $\text{IMD}_{\text{III-2}}$ levels predicted by (2.3) indicate a sharp, deep notch for frequencies between 6.0 and 7.4 GHz. It was confirmed in experiment by Iannone and Darcie using an InGaAsP laser that there is indeed a local minimum in this vicinity but it is less pronounced than the analytical prediction [28]. Therefore the actual local minimum in this $\text{IMD}_{\text{III-2}}$ characteristic should also be less pronounced than predicted analytically.

By examining the overlaid plots of the simulated and theoretical distortion in Figure 2.6, it is observed that the simulated 2HD level follows the predicted 2HD level very well and is somewhat more severe for source frequencies above 3 GHz. The level of the simulated $\text{IMD}_{\text{III-2}}$ products appear to average out the analytical $\text{IMD}_{\text{III-2}}$ characteristic

by lying below the theoretical levels up until half the relaxation frequency. It then continues above the predicted local minimum, peaking close to the relaxation frequency and then decreasing for frequencies above that point. Therefore the distortion levels simulated in our model appear to be greater than 8 dB below the predicted distortion levels for all frequencies of interest. The distortion characteristic for the three frequency intermodulation products ($\pm f_1 \pm f_2 \pm f_3$) were observed in simulations to be 6 dB higher than the two frequency IMD products as predicted by (2.4) [28]. The $\text{IMD}_{\text{III-3}}$ products had to be generated by three tone distortion tests and were therefore more difficult to simulate than the two frequency 3rd order IMD products (IMD_2). Since the relation given by (2.4) was verified, only two tone distortion tests were performed to measure the $\text{IMD}_{\text{III-2}}$ with no loss of generality.

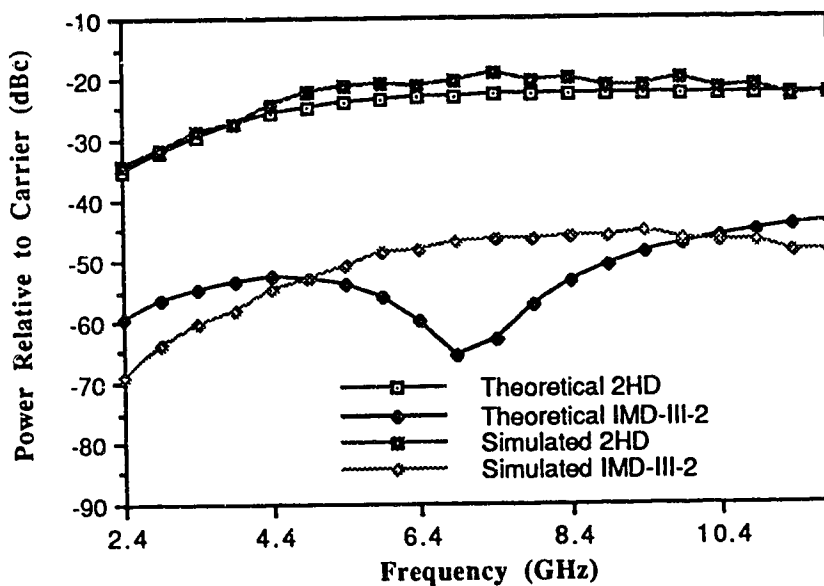


Figure 2.6- Analytical and Simulated 2HD and $\text{IMD}_{\text{III-2}}$ Characteristics for $\text{OMD}=28\% f_{\text{relax}}= 10 \text{ GHz}$

Another resonance distortion characteristic necessary to verify was how $\text{IMD}_{\text{III-2}}$ and 2HD products behave as a function of optical modulation depth (OMD). According to (2.2) the amplitude of a 2HD product is directly proportional to the OMD, therefore the 2HD power levels from two different OMD's at the same frequency are related by (2.29a).

If the OMD is reduced by half, then by (2.29a) the 2HD products power will be reduced by 6 dB.

$$2\text{HD}'' = 20 \cdot \log \left(\frac{\text{OMD}''}{\text{OMD}} \right) + 2\text{HD} \quad (2.29a)$$

Similarly (2.3) states that the amplitude of the $\text{IMD}_{\text{III-2}}$ products is proportional to the square of the OMD, which results in (2.29b). If the OMD is reduced by half, then the power of the $\text{IMD}_{\text{III-2}}$ product will be reduced by 12 dB

$$\text{IMD}_{\text{III-2}}'' = 20 \cdot \log \left(\frac{\text{OMD}''}{\text{OMD}} \right)^2 + \text{IMD}_{\text{III-2}} \quad (2.29b)$$

Similarly by (2.4) changes in OMD for $\text{IMD}_{\text{III-3}}$ products is described by (2.29c)

$$\text{IMD}_{\text{III-3}}'' = 20 \cdot \log \left(\frac{\text{OMD}''}{\text{OMD}} \right)^2 + \text{IMD}_{\text{III-3}} \quad (2.29c)$$

The simulated 2HD and $\text{IMD}_{\text{III-2}}$ products are shown in Figure 2.7 with total optical modulation depths of 14% and 28% having $f_r = 6.7$ GHz (this resonance frequency was chosen at the time of simulation for convenience). From this graph it is observed that approximately a 6 dB separation exists between the two 2HD lines, and a 12 dB separation between the $\text{IMD}_{\text{III-2}}$ lines, as expected. Therefore (2.29a) and (2.29b) are valid for predicting the resonance distortion product level at a given frequency for any OMD that is selected in our model, and verifies that the distortion introduced by our model will be correct for OMD's selected in system simulations.

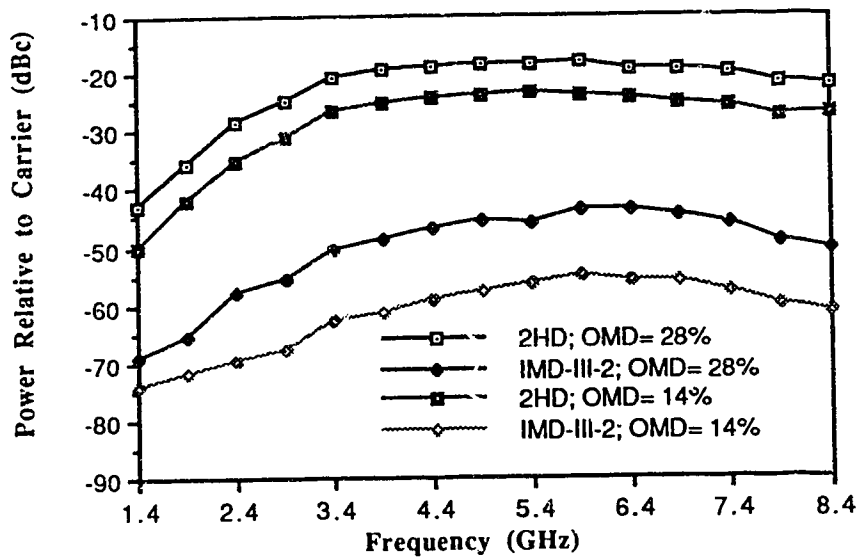


Figure 2.7- Simulated 2HD and IMD_{III-2} Characteristics for Two OMD Levels, OMD= 14% and OMD= 28% $f_{relax}= 6.7$ GHz

In summary, the second harmonic (2HD) and 3rd order intermodulation (IMD_{III-2} and IMD_{III-3}) resonance distortion properties of our 1.3 μm InGaAsP-BH laser model have been benchmarked against the analytical resonance distortion characteristics predicted by (2.2) through (2.5). Results show that our model is conservative for 2HD products (Figure 2.6) and that its predicted distortion levels for modulation depths other than 14% and 28% should be correct (Figure 2.7). Not directly benchmarked in this model are the second order intermodulation products IMD_{II} lying at frequencies of (f_2-f_1) and (f_2+f_1) . However given that the 2HD, IMD_{III-2} and IMD_{III-3} products generated in this model are all close to the predicted levels, it is reasonable to state that the IMD_{II} levels in this model will also be correct. The IMD_{II} levels were simulated by two tone distortion tests and found to be 6 dB higher than the 2HD levels, ie

$$\text{IMD}_{\text{II}} = 2\text{HD} + 6 \text{ dB} \quad (2.29\text{d})$$

Note that this is very similar to the relation (3.4).

2.1.5 Dominant Source of Distortion From Laser Model with a Fifty Channel Modified Orthogonal SCM Signal Present

The purpose of this section is to identify what type of distortion is dominant and the channel positions where the most resonance distortion occurs in our model, given the frequency plan of our modified orthogonal SCM payload described in Chapter 4. Simulating an M channel system (with the frequency plan given by (2.30) below) by passing this signal through the laser distortion model results in distortion products appearing throughout the entire composite broadband signal. For this discussion assume M= 50 channels because it was the largest simulated payload and hence experienced the most distortion. Conventional techniques to calculate signal to distortion ratio's for each channel no longer applies because of the modified orthogonal SCM signal's unusual statistical behaviour (see Section 4.1.5). However, for the purpose of a qualitative analysis to determine only what type of distortion product generates the most significant levels of distortion and in which channels it is most severe, assume that the maximum drive current is related to the individual drive currents as if they added on a mean square basis. This allows us to perform an analysis based on two tone distortion test simulation results.

In this digital SCM system, the channel carriers are assumed to be placed starting at a frequency of 400 MHz and spaced at B= 200 MHz as given in (2.30).

$$\omega_k = 2\pi(k+1)B \quad \left\{ \text{for } 1 \leq k \leq 50 \right\} \quad (2.30)$$

This results in a multioctave payload susceptible to second order distortion products. By (2.29d) the amplitude of second order, two frequency intermodulation products (IMD_{II}) will be more severe than single tone second harmonic products (2HD) by a factor of 6 dB and there will be a far greater number of (f₁+f₂) and (f₁-f₂) products than the number of 2f₁ products. Therefore the IMD_{II} products will be dominant over the 2HD product levels.

To consider where the dominant distortion appears, first let us determine the number of IMD_{II} distortion products appearing in each channel position. Let $\Delta f = B = 200$

MHz to be consistent with Olshansky's distortion product analysis [2]. By definition there are M payload channels centered at frequencies:

$$f_m = m \cdot \Delta f, \quad \text{for } m = M_{\min} \dots M_{\max} \quad (2.31)$$

Assuming there is one discrete product generated from the intermodulation of two channels, the number of second order IMP's, N_m^- for (f_1-f_2) products and N_m^+ for (f_1+f_2) products, at channel m is given by: [2]

$$N_m^- = M - m, \quad \text{for } m \leq M \quad (2.32a)$$

$$N_m^+ = \left(\frac{m}{2}\right) - M_{\min}, \quad \text{for even } m, m \geq 2M_{\min} \quad (2.32b)$$

$$N_m^+ = \left(\frac{m+1}{2}\right) - M_{\min}, \quad \text{for odd } m, m > 2M_{\min} \quad (2.32c)$$

Since the first channel lies at $2\Delta f = 400$ MHz, $M_{\min} = 2$; assuming that 50 subcarrier channels are present, $M=50$, then $M_{\max} = 51$. This yields

$$N_m^- = 50 - m, \quad \text{for } m \leq 50 \quad (2.33a)$$

$$N_m^+ = \left(\frac{m}{2}\right) - 2, \quad \text{for even } m, m \geq 4 \quad (2.33b)$$

$$N_m^+ = \left(\frac{m+1}{2}\right) - 2, \quad \text{for odd } m, m > 4 \quad (2.33c)$$

Therefore $N_{\text{total}}(f_m) = N_m^+ + N_m^- \quad (2.33d)$

Equations N_m^+ , N_m^- and $N_{\text{total}}(f_m)$ are graphed in Figure 2.8

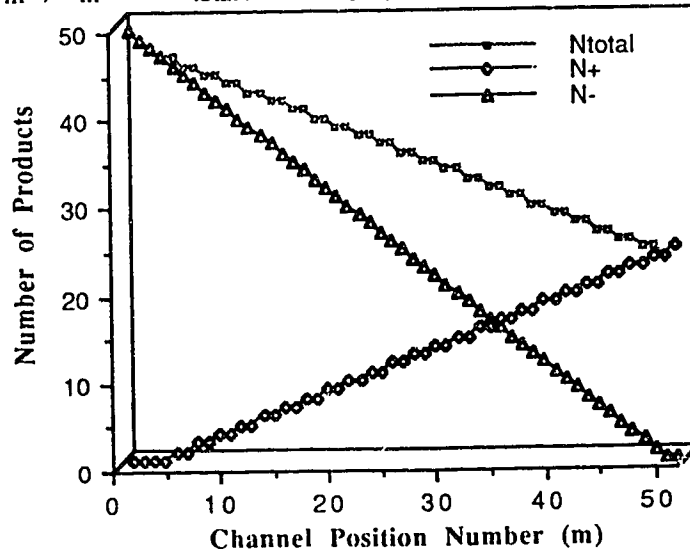


Figure 2.8- Number of IMD_{II} Products Falling in Channel Position m , Where N_m^+ are (f_1+f_2) Products, and N_m^- are (f_1-f_2) Products, and $N_{\text{total}}(f_m) = N_m^+ + N_m^-$

Simulating the 50 channel system (with the frequency plan given by (2.30)) by passing this signal through the laser distortion model will result in second order IMD products (IMD_{II}) appearing throughout the entire composite broadband signal. In Section 4.2.1 it is demonstrated that the best modulation depth when carrying a composite broadband orthogonally multiplexed signal was $OMD_{rms} = (0.7)MOD = 14\% \text{ rms}$ (the parameter MOD was arbitrarily defined for simulation purposes as being the equivalent rms modulation depth calculated from channels added on a mean square basis). It was found that when the channel currents were summed together, the correlation between channels caused a partially coherent addition to occur. This resulted in an rms modulation depth 0.7 times that calculated if the channel currents were summed on a mean square basis. As stated earlier, the channel powers are assumed in this qualitative analysis to add on a power basis. Therefore let us select the OMD of each channel to have the same OMD as was given to each individual channel in the modified orthogonal SCM signal with 50 channels present. This OMD is equal to 2.83%; therefore if all fifty uncorrelated channels were summed together, the rms OMD would be 20%.

Now replace each channel by a carrier having an arbitrary fixed phase so that they add on a mean square basis, and have an amplitude corresponding to an $OMD = 2.83\%$. Now the total distortion power appearing in any channel position is given by the power of one distortion product appearing in that frequency position, multiplied by the number of products appearing in that band from all other products; this may be expressed in dB as:

$$IMD_{II-Total}(f_m) = IMD_{II}(f_m) + 10 \cdot \log N_{total}(f_m) \quad (2.34a)$$

The single IMD_{II} products as they appear in frequency from a two tone distortion simulation tests are shown in Figure 2.9. Each $IMD_{II}(f_m)$ point corresponds to the power (in dB) of one distortion product (relative to the channels power) observed by taking an FFT of the output from the laser model given that two tones (each having an $OMD = 2.83\%$) modulated it. The total distortion power for each channel position is also given in Figure 2.9 and was calculated using (2.34a).

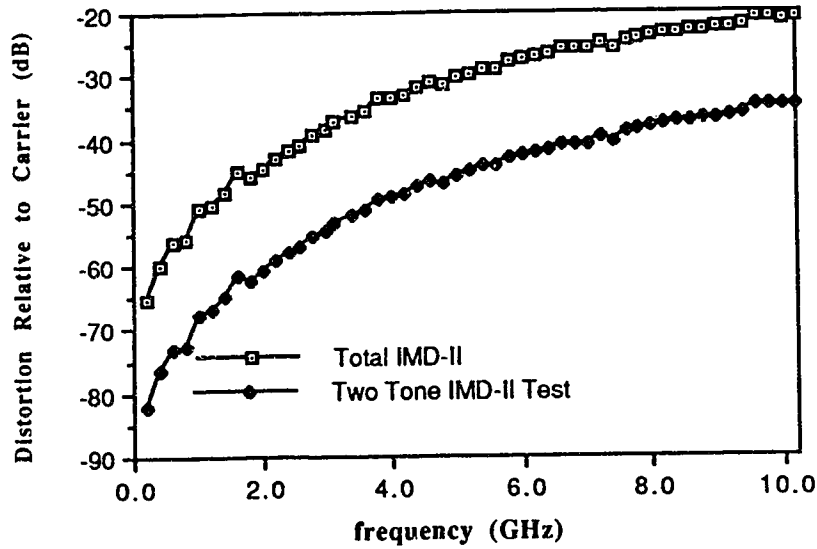


Figure 2.9- Single $IMD_{II}(f_m)$ Products Observed From Two Tone Distortion Test Simulations with $OMD = 2.83\%$ per Tone, and the Total Projected Distortion With 50 Uncorrelated Channels Spaced According to (2.30)

Another source of distortion which is of concern are the 3rd order three tone IMD_{III-3} products. From Figure 2.6 and (2.4) it is observed that with a total OMD of 28% in a two tone distortion test ($OMD = 14\%$ for each tone), the maximum distortion product level observed was -39 dB. Translating this distortion level from an $OMD = 14\%$ for each tone to $OMD = 3.83\%$ is accomplished using (2.29c) Now in an M channel SCM system there will in general be $M^2/2$ or less, third order IMD_{III-3} lying within each SCM channel [2]. If there are 50 random phased channel carriers present, each possessing a modulation depth of 2.83% as above, then the worst case distortion level due to IMD_{III-3} would be

$$IMD_{III-3-max} \leq -39 \text{ dB} + 20 \cdot \log \left(\frac{OMD''}{OMD} \right)^2 + 10 \cdot \log \left(\frac{N^2}{2} \right) \quad (2.34b)$$

$$IMD_{III-3-max} \leq -39 \text{ dB} + 20 \cdot \log \left(\frac{2.83\%}{14\%} \right)^2 + 10 \cdot \log \left(\frac{(50)^2}{2} \right) = -36 \text{ dB}$$

Comparing this to the maximum expected distortion level predicted in Figure 2.9 we see that the most significant source of distortion, in the worst case, are IMD_{II} products appearing at the highest channel positions. Since the three frequency, IMD_{III-3} products are 6 dB lower in magnitude than this level, they may be ignored. Therefore it may be

concluded that IMD_{II} products due to resonance distortion are the most significant contributors to the total distortion introduced by the laser model with 50 carriers present which add on an power basis, and is maximum in channels positioned nearest the laser's resonance frequency.

In summary, by performing a distortion analysis by adding products on a power basis it has been shown that for a system having a carrier plan given by (2.30), the maximum source of distortion arises from IMD_{II} products and the most distortion appears in channels nearest the laser's natural resonance frequency. If the channel signals do not add on a mean square basis, as is the case for our modified orthogonal SCM signal (see Section 4.1.5), the qualitative results above do not apply. However the relationship between the signal power levels and the corresponding different distortion products will remain unchanged. Therefore from this analysis it may be deduced that the most resonance distortion arises from IMD_{II} products and will be observed in the highest channel positions. This information was needed to properly select the sample set of worst case channels for demodulation from the broadband composite signal in transmission capacity simulations (see Section 4.2).

2.1.6 Laser's Relative Intensity Noise Characteristics

When considering the noise characteristics of an optical transmission system, it is necessary to consider the noise of the semiconductor laser in addition to the receiver noise. The noise at the output of the laser is called relative intensity noise (RIN) and is defined as

$$RIN \equiv \frac{\langle (\Delta P(f))^2 \rangle}{\langle P_0 \rangle^2} \quad (2.35)$$

where:

$\langle (\Delta P(f))^2 \rangle$ = the mean-square light intensity fluctuation spectral density of the light output from the laser (W^2/Hz)

P_0 = the average laser light intensity, or dc light output (W)

The RIN is defined so that it may be easily referenced to the electrical noise power in the receiver. The photo-current at the output of the photodetector is directly proportional

to the received optical power, therefore the electrical power at the input to the preamplifier is proportional to the square of the received optical power. Consequently the power spectral density of the noise current in the photodetector output, due to fluctuations in the laser output is calculated by multiplying the square of the received dc photocurrent with the RIN. Using (2.35) the noise current power spectral density (A^2/Hz) may be calculated as.

$$i_{RIN}^2 = RIN \cdot (I_{photo-dc})^2 \quad (2.36)$$

Relative intensity noise is the instantaneous deviation of the output power level due to the random photon density fluctuations of each lasing mode sustained in the cavity. These fluctuations are excited by the quantum processes inside the laser cavity which include the shot noise of the injection current, the spontaneous recombination of carriers within the active layer, light absorption and scattering, induced backward reflections into the cavity and stimulated emission. The basic RIN driving mechanism can be represented as an addition of a shot noise variable term to the multimode rate equations, by inserting a shot noise distributed carrier density term to (2.6) and a shot noise distributed photon density term to (2.7) in each mode, these terms are known as Langevin noise terms [32].

These shot noise distributed terms disturb the multimode lasing process by randomly increasing the photon and carrier densities, which in turn alters the instantaneous stimulated emission gain in the cavity as a function of wavelength. This change in gain disturbs the photon densities in all other modes, causing an increase in some modes while lowering the photon densities in others. The detected photon density at the receiver is a superposition of all the photon densities of the different longitudinal lasing modes, so as the individual mode intensities fluctuate their sum creates a net intensity fluctuation or RIN, most of which cancels out. This is a result of there being essentially only one carrier reservoir for all the lasing modes which stabilizes the number of photons in the cavity by regulating the gain in the stimulated emission process [47]. If not all of the lasing modes are equally detected at the receiver, (ie. unequal transmission loss and unequal delay for all

lasing wavelengths) this cancellation phenomenon is degraded and results in mode partition noise. In our system model the transmission distance is short and dispersion is negligible (see Section 2.2), therefore RIN enhanced by mode partition noise is negligible and was ignored.

Since RIN is the response of the rate equations to Langevan noise terms, its characteristics are influenced by the nonlinear resonant coupling between the photons and the injected carriers. Statistically it is difficult to say how the RIN's pdf is distributed because its wideband spectral properties are nonuniform and signal dependant. However, in the scope of this work it is reasonable to suggest that it may be treated as Gaussian noise.

Analytically the frequency characteristic of RIN is given in [33] as:

$$RIN(\omega) = \frac{\left(A + \left(\frac{2\beta N}{\tau_n S} \right) \omega^2 \right)}{\left((\omega^2 - \omega_0^2)^2 + (\alpha\omega)^2 \right)} \quad (2.37)$$

where:

- α - $I_{bias}/(I_{th} \tau_n)$ = damping constant [34]
- β -spontaneous emission factor (dimensionless)
- I_{bias} - junction drive current (mA)
- I_{th} - junction threshold current (mA)
- N - average carrier density ($1/m^3$)
- S - average photon density ($1/m^3$)
- τ_n -spontaneous recombination lifetime of a carrier (sec)
- A - constant RIN value at frequencies well below resonance (dimensionless)
- ω_0 - natural resonance frequency (rad/sec)

As characterized by (2.37) RIN is a function of frequency and increases in amplitude with increasing frequency to a maximum resonant peak at the laser's natural resonance frequency ($f_r = \omega_0/2\pi$). This is demonstrated in Figure 2.10 which shows the expected RIN level for 1.3 μ m InGaAsP-BH laser characterized by Tucker, with $f_r = 10$ GHz.

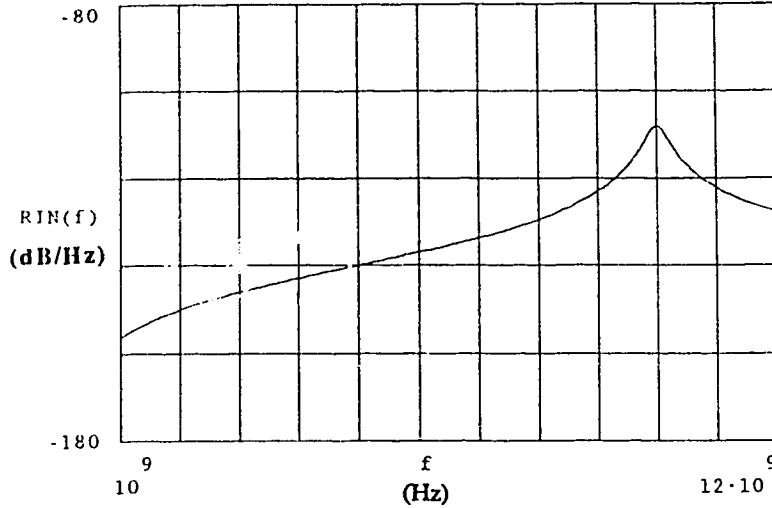


Figure 2.10: Expected RIN Characteristic of the 1.3 μm InGaAsP-BH laser characterized by Tucker, with $f_r = 10 \text{ GHz}$

SCM channels are assumed to be placed near f_r , therefore the most RIN will be experienced by channels placed near this frequency. Since our analysis is based on a worst case noise and distortion analysis as outlined in Section 2, let us adopt the maximum RIN level of the laser near resonance to be the worst case RIN for application in the system SNR calculations in Chapter 4. Note that there is room for optimization in a real system by lowering signal power in channels which experience less RIN and adding this signal power to channels immersed in higher RIN levels. However this optimization was not pursued in our system study because a worst case analysis was assumed.

It has also been shown [35] that as the bias current increases, the level of RIN at a given frequency decreases as

$$\text{RIN}(\omega) \sim \left(\frac{I_{\text{bias}}}{I_{\text{th}}} - 1 \right)^{-3} \quad (2.38)$$

Therefore as the bias current increases, RIN decreases at a rate of approximately 30 dB per decade (electrically, after detection). This was experimentally verified in [34].

Just as resonance distortion may be enhanced in the presence of back-reflected light the RIN may also be increased by 10 to 20 dB. Therefore to minimize RIN, it is necessary

in a practical system to use an optical isolator with a reflected power ratio of less than approximately -60 dB [2] & [24]. However, an optical isolator may cause up to a 4.5 dB optical insertion loss [36] which must be accounted for in the optical power budget.

Some work has been completed and more work continues, to reduce the RIN levels of semiconductor lasers. An example of this is [33] where by lengthening the cavity of an InGaAsP laser from 100- μm to 300- μm Hill found that the level of RIN was reduced by nearly 8 dB. RIN levels of less than -140 dB/Hz have been reported (-145 dB/Hz [34] and -155 dB/Hz [23]) in the most recent publications. A commercial semiconductor laser, including an optical isolator, is presently being released from ORTEL Corp. (#1530B) having 12 GHz direct modulation bandwidth with RIN less than -145 dB/Hz for $f < 2\text{GHz}$, less than -140 dB/Hz for $2\text{GHz} < f < 6\text{GHz}$, and less than -130 dB/Hz for $f > 6\text{GHz}$. Recently maximum RIN $< -140\text{ dB/Hz}$ has been reported [34]. It is therefore safe to assume that a semiconductor laser with RIN $< -140\text{ dB/Hz}$ up to near the resonance frequency will be commercially available soon. So for this analysis let us assume that maximum RIN of the laser in our system is -140 dB/Hz instead of -110 dB/Hz shown in Figure 2.10.

2.2 PASSIVE OPTICAL COMPONENTS

Consider now the optical transmission components and the receiver. As discussed in the Sections 2.1.1b and 2.1.6, it is required that an optical isolator be used to minimize distortion and RIN enhancing back-reflections into the laser. The insertion loss from this device is assumed to be 4.5 dB of optical power [36]. A single mode fibre at 1.3 μm is assumed to be used to match the wavelength of operation for a InGaAsP laser in the low OH absorption window, to minimize dispersion at the 1.3 μm zero dispersion wavelength, and to avoid modal noise which arises when multimode fibre is used [37]. Modal noise was also confirmed in our lab on a simple analog multimode fibre link to be the limiting noise in the system.

Coupling efficiency into the single mode fibre is assumed to be approximately 25% (equivalent to an optical loss of 6 dB) which is achievable in the laboratory. The optical link distance in the application was assumed to be 100 m. Therefore once coupled into the fibre, the low loss (0.45 dB/km optical loss when operating at 1.3 μm [30]) results in only 0.05 dB of fibre attenuation. For operating a practical system it will be required to have a connector at each end of the fibre for installation purposes, therefore assume approximately 1 dB of optical loss to account for two connectors.

The problem however with using poor connectors is that interferometric noise may result from multiple reflections [24]. In the case of two connectors with power reflection coefficients R_1 and R_2 , the received light signal will contain a reflected wave $e(t)$ and a multiply reflected wave delayed by τ , $R_1R_2 e(t-\tau)$, (see Figure 2.11).

$$e(t)_{rx} = e(t) + R_1R_2e(t-\tau) \quad (2.39)$$

When the total signal is detected at the photodiode by direct detection, the squaring process will produce a cross product $[R_1R_2 e(t-\tau) e(t)]$ along with the normal $e^2(t)$ signal and a negligible $[R_1R_2 e(t-\tau)]^2$ term. Since $e(t)$ has the form of $A\cos(\omega_c t + \Phi(t))$ in the optical domain, where $\Phi(t)$ is the random phase noise of the optical carrier, the cross product will appear as $R_1R_2A^2\cos[\Phi(t)-\Phi(t-\tau)/2]$ with a zero difference frequency and a nonzero phase difference. Since $\Phi(t)$ is random this will create random amplitude fluctuations which can be interpreted as an additional source of intensity noise. Multiple connector reflections will therefore convert phase noise of the optical carrier into relative intensity noise at the receiver after detection. Thus it is advisable to minimize connector reflections, possibly even use fusion splices solely for this purpose. In our system interferometric noise was assumed to be negligible, however when implementing this type of system it must be considered.

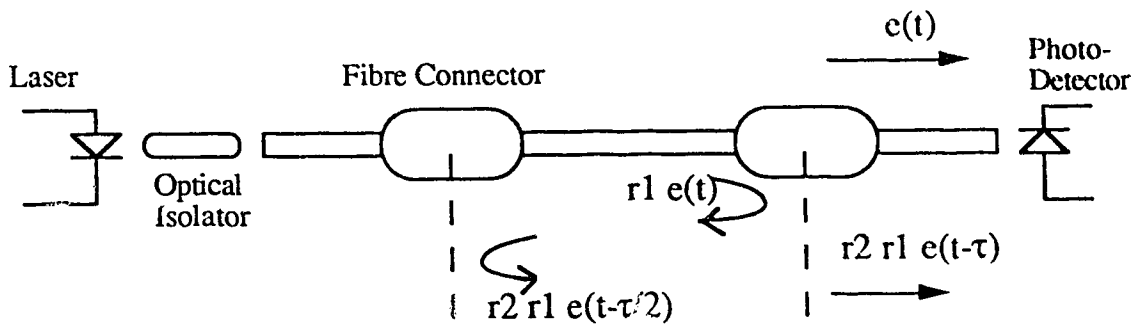


Figure 2.11- Interferometric Noise from Multiple Connector Reflections

In single mode fibre systems signal dispersion arises only from the velocity of the light varying in the core as a function of wavelength (known as intramodal or chromatic dispersion). Since the source in this system is assumed to be a multimode laser it has a light spectrum that spans a finite optical band of wavelengths, $\Delta\lambda$. Dispersion is calculated from the material dispersion parameter of the fibre, given in units of ps/(nm km). The main reason for operating at a centre wavelength of 1.3 μm is to access the near zero dispersion window of silica at that wavelength. What is relevant is the difference in phase and attenuation between the extremes of one information channel which is $2B$ wide. To test the phase and amplitude difference the dispersion experienced by a tone at $(10 \text{ GHz} - B)$ and $(10 \text{ GHz} + B)$ was calculated where $B=100 \text{ MHz}$. Assuming a material dispersion parameter of 3.5 ps/(nm km), and a multimode laser with 1nm mode separation between each of 7 modes (taken from an InGaAsP-BH laser used by Bowers in [19]) then in a 100 m distance transmitting two tones near 10 GHz results in a net attenuation of only 0.3% and a phase offset of approximately 1.5 degrees for each tone. On a per channel basis, the effects of dispersion through a 100 m transport distance on the SCM payload are negligible and will be ignored in this analysis. Consequently transmission of the optical signal is assumed to be distortionless.

The light at the receiver is coupled into a photodetector, converted to an electrical signal and then electrically amplified by a low noise wideband amplifier. It is assumed that only a 1 dB optical loss will be incurred by coupling into the photodetector. See Table 2.1

for a summary of optical losses. Assuming 7.5 mW was output from the laser [35] and that there has been only 12.5 dB of optical loss between the laser and the photodetector, the amount of light coupled into the photodetector is approximately 0.4 mW. Assuming that 10 GHz of direct modulation bandwidth is being used a photodetector with frequency response greater than 10 GHz is required which can receive this large power level. Due to the high received power it is not feasible to use an avalanche photo-diode (APD); therefore a PIN must be used. A device able to handle 0.4 mW received power without saturation modulated at up to 10 GHz, is commercially available from ORTEL Corp., (#2515B Photodiode Module). This device has a 3dB frequency response of 12 GHz and a responsivity of 0.6 A/W. Therefore we adopt this device, or one very similar to it as the photodetector in our system. The received photo-current is then approximately 250 μ A at the output of the photodiode.

This photo-current is then fed into a wideband amplifier that can preamplify the complete 10 GHz wide signal for further amplification and demodulation. This amplification is defined to be distortionless in our system but may be accounted for in a real system by applying penalties to the link budget margin. Conventional fibre optic receivers have contained either a transimpedance or integrating first stage and has provided amplification for signals only up to the low GHz range. Bandwidth requirements in SCM and direct detection receivers however, may span over several decades of frequency (0-10 GHz), and therefore conventional microwave design techniques are not generally applicable. Thus a need for a new family of amplifiers arose. Recently it has been reported by Gimlet in [37] that a 16 GHz bandwidth pin/HEMT (high electron mobility transistor) receiver combining both integrating and transimpedance amplifier techniques as developed. It was fabricated on a hybrid integrated circuit, and resulted in a maximum noise current spectral density of 12 $\text{pA}/\sqrt{\text{Hz}}$. An amplifier was also constructed by Viola [38] using discrete commercial devices resulting in a bandwidth of 10 GHz with a maximum noise current spectral density of 13 $\text{pA}/\sqrt{\text{Hz}}$. Assume that an amplifier of this type is used in our

system, with at least a 10 GHz wide direct amplification bandwidth and an rms noise spectral current density of $12 \text{ pA}/\sqrt{\text{Hz}}$. As a consequence of the amplifier bandwidth constraint it was assumed that the modulation bandwidth of the optical link be limited to 10 GHz. Since InGaAsP lasers exist with modulation bandwidths in excess of 10 GHz, biasing the laser model at a relaxation frequency of 10 GHz as stated earlier is a reasonable assumption.

Table 2.1: Summary of Optical Losses

<u>Source of Degradation</u>	<u>Optical Loss (dB)</u>
optical isolator	4.5 dB
coupling into fibre	6 dB
connector losses	1 dB
single mode fibre loss	0.05 dB
coupling into detector	<u>1 dB</u>
	12.5 dB or Loss = 17.8

The received photo-current is therefore given by

$$I_{\text{Photo-Current}} = R_{\text{responsivity}} \cdot \frac{P_{\text{Laser}}}{L_{\text{Loss}}} = 0.6 \frac{\text{mA}}{\text{mW}} \frac{7.5 \text{ mW}}{17.8} = 250 \mu\text{A} \quad (2.40)$$

As stated above, transmission of the optical signal to the receiver is distortionless. Therefore it may be modelled simply by scaling the steady state photon density output from the laser at a bias yielding $f_{\text{relax}} = 10 \text{ GHz}$, to become a dc photo-current of $250 \mu\text{A}$ at the receiver. This may be accomplished by defining an optical scaling coefficient (G) where S_o was calculated in Section 2.1.3 using (2.19) and (2.20):

$$G = \frac{I_{\text{Photo-dc}}}{S_o} = \frac{250 \mu\text{A}}{1.6 \cdot 10^{21} \text{ m}^{-3}} = 1.5625 \cdot 10^{-24} \mu\text{A m}^3 = \frac{1}{6.4 \cdot 10^{24}} \mu\text{A m}^3 \quad (2.41)$$

This scaling coefficient was placed in the large signal laser rate equation module and is shown in Figure 2.2a. The output of the laser module is then the expected dc large signal photo-current after detection in our receiver.

2.3 SUMMARY OF NOISE CONTRIBUTIONS AND SYSTEM ASSUMPTIONS

In considering the total noise in the assumed system, we referenced all the noise to the input of the preamplifier, since it is the most commonly used point of reference in optical systems. Given that the received photocurrent after the above optical loss calculations is 250 μA , the noise contributions from RIN, shot noise, and preamplifier noise are as follows.

Noise levels:

- i) RIN (= -140 dB/Hz) - Contributions from laser's RIN only. Assume contributions from interferometric noise is zero

$$N_{\text{RIN}} = (10^{-14} \frac{1}{\text{Hz}}) \times (I_{\text{photo-DC}})^2 = 10^{-14} \frac{1}{\text{Hz}} (250 \mu\text{A})^2$$

$$N_{\text{RIN}} = 635 \cdot 10^{-24} \frac{\text{A}^2}{\text{Hz}}$$

- ii) SHOT NOISE

$$N_{\text{Shot}} = 2 e \times I_{\text{photo-DC}}$$

$$N_{\text{Shot}} = (2 \cdot 1.602 \cdot 10^{-19} \frac{\text{A}}{\text{Hz}}) \cdot 250 \cdot 10^{-6} \text{ A}$$

$$N_{\text{Shot}} = 80.74 \cdot 10^{-24} \frac{\text{A}^2}{\text{Hz}}$$

- iii) PREAMP NOISE CURRENT: assumed $i_{\text{n-amp}} = 12 \text{ pA}/\sqrt{\text{Hz}}$

$$N_{\text{PreAmp}} = 144 \cdot 10^{-24} \frac{\text{A}^2}{\text{Hz}}$$

Therefore:

$$N_{\text{Total}} = N_{\text{RIN}} + N_{\text{Shot}} + N_{\text{Pre-Amp}}$$

$$N_{\text{Total}} = (63.5 + 8.07 + 14.4) \cdot 10^{-23} \frac{\text{A}^2}{\text{Hz}}$$

$$N_{\text{Total}} = 86 \cdot 10^{-23} \frac{\text{A}^2}{\text{Hz}} \quad \text{or} \quad i_{\text{n}} = \sqrt{N_{\text{Total}}} = 29.3 \frac{\text{pA}}{\sqrt{\text{Hz}}}$$

This is the equivalent rms noise power current spectral density at the input to the preamplifier and it will be used to estimate the signal to noise ratio of the microwave payload on this particular optical link from the worst case eye diagram analysis after introducing laser resonance distortion. Since the noise is RIN dominated, its statistics will be signal dependant. However due to the scope of this work it has been assumed that the noise is Gaussian for purposes of BER calculations.

In summary, the assumptions and reasoning used to model signal degradations in the lightwave link are as follows:.

SUMMARY OF LIGHTWAVE LINK MODELLING APPROACH AND ASSUMPTIONS

* Approach:

Modelled the worst case influence of distortion and noise on the digital SCM signal. This was accomplished by modelling laser resonance distortion, calculating of the received signal eye opening, and also the noise spectral density of worst case channel position. These factors are used for BER calculations in Chapter 4.

* Assumptions:

A. Laser: 1.3 μm InGaAsP-BH laser designed for SCM applications [2]

1.) Distortion:

- nonlinearity of the light current curve
 - sublinearity at high bias points; static characteristic; not modelled
 - threshold region; introduces clipping distortion; modelled by rate equations
- resonance distortion is more significant than sublinearity of light current curve at frequencies in same decade as resonance frequency [23], [24] & [25]
 - modelled by the single mode rate equations using parameters measured by Tucker for a laser of this type [20], it was conservative for 2HD

2.) Frequency Response:

- Available modulation bandwidth of 10 GHz;
- Implicitly modelled in rate equations
- Laser biased at $I_{\text{bias}} = 7I_{\text{threshold}}$ to achieve relaxation frequency = 10 GHz;

3.) Noise:

- Relative intensity noise < -140 dB/Hz over the band of interest

4.) Power Output:

- 7.5 mW at $I_{\text{bias}} = 7I_{\text{threshold}}$ [35]

B. Optical Isolator: placed between laser and fibre:

- minimizes back reflections which enhance RIN and resonance distortion
- has 4.5 dB optical insertion loss

C. Fibre:

- single mode to avoid modal noise
- centered at 1.3 μm to match the wavelength and minimize dispersion
- 0.05 dB optical loss per km with 1dB for connector losses

D. Detector

- PIN photodetector capable of receiving 0.5 mW optical power modulated at up to 10 GHz, with a responsivity of 0.6 mA/mW.
- Received power of 0.42 mW, resulting in a dc photo-current = 250 μA
- 10 GHz bandwidth preamplifier with equivalent noise current = 12 $\text{pA}/\sqrt{\text{Hz}}$
- Equivalent system rms noise spectral density at the input to the preamplifier of

$$i_n = \sqrt{N_{\text{Total}}} = 29.3 \frac{\text{pA}}{\sqrt{\text{Hz}}}$$

Chapter 3

MODIFIED ORTHOGONAL SUBCARRIER MULTIPLEXING TRANSMISSION TECHNIQUES FOR A DIGITAL LIGHTWAVE SYSTEM

In Chapter 2 the physical transmission link was discussed and the dominant degradation effects on the SCM signal were identified and modelled. In this chapter we consider how the digital SCM signal may be generated using modified orthogonal subcarrier multiplexing (or modified orthogonal SCM). After this introduction, the technique of orthogonal subcarrier multiplexing also known as orthogonal multiplexing [39], [41] - [46] and its properties are given in Section 3.1. Following in Section 3.2 is a presentation of what change was introduced to constitute modified orthogonal SCM and why it is well suited for a multi-Gbit/s payload transmission on an optical SCM link. In Section 3.3 the possible configurations of modified orthogonal SCM are considered and the corresponding BOSS simulation modules are given. Section 3.4 then presents some preliminary ideas for carrier and clock recovery in the receiver.

Referring back to Section 1.2.3 (Digital Subcarrier Multiplexing) the transmission of a group of parallel bit streams is accomplished in a subcarrier multiplexed system by keying each of the carriers with a combination of one or more parallel bit streams. The modulated carriers are spaced such that there is a guard band between channels after filtering, and little or no interchannel interference (ICI) results. This technique is commonly used in conventional frequency division multiplexing systems (FDM), and has been the only method identified for use in the area of digital subcarrier multiplexing. See Figure 3.1 for a typical FDM spectrum.

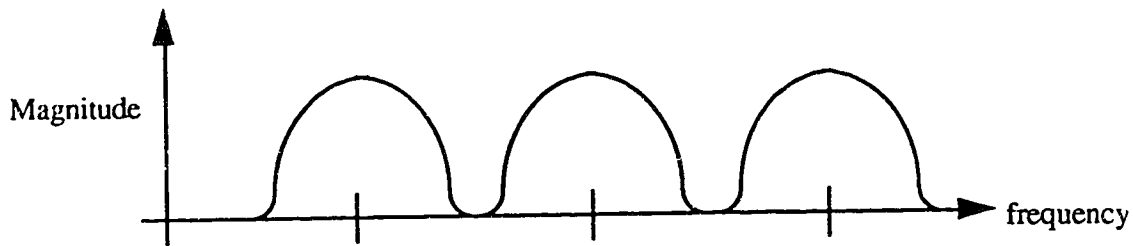


Figure 3.1- A Conventional FDM Spectrum

Optical subcarrier links of today have the properties of a very wide modulation bandwidth and a limited power budget. Transmission of multi-Gbit/s parallel payloads by SCM has resulted in the use of robust digital modulation formats such as binary frequency shift keying (BFSK) [10], or binary phase shift keying (BPSK) [11] & [14] which are bandwidth inefficient. BFSK and BPSK systems typically attain bandwidth efficiencies of 0.5 bit/s/Hz, which is poor compared to the 8-PSK and 16-QAM SCM systems demonstrated in [12]. However by comparison, BFSK and BPSK are less expensive to generate and more robust because they have good immunity to noise and distortion introduced by the optical link.

The system designer is faced with the problem of maximizing the overall data rate and minimizing interchannel interferences. In certain applications, the channels may operate at equally spaced centre frequencies, transmit at the same data rate, and the signalling intervals of different channels can be synchronized. For this class of FDM applications, orthogonal SCM techniques may be considered.

Orthogonal SCM is a multichannel multiplexing technique where the equispaced carriers are phase related, and amplitude modulated such that their channels are bandlimited and orthogonal. This permits significant spectral overlap between channels which improves bandwidth efficiency, and sharp bandpass channel filtering is not required. The parallel data streams at the input to our communication system all operate at the same data rate and are synchronized in time. Consequently orthogonal SCM was chosen to be considered in our system rather than conventional FDM techniques such as PSK, FSK or QAM. See Figure 3.2 for the spectrum of an orthogonal SCM signal.

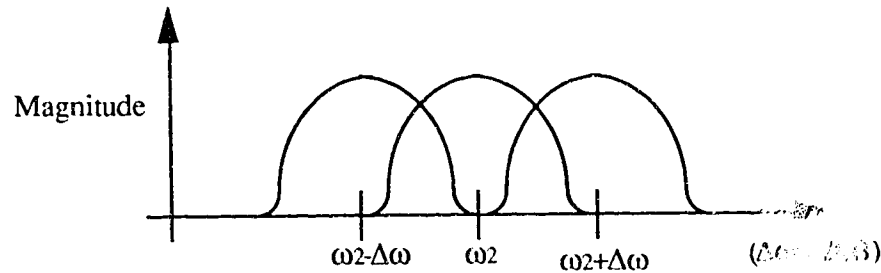


Figure 3.2- An Orthogonal SCM Spectrum

An orthogonal SCM signal is generated as follows. The channel carriers must be amplitude shift keyed at the same data rate (B) with their signalling intervals aligned in time and carriers equally spaced B Hz apart. For orthogonality to be maintained, adjacent channel carriers must be staggered with phase offsets of 90 degrees; for example the carriers of a three channel system may be $\cos(\omega t)$, $\sin((\omega+2\pi B)t)$ and $\cos((\omega+4\pi B)t)$. Other requirements for orthogonal SCM are given by Chang [39] and state that for no ICI to occur, the baseband pulse spectrum must be bandlimited to B Hz before modulating the appropriate carrier, and satisfy certain phase criterion (see Sect. 3.1.1). To bandlimit the baseband spectrum to B Hz, Nyquist pulse shaping may be used. By using square root Nyquist filtering in both the transmitter and receiver, a zero intersymbol interference (ISI) condition is maintained and optimum performance in the presence of white Gaussian noise is assured [41]. Orthogonal channels may be separated at the receiver by multiplying the received signal with the appropriate phase locked $\sin(\omega t)$ or $\cos(\omega t)$ local oscillator and applying low pass filtering.

Nyquist shaping and filtering is not suitable in this application because of the very high tributary data rate of 200 Mbit/s in our system, making it an expensive alternative. Consequently it was assumed that the Nyquist constraints be relaxed, implying that the baseband pulse spectrum is no longer bandlimited. It was found that adjacent channels need not be bandlimited to be orthogonal (see Section 3.2.1); this condition was not considered in earlier work [39] & [41]. As a result, suitable nonbandlimited baseband

pulse shapes were selected which satisfied Chang's phase criteria, and a simple Butterworth low pass filter was chosen in the receiver for demodulation. This new technique has been termed "modified orthogonal multiplexing" and the results of this work indicate that it is a suitable technique for a multigigabit digital SCM system

3.1 ORTHOGONAL SUBCARRIER MULTIPLEXING

For a background description of orthogonal SCM consider the following two subsections. First Chang's criteria [39] are stated in Section 3.1.1 describing the conditions under which orthogonality is maintained between adjacent channels. This is followed in Section 3.1.2 by a description of an orthogonal SCM QAM system (also known as O-QAM) presented and analyzed by Saltzberg in [41]. After laying the necessary background, Section 3.2 goes on to explain the principles and techniques of modified orthogonal SCM. Modified orthogonal SCM allows removal of the bandlimiting constraint on the baseband pulse shape. This results in a simplified implementation with an acceptable level of signal degradation arising from ICI due to nonorthogonal, nonbandlimited channels.

3.1.1 Chang's Criteria for Orthogonal SCM

In [39] Chang describes the general conditions of synthesizing channel spectra suitable for orthogonal SCM. It was shown that if the following criteria are met, then channels will be orthogonal to each other and no interchannel interference will result. For the simplicity of explaining how this method works, the criteria for orthogonality are stated in the context of not using quadrature carriers for each channel (ie. no QAM). The case of using orthogonal SCM QAM channels is described in Section 3.1.2.

The criteria for maintaining orthogonality between channels, each carrying independent data streams at a rate of B bit/s are as follows.

- (1) Baseband pulse spectrum $F(\omega)$ is bandlimited to $(2\pi B)$

- (2) Synchronized data (@B symbol/sec) in all the channels with signalling intervals aligned
- (3) The channel carriers are spaced at B Hz apart in frequency
- (4) The adjacent channel carriers are offset in absolute phase by 90 degrees

Chang also outlined a specific phase requirement that the spectrum of $F(\omega)$ must possess for orthogonality of adjacent channels to be maintained. Denoting the phase spectra of adjacent channels (i) and (i+1) respectively as $\alpha_i(\omega)$ and $\alpha_{i+1}(\omega)$, Chang states that

$$(5) \quad \alpha_i(\omega) - \alpha_{i+1}(\omega) = \pm \frac{\pi}{2} + \gamma_i(\omega) \tag{3.1}$$

for: $\{ \omega_i < \omega < \omega_i + 2\pi/T \}$

where: $\gamma_i(\omega)$ is an arbitrary phase function with odd symmetry about $\omega = \omega_i + \Delta\omega/2$.

See Figure 3.3. Note that at any given frequency of spectral overlap there is a constant $\pi/2$ phase separation between the signals in adjacent channels; therefore $\gamma_i(\omega) = 0$. This satisfies criterion (5) for orthogonality.

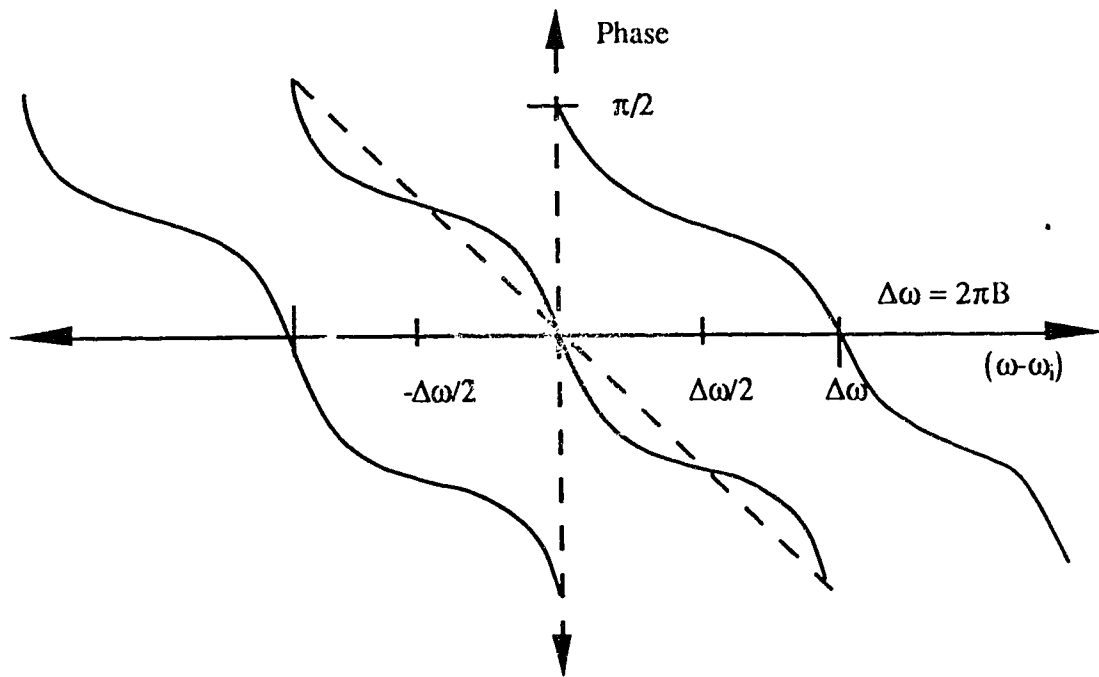


Figure 3.3- Example of a Suitable Phase Spectrum for $F(\omega)$

With these criteria it may be possible to design an orthogonal SCM system, but the most difficult constraint of this system for high bit rate applications is that the baseband pulse spectrum be bandlimited and satisfies Chang's phase requirements. A solution proposed by Chang was to use Nyquist shaped pulses to meet criteria (1) and (5). Consequently in our work we have removed criterion (1) (the bandlimiting constraint), while meeting criteria (2) through (5). This permits a more feasible implementation for high data rate systems with introduction of some penalty in performance due to interchannel interference (ICI) from nonadjacent channels and intersymbol interference (ISI).

3.1.2 An Orthogonal SCM-QAM System (O-QAM)

Described in this section is Saltzberg's orthogonal SCM QAM (O-QAM) system in which he used square root Nyquist raised cosine filtering in both the transmitter and receiver to satisfy Chang's criteria (1) and (5) and to eliminate intersymbol interference (ISI) [41]. Each channel transmits at a data rate of $2B$ where B is the bit rate in each of the input parallel data streams. The channel centre frequencies are placed B Hz apart in frequency, and the carriers are offset in adjacent channels by 90° relative to each other.

A block diagram of this system is shown in Figure 3.4. There are two groups of subchannels shown. The data symbols in the group enclosed by a dashed line are delayed by half a symbol ($1/2B$) relative to the other, and placed in quadrature. Therefore each channel transmits two independent data streams, each suppressed carrier amplitude modulating one of two quadrature carriers whose frequency is the centre of the channel. Each data stream has a bit rate of B bits/s and is staggered relative to the other in time by half a symbol or ($1/2B$). The phase of adjacent channel carriers are staggered relative to each other such that for two subchannels carrying data symbols aligned in time, the phase of a subchannel carrier is offset by 90° relative to the one in the adjacent channel.

The transmit ($F(\omega)$) and receive ($G(\omega)$) filters are identical (ie. $F(\omega)=G(\omega)$) and assumed to be real. Using the same filters in both transmitter and receiver provides matched filtering and hence optimum noise performance in the presence of white Gaussian noise. The $F(\omega)$ is specified to be bandlimited to ensure that ICI does not arise as required by criterion (1) in Section 3.1.1.

$$F(\omega) = 0 \quad \text{for } \{|\omega| \geq \frac{2\pi}{T}\} \quad (3.2)$$

Where $B= 1/T$. $F^2(\omega)$ was stipulated to meet conditions for zero intersymbol interference (ISI), and therefore it must have a Nyquist roll off.

$$F^2(\omega) + F^2\left(\omega - \frac{2\pi}{T}\right) = 1 \quad \text{for } \left\{0 \leq \omega \leq \frac{2\pi}{T}\right\} \quad (3.3)$$

The multiplexed signal before transmission will therefore have the following form.

$$\begin{aligned} s(t) = & \sum_{m \text{ odd}} \sum_{n=-\infty}^{\infty} a_{nm} f(t-nT) \sin(\omega_0+m(2\pi B))t + \sum_{m \text{ even}} \sum_{n=-\infty}^{\infty} b_{nm} f(t-nT) \cos(\omega_0+m(2\pi B))t + \\ & \sum_{m \text{ even}} \sum_{n=-\infty}^{\infty} a_{nm} f\left(t-nT-\frac{T}{2}\right) \sin(\omega_0+m(2\pi B))t + \sum_{m \text{ odd}} \sum_{n=-\infty}^{\infty} b_{nm} f\left(t-nT-\frac{T}{2}\right) \cos(\omega_0+m(2\pi B))t \end{aligned} \quad (3.4)$$

where:
$$T = \frac{1}{B} \quad (3.5)$$

and $f(t)$ is the inverse Fourier transform of $F(\omega)$, and a_{nm} and b_{nm} are the information-bearing symbols.

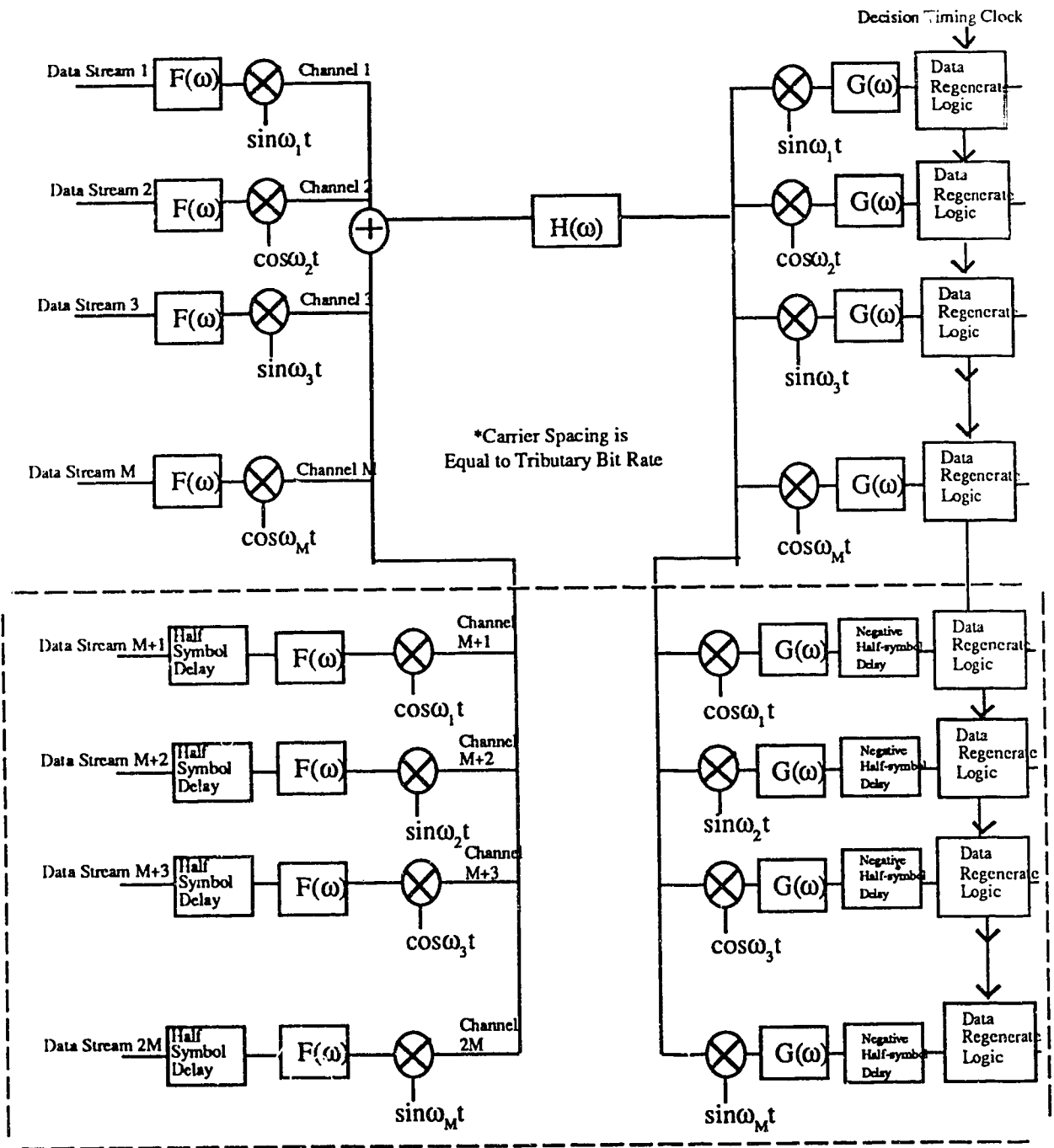


Figure 3.4- Block Diagram of an O-QAM System, Quadrature Component of Signal Encompassed by the Dashed Line

The bandwidth efficiency of this O-QAM system is given by,

Bandwidth Efficiency(O-QAM) = (total throughput data rate)/(required bandwidth)

$$\eta_{\text{O-QAM}} = \left(\frac{\left(\frac{2M}{T} \right)}{(M+1) \cdot \left(\frac{1}{T} \right)} \right) = \frac{2M}{M+1} \quad (3.6)$$

which approaches 2 bit/s/Hz if the number of channels is large. Binary level signalling is used, therefore a near Nyquist symbol rate is achieved using O-QAM.

Saltzberg observed that the performance of this system was sensitive to impairments in transmission, as well as downconversion and sampling time errors of the receiver. Assuming transmission and downconversion is ideal, the width of the received eye was such that a 12% deviation of the sampling time from its centre resulted in a symbol error. Saltzberg also found that degradation resulted when there was a phase error in downconversion, in fact he observed that this parallel system was approximately three times as sensitive as a single channel to phase errors. In the presence of delay distortion an increase in crosstalk between adjacent channels resulted, however its effects could be minimized by adapting the phase of downconversion carriers. Amplitude distortion due to the transmission medium was also considered and it was found that the increase in crosstalk was less sensitive than for delay distortion. Saltzberg concluded that in the presence of dispersive medium it is essential that the receiver separately adjusts the demodulating carrier phase and sampling time for each channel and do so with very low jitter. This receiver structure in itself makes the parallel O-QAM system outlined by Saltzberg difficult to implement.

This spectrally efficient O-QAM system is therefore an expensive one to directly implement because of the Nyquist roll-off filters and the complex receiver structure required. Most likely this is why a direct implementation of O-QAM in a practical system has not been found published in the literature. The primary application of Saltzberg's technique was intended to be in the area of voice band data transmission over the telephone

lines. This was because it offered an effective technique to correct amplitude and phase distortion of the telephone channel along with providing good immunity against impulse noise [41]. The development of digital signal processors (DSP's) over the past two decades combined with the low data transmission rates for telephone modems (kb/s range) has enabled implementation of an O-QAM system by digital synthesis and demodulation using the discrete Fourier transform (DFT) [42]-[45].

To digitally implement the O-QAM technique presented by Saltzberg, Hirosaki introduced a preprocessing stage before performing a DFT, such that the channel symbols were shaped before upconversion by an FIR filter approximating a square root raised cosine Nyquist filter [42]-[44]. The same digital filtering procedure was introduced at the receiver after performing a DFT on the sampled signal. Since the FIR filter only approximates a square root Nyquist, the signal is not completely bandlimited, however the resulting ICI will be small if the order of the FIR filter is large. Therefore synthesis using preprocessing and the DFT implemented by a DSP results in Saltzberg's O-QAM system implemented digitally, thereby avoiding the expensive filtering and complex receiver structure required in a direct implementation.

By using a fast Fourier transform (FFT) algorithm [43] along with a digital automatic equalizer at the receiver [44], Hirosaki implemented an O-QAM modem operating at 256 kb/s in a groupband from 60 kHz to 108 kHz [42]. Recently applications of this technique have also been considered for transmitting data or facsimile signals on the general switched telephone network (GSTN), high rate digital subscriber lines (HDSL) and cellular radio. Two main advantages beside high bandwidth efficiency are that the signal may be processed at the receiver without noise and interference enhancement resulting from equalization when a single carrier is used, and the long symbol time provides better immunity to fading and impulse noise [46].

3.2 MODIFIED ORTHOGONAL SCM

As described above, O-QAM has been digitally synthesized using DSP's in the kbit/s data rate range, but synthesizing a multiplexed Gbit/s payload in this way is not possible, so a direct implementation of O-QAM is necessary. Nyquist filtering is required to achieve no intersymbol interference (ISI), and channel bandlimiting for no interchannel interference (ICI). Nyquist filtering is difficult to achieve in our application because of our multi-Gbit/s data transmission rate. For an easier implementation at the price of some degradation in performance, we remove the Nyquist shaping constraint on the baseband data pulses. This implies a nonzero ISI condition, and that the baseband pulse spectrum is no longer bandlimited to $1/T$ (T =period of one data symbol) resulting in nonzero ICI. This modification may be interpreted in Figure 3.4 as choosing $F(\omega)$ and $G(\omega)$ to be non-Nyquist, and $F(\omega)$ not equal to $G(\omega)$.

Orthogonal SCM's criterion (1) (Section 3.1.1) is therefore removed; this constitutes the technique of modified orthogonal SCM. If quadrature subchannels enclosed by the dashed line are assumed to be used and is shown in Figure 3.4, it is termed modified O-QAM. The other possibility is to remove the quadrature subchannels present, this was termed modified orthogonal SCM with no quadrature subchannels. Both are encompassed by the technique of modified orthogonal SCM.

By allowing the baseband pulse to not be bandlimited to $B=1/T$ while still meeting Chang's phase criterion, it may appear that orthogonality between directly adjacent channels cannot be maintained in the modified orthogonal SCM system; this is not the case. It is shown in Section 3.2.1 that any given subchannel modulated by a cosine carrier is orthogonal to all subchannels with sine carriers and not orthogonal to all subchannels modulated with cosine carriers; the converse is also true. Channels which are not orthogonal introduce ICI in the channel of interest, resulting in signal degradation. The

selected (which satisfies Chang's phase criterion), and may be determined by computer simulation. By comparing performance of different baseband pulse shapes and system configurations of modified orthogonal SCM, the appropriate candidates may be selected for simulation in the digital SCM system.

3.2.1 Orthogonality Analysis of Nonbandlimited Channels

For a modified orthogonal SCM system it was stipulated that the baseband pulse's spectrum ($F(\omega)$ in Figure 3.4) be permitted to exceed a bandwidth of $B=1/T$ (where T is the symbol period) to remove the Nyquist filtering constraint required in O-QAM. It is shown in this section that even if the selected baseband pulse spectrum is not bandlimited to B Hz, any given subchannel on a cosine carrier is orthogonal to all subchannels on sine carriers over a symbol time. By symmetry the converse is also true for any subchannel on a sine carrier. To prove this, the interference appearing in the k th numbered cosine subchannel (where k is even from Figure 3.4) after downconversion is considered in the following analysis.

Due to symmetry in this system, only the ICI appearing in one subchannel need be considered to derive the orthogonality relationship between all channels. The results will be the same if an even or odd numbered channel or the sine or cosine subchannel is chosen (see Figure 3.4). Without any loss of generality, a cosine subchannel from an even numbered k^{th} channel (not one of the two end channels), was chosen for the following orthogonality analysis. Since it is assumed that the system is time-invariant and linear, orthogonality for the channel of interest may be observed by determining the response to a single pulse transmitted in each subchannel.

The frequency response of the transmission medium, $H(\omega)$ shown in Figure 3.4, is assumed in this orthogonality analysis to be distortionless with a transfer characteristic of

$$H(\omega) = 1 \quad (3.7)$$

transfer function $G_o(\omega)$. The purpose of the analysis is to demonstrate that ICI from certain nonadjacent subchannels is zero, therefore to avoid obscuring the picture by introducing ISI from a non-Nyquist low pass filter, define $G(\omega)$ (in Figure 3.4) to be $G_o(\omega)$ where

$$\begin{aligned} G_o(\omega) &= 1 & \text{for } \omega < \omega_k \\ &= 0 & \text{for } \omega \geq \omega_k \end{aligned} \quad (3.8)$$

$$\text{where } \omega_k = \omega_o + k(2\pi B) \quad \text{and } \omega_k \gg \omega_o$$

The stopband of $G_o(\omega)$ starts at ω_k (th k th channel position is the channel of interest) to remove the spectral image of the broadband composite signal which appears above ω_k after downconversion. The condition ($\omega_k \gg \omega_o$) was chosen so that most interfering channels in this analysis will not be removed by $G_o(\omega)$ after downconversion. Contributions of ICI to the k^{th} cosine subchannel may be made from all channels in the system because $F(\omega)$ is not bandlimited. It is necessary then to consider all sine and cosine subchannels in the system to determine which are orthogonal to the channel of interest.

The spectrum of the received signal when a single pulse is transmitted in a $(k+L)^{\text{th}}$ cosine subchannel, (where k is even and L is any positive or negative integer representing a channel number offset from k) is given in Appendix 1, Section A1.1 as:

$$\begin{aligned} S_{R_x, (k+L), \cos}(\omega) &= \frac{b_{k+L}}{2} H(\omega) F(\omega - \omega_k - 2\pi BL) \exp\left\{-j(\omega - \omega_k - 2\pi BL) \frac{T}{2} \frac{(1 - (-1)^L)}{2}\right\} \\ &+ \frac{b_{k+L}}{2} H(\omega) F(\omega + \omega_k + 2\pi BL) \exp\left\{-j(\omega + \omega_k + 2\pi BL) \frac{T}{2} \frac{(1 - (-1)^L)}{2}\right\} \end{aligned} \quad (3.9a)$$

The phase factor is due to the time displacement of the pulse by half a symbol period in $(k+L)^{\text{th}}$ channel, and consequently is nonzero for odd L . By (3.5) and (3.7) this reduces to

$$\begin{aligned} S_{R_x, (k+L), \cos}(\omega) &= (-1)^L \frac{b_{k+L}}{2} F(\omega - \omega_k - 2\pi BL) \exp\left\{-j(\omega - \omega_k) \frac{T}{4} (1 - (-1)^L)\right\} \\ &+ (-1)^L \frac{b_{k+L}}{2} F(\omega + \omega_k + 2\pi BL) \exp\left\{-j(\omega + \omega_k) \frac{T}{4} (1 - (-1)^L)\right\} \end{aligned} \quad (3.9b)$$

Multiplication by $2\cos(\omega_k t)$ and filtering by $G_o(\omega)$ yields

$$R_{(k+L),\cos}(\omega) = (-1)^L \frac{b_{k+L}}{2} [F(\omega-2\pi BL) + F(\omega+2\pi BL)] \exp\left\{-j\omega \frac{T}{4}(1-(-1)^L)\right\} \quad (3.10)$$

A single pulse transmitted in any $(k+L)^{\text{th}}$ sine subchannel yields a received signal whose spectrum is given in Appendix 1, Section A1.2 as:

$$S_{R_{x,(k+L),\sin}}(\omega) = \frac{j}{2} a_{k+L} H(\omega) F(\omega+\omega_k+2\pi BL) \exp\left\{-j(\omega+\omega_k+2\pi BL) \frac{T}{2} \frac{(1+(-1)^L)}{2}\right\} \\ - \frac{j}{2} a_{k+L} H(\omega) F(\omega-\omega_k-2\pi BL) \exp\left\{-j(\omega-\omega_k-2\pi BL) \frac{T}{2} \frac{(1+(-1)^L)}{2}\right\} \quad (3.11a)$$

Using (3.5) and (3.7) yields

$$S_{(k+L),\sin}(\omega) = \frac{j}{2} (-1)^{L-1} a_{k+L} F(\omega+\omega_k+2\pi BL) \exp\left\{-j(\omega+\omega_k) \frac{T}{4} (1+(-1)^L)\right\} \\ - \frac{j}{2} (-1)^{L-1} a_{k+L} F(\omega-\omega_k-2\pi BL) \exp\left\{-j(\omega-\omega_k) \frac{T}{4} (1+(-1)^L)\right\} \quad (3.11b)$$

Multiplication by $2\cos(\omega_k t)$ and filtering by $G(\omega)$ yields

$$R_{(k+L),\sin}(\omega) = (-1)^{L-1} \left(\frac{j}{2}\right) a_{k+L} [F(\omega+2\pi BL) - F(\omega-2\pi BL)] \exp\left\{-j\omega \frac{T}{4} (1+(-1)^L)\right\} \quad (3.12)$$

The signal appearing in time at any symbol decision instants of $t = nT$ from any $(k+L)^{\text{th}}$ numbered cosine subchannel will be

$$r_{(k+L),\cos}(nT) = \frac{1}{2\pi} \int_{-\infty}^{\infty} R_{(k+L),\cos}(\omega) \exp\{j\omega nT\} d\omega \quad (3.13)$$

Substituting (3.10) into (3.13) yields

$$r_{(k+L),\cos}(nT) = \frac{1}{2\pi} \int_{-\infty}^{\infty} (-1)^L \frac{b_{k+L}}{2} [F(\omega-2\pi BL) + F(\omega+2\pi BL)] \cos\left\{\omega \left[nT - \frac{T}{4}(1-(-1)^L)\right]\right\} d\omega \\ + \frac{j}{2\pi} \int_{-\infty}^{\infty} (-1)^L \frac{b_{k+L}}{2} [F(\omega-2\pi BL) + F(\omega+2\pi BL)] \sin\left\{\omega \left[nT - \frac{T}{4}(1-(-1)^L)\right]\right\} d\omega \quad (3.14)$$

Note that for $L=0$, (3.14) reduces to $b_k f(nT)$ where $f(t)$ is the inverse Fourier transform of $F(\omega)$. The imaginary component of (3.14) is the product of an even function $[F(\omega-2\pi BL) + F(\omega+2\pi BL)]$ (because $F(\omega)$ is real and therefore is even) and a sine function

which is odd. Therefore the integral of the imaginary component of (3.14) is zero, and (3.14) reduces to:

$$\begin{aligned} r_{(k+L),\cos(nT)} = & (-1)^L \left(\frac{b_{k+L}}{4\pi} \right) \int_{-\infty}^{\infty} F(\omega - 2\pi BL) \cos\left\{ \omega \left[nT - \frac{T}{4}(1 - (-1)^L) \right] \right\} d\omega \\ & + (-1)^L \left(\frac{b_{k+L}}{4\pi} \right) \int_{-\infty}^{\infty} F(\omega + 2\pi BL) \cos\left\{ \omega \left[nT - \frac{T}{4}(1 - (-1)^L) \right] \right\} d\omega \end{aligned} \quad (3.15)$$

Now shift the variables of integration for the first integral where

$$y = \omega + \left(\frac{2\pi}{T} \right) L$$

Similarly shift the variables of integration for the second integral where

$$x = \omega - \left(\frac{2\pi}{T} \right) L$$

The cosine products are altered by the change of variables to (where z represents either y or x):

$$\cos\left\{ \left(z \pm \left(\frac{2\pi}{T} \right) L \right) \left[nT - \frac{T}{4}(1 - (-1)^L) \right] \right\} = (-1)^L \cos\left\{ z \left[nT - \frac{T}{4}(1 - (-1)^L) \right] \right\} \quad (3.16)$$

Using (3.5), (3.16) and the shift of variables, (3.15) reduces to

$$r_{(k+L),\cos(nT)} = \frac{b_{k+L}}{4\pi} \left[\int_{-\infty}^{\infty} F(y) \cos\left\{ y \left[nT - \frac{T}{4}(1 - (-1)^L) \right] \right\} dy + \int_{-\infty}^{\infty} F(x) \cos\left\{ x \left[nT - \frac{T}{4}(1 - (-1)^L) \right] \right\} dx \right] \quad (3.17)$$

Since the two integrals are equal we get

$$r_{(k+L),\cos(nT)} = \frac{b_{k+L}}{2\pi} \int_{-\infty}^{\infty} F(z) \cos\left\{ z \left[nT - \frac{T}{4}(1 - (-1)^L) \right] \right\} dz \neq 0 \quad (3.18)$$

From (3.18) it may be observed that all cosine subchannels (for all L except L=0) contribute to ICI causing symbol distortion at any symbol decision instants of $t_n = nT$ in the channel of interest. Therefore if k is even it may be concluded that any given kth cosine subchannel is not orthogonal to all other cosine subchannels at time instants $t_n = nT$.

By a similar analysis the ICI influence from any k th sine subchannel is derived as follows. Since the product $[F(\omega+2\pi BL) - F(\omega-2\pi BL)]$ in (3.12) is an odd function of ω , the crosstalk signal appearing in time due to any $(k+L)$ th numbered sine subchannel at any symbol decisions instant $t_n=nT$ will be

$$\begin{aligned} r_{(k+L),\sin}(nT) &= (-1)^L \frac{a_{k+L}}{4\pi} \int_{-\infty}^{\infty} F(\omega+2\pi BL) \sin \left\{ \omega \left[nT - \frac{T}{4}(1+(-1)^L) \right] \right\} d\omega \\ &\quad - (-1)^L \frac{a_{k+L}}{4\pi} \int_{-\infty}^{\infty} F(\omega-2\pi BL) \sin \left\{ \omega \left[nT - \frac{T}{4}(1+(-1)^L) \right] \right\} d\omega \end{aligned} \quad (3.19)$$

Next change the variables of integration in (3.19) where $x = \omega - \left(\frac{2\pi}{T}\right)L$ for the first integral and $y = \omega + \left(\frac{2\pi}{T}\right)L$ for the second integral. The sine products are altered by the change of variables to (where z represents either x or y)

$$\sin \left\{ \left(z \pm \left(\frac{2\pi}{T}\right)L \right) \left[nT - \frac{T}{4}(1+(-1)^L) \right] \right\} = (-1)^L \sin z \left[nT - \frac{T}{4}(1+(-1)^L) \right] \quad (3.20)$$

Using (3.5), (3.20) and the shift of variables, (3.19) reduces to

$$r_{(k+L),\sin}(nT) = \frac{a_{k+L}}{4\pi} \left[\int_{-\infty}^{\infty} F(x) \sin \left\{ x \left[nT - \frac{T}{4}(1+(-1)^L) \right] \right\} dx - \int_{-\infty}^{\infty} F(y) \sin \left\{ y \left[nT - \frac{T}{4}(1+(-1)^L) \right] \right\} dy \right] \quad (3.21)$$

Since the two integrals are equal, we get:

$$r_{(k+L),\sin}(nT) = \frac{a_{k+L}}{4\pi} \left[\int_{-\infty}^{\infty} F(z) \sin \left\{ z \left[nT - \frac{T}{4}(1+(-1)^L) \right] \right\} dz - \int_{-\infty}^{\infty} F(z) \sin \left\{ z \left[nT - \frac{T}{4}(1+(-1)^L) \right] \right\} dz \right] = 0 \quad (3.22)$$

From (3.22) it may be observed that all sine subchannels (for all L) do not contribute to ICI appearing at any symbol sampling instant $t_n=nT$. Therefore if k is even it may be concluded that every k th numbered cosine subchannel is orthogonal to all sine subchannels at time instants of $t_n=nT$.

In summary it has been shown that for any given k th numbered cosine subchannel (where k is even) that it is orthogonal to all sine subchannels at time instants of $t=nT$, and not orthogonal to all other cosine subchannels. Due to the symmetry of this system the

above result may be extended for all channel positions, not just for even k . Therefore it is concluded that any subchannel in a modified O-QAM system is orthogonal to all other subchannels whose carriers are offset by $(2m+1)\times 90^\circ$ relative to the carrier phase of the channel of interest.

3.2.2 Baseband Pulse Shapes Suitable for Modified Orthogonal SCM

The modified orthogonal SCM technique requires a baseband pulse shape whose phase spectrum satisfies criterion (5) in Section 3.1.1; it is shown in this section that one solution to this criterion is to use symmetric baseband pulses. In Section 3.2.1 it was shown that subchannels on carriers offset by 90° are still orthogonal even if the channels are not bandlimited, which extended Saltzberg's analysis in [41]. The only spectral constraint then determining the selection of baseband symbol pulse candidates, is that their phase spectra satisfy criterion (5) in Section 3.1.1. The most straightforward way to satisfy this criteria is to set $\gamma_i(\omega) = 0$ in (3.1), which maintains a phase spectrum separation between adjacent channels of $\pi/2$ for all frequencies. This implies that the phase spectrum $\alpha_i(\omega)$ for a given channel at a carrier frequency of ω_i is has odd symmetry about $\omega = [\omega_i + \pi/T]$ (see Figure 3.3). The simplest solution to meet this condition for the pulse's phase spectrum is to assume that it is zero. Zero phase in $F(\omega)$ implies that all the frequencies that make up the pulse shape start at the same time, which in turn implies that the pulse shape is symmetrical in time.

It is on this zero phase criterion that the following baseband pulse shapes with nonbandlimited spectra may be considered as candidates for modified orthogonal SCM:

- Half sine shape
- Rectangular shape
- Sine square shape

To examine what happens when the phase spectrum of the baseband pulse is nonzero, pulses shaped by a Butterworth low pass filter will also be considered in simulations.

3.2.2a Half Sine Shaped Pulse

Consider first of all a half sine shaped pulse, that is:

$$f_{\text{half sine}}(t) = \begin{cases} \cos\left(\frac{\pi \cdot t}{T}\right) & \text{for } \left(-\frac{T}{2} \leq t \leq \frac{T}{2}\right) \\ = 0 & \text{Elsewhere} \end{cases} \quad (3.23)$$

The spectrum of this symbol is real and given by

$$F_{\text{half sine}}(\omega) = \left(\frac{T\pi}{2}\right) \left[\frac{\cos\left(\frac{\omega T}{2}\right)}{\left(\frac{\pi}{2}\right)^2 - \left(\frac{\omega T}{2}\right)^2} \right] \quad (3.24)$$

From (3.24) it is observed that the phase spectrum of this baseband symbol is zero as stipulated above. The half sine shaped spectrum is approximately as it appears in Figure 3.6. with a first null appearing at $f = 3/(2T)$, and every null following at $(1/T)$ intervals.

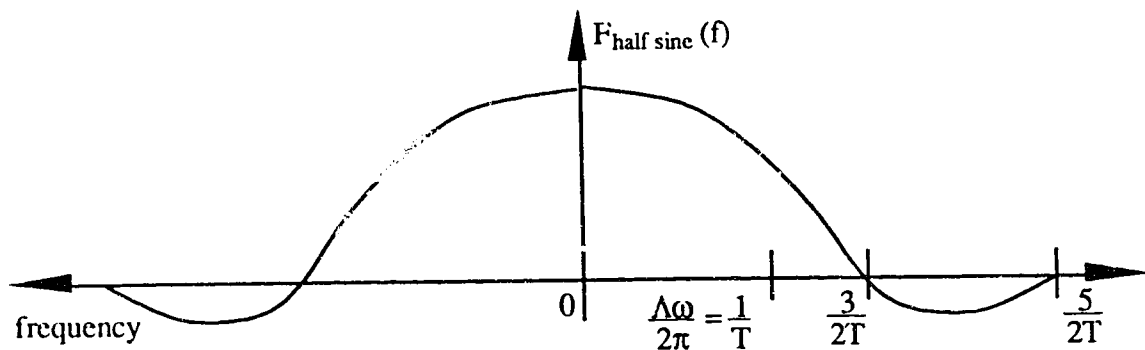


Figure 3.6 Spectrum of a Half Sine Pulse

By inspecting Figure 3.6 it may be observed that if there are five orthogonal SCM channels spaced at $(B=1/T)$ (as required in modified orthogonal SCM), the main spectral lobes from the center channel and the channel two positions away will overlap. Since a subchannel at f_k is not orthogonal to a subchannel at f_{k+2} (whose data streams are aligned in time), main lobe ICI will be introduced in the subchannel two positions away creating symbol distortion at the optimum sampling instant. ICI will also arise from the spectral tails of nonadjacent channels every second position away because they are also not orthogonal. These spectral tails roll off proportional to $1/f^2$ so the most significant ICI

contribution will be from the main lobe spectral interference. To evaluate performance with this pulse shape it is necessary to simulate (by an eye diagram analysis) an orthogonal SCM signal with interfering channels present to see how severe the ICI is from nonorthogonal channels, and to observe the penalty of using a simple Butterworth filter in the receiver. For results see Section 4.1.1b.

3.2.2b Rectangular Shaped Pulse

Next consider a rectangular shaped pulse:

$$f_{\text{rect}}(t) = \begin{cases} 1 & \text{for } \left(-\frac{T}{2} \leq t \leq \frac{T}{2}\right) \\ 0 & \text{Elsewhere} \end{cases} \quad (3.25)$$

The spectrum of this pulse is real and given by

$$F_{\text{rect}}(\omega) = T \left(\frac{\sin\left(\frac{\omega T}{2}\right)}{\omega\left(\frac{T}{2}\right)} \right) \quad (3.26)$$

A plot of (3.26) is shown in Figure 3.7

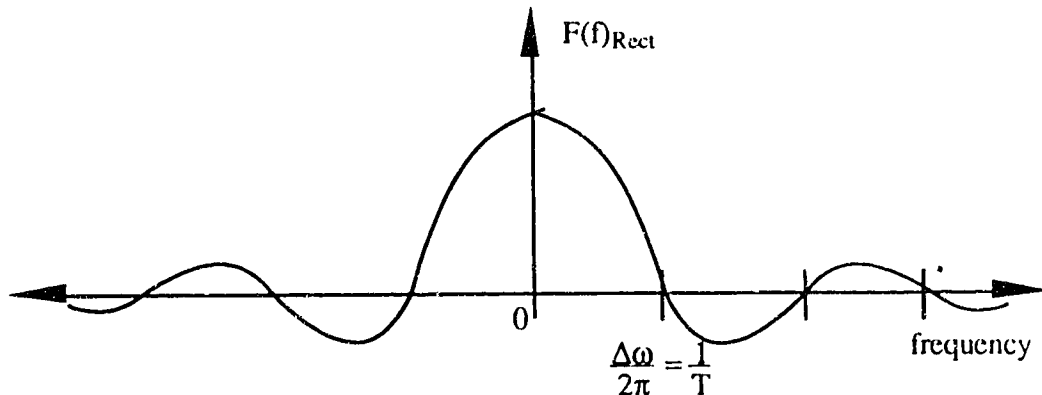


Figure 3.7: Spectrum of Rectangular Pulse

From Figure 3.7 it is observed that if there are five orthogonal SCM channels spaced at $1/T$, the main spectral lobes from non-adjacent channels do not overlap. In comparison to half sine shaped symbols there is no main lobe spectral overlap, however spectral tails are higher in amplitude. Since the spectral tails of rectangular shaped pulses roll off proportional to $1/f$, the contribution from interfering channels more than two positions

away will be more severe for rectangular than half sine shaped pulses. To evaluate the ICI and ISI performance for rectangular pulses compared to half sine shaped pulses, simulations are also required with interfering nonorthogonal channels present. For results see Section 4.1.1b.

3.3.2c Sine Square Shaped Pulse

The next baseband shape to be considered as a candidate for modified orthogonal SCM is a sine square shaped pulse which is defined as

$$f_{\text{sine square}}(t) = \cos^2\left(\frac{\pi \cdot t}{T}\right) \quad \text{for } \left\{-\frac{T}{2} \leq t \leq \frac{T}{2}\right\}$$

$$= 0 \quad \text{Elsewhere} \quad (3.27)$$

The spectrum of this pulse is real and given by

$$F_{\text{sine square}}(\omega) = \frac{1}{2} \left\{ \frac{T \sin\left(\frac{\omega T}{2}\right)}{\left(\frac{\omega T}{2}\right)} + \frac{\frac{1}{2} \sin\left[\left(\omega - \frac{2\pi}{T}\right)\frac{T}{2}\right]}{\left(\omega - \frac{2\pi}{T}\right)\frac{T}{2}} + \frac{\frac{1}{2} \sin\left[\left(\omega + \frac{2\pi}{T}\right)\frac{T}{2}\right]}{\left(\omega + \frac{2\pi}{T}\right)\frac{T}{2}} \right\}$$

or:

$$F_{\text{sine square}}(\omega) = T \cdot \sin\left(\frac{\omega T}{2}\right) \frac{\left(\omega^2 + \frac{4\pi^2}{T^2}\right)}{\omega T \left(\frac{2\pi^2}{T} - \omega^2\right)} \quad (3.28)$$

A plot of (3.28) is shown in Figure 3.8.

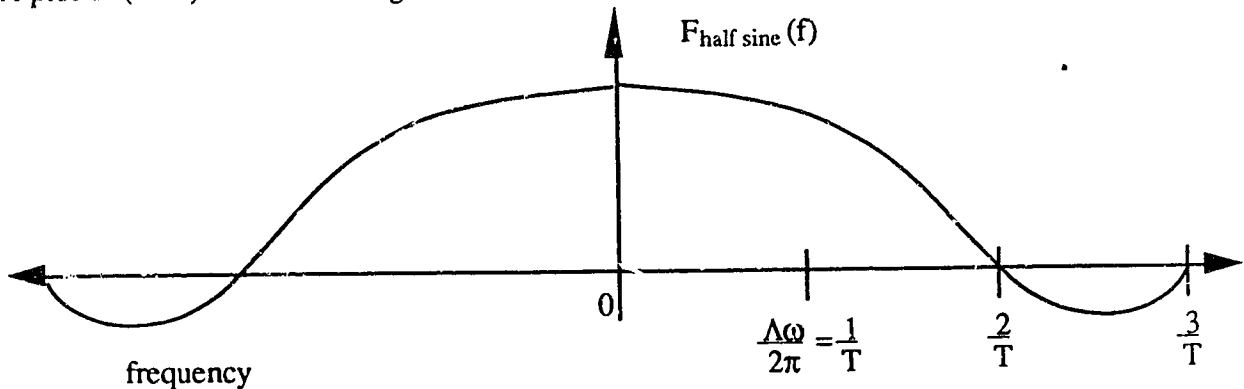


Figure 3.8 Spectrum of Sine Square Pulse

By inspecting (3.28) it is observed that the first spectral null is at $2/T$, and therefore main lobe interference from nonadjacent channels should be significant and result in more severe ICI penalties than from half sine or rectangular shapes.

3.2.2d Butterworth Low Pass Filter Shaped Pulses

To confirm that orthogonality cannot be maintained when the Chang's phase criterion is not met, consider orthogonal SCM of pulses generated by a Butterworth low pass filter. The spectrum of a rectangular pulse of duration T is given by $T \text{sinc}(\omega T/2)$, which is real and has a phase spectrum which is zero. The transfer function of a 3rd order Butterworth low pass filter has approximately a linear phase, but tapers off after its 3dB cutoff frequency [47].

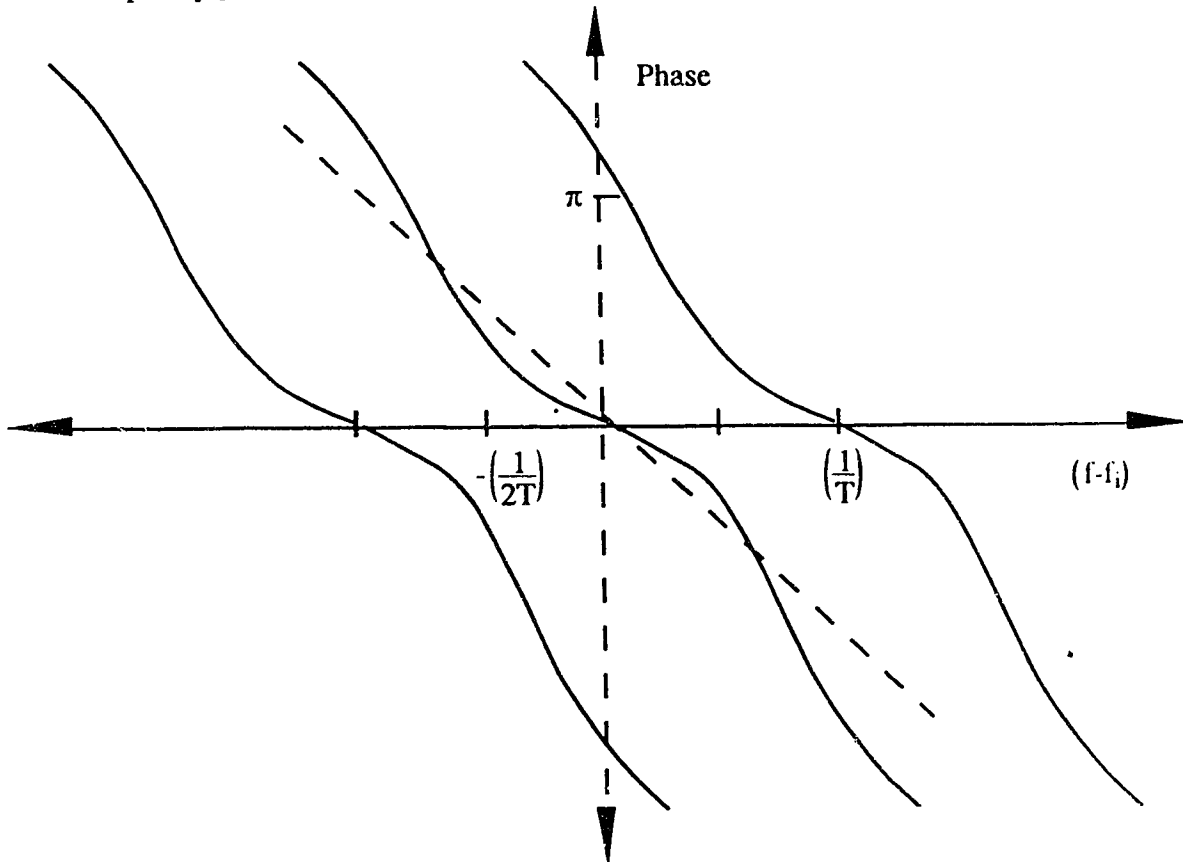


Figure 3.9 Phase Spectrum of Three Adjacent Channels with Pulses Shaped by a Butterworth LPF, 3dB Bandwidth= 100 MHz

Since the phase spectrum of the transfer function adds directly to the phase spectrum of the input signal, the output pulse phase spectrum is the same just shifted in frequency. Also assume that this symbol is multiplied up in frequency by $\cos(\omega_0 t)$ with an orthogonal multiplexed channel placed above and below, with only one symbol

transmitted. The resulting phase spectrum will appear as given by Figure 3.9. Orthogonality is lost if criterion (5) in Section 3.1.1 is violated. Criterion (5) states by (3.1) that the difference phase $\gamma_i(f)$, between two adjacent channels centered at f_i and f_{i+1} must be an odd function about $f=f_i+1/(2T)$ for orthogonality to be maintained. By inspecting Figure 3.9 it is observed that $\gamma_i(f)$ does not satisfy this criterion, therefore adjacent channels are not orthogonal and will have severe ICI penalties. See Section 4.1.1a for simulation results.

3.3 SYSTEM IMPLEMENTATIONS OF MODIFIED ORTHOGONAL SCM

There are two possible implementations of the modified orthogonal SCM system shown in Figure 3.4, modified O-QAM and modified orthogonal SCM with no quadrature subchannels. By (3.6) the modified O-QAM system has a bandwidth efficiency approaching 2 bit/s/Hz for a large number of channels. This is twice the bandwidth efficiency than the other implementation, but more ICI is present. By (3.18) ICI for modified O-QAM arises in a k^{th} cosine subchannel from the $(k+1)^{\text{th}}$ and $(k-1)^{\text{th}}$ cosine channels (the converse is also true for sine subchannels), so ICI from directly adjacent channels is nonzero. Removing all the quadrature subchannels (enclosed by the dashed line in Figure 3.4) constitutes the second implementation and results in ICI arising only from every second channel away as proven by (3.18) and (3.22).

The modified O-QAM system has twice the bandwidth efficiency than the modified orthogonal SCM system with no quadrature subchannels, but more ICI arises because directly adjacent channels are not orthogonal. Therefore a tradeoff exists between bandwidth efficiency and ICI for the two system implementations. To evaluate which implementation provides the best performance in our digital SCM system, both must be considered. Presented next is how each modified orthogonal SCM configuration was directly implemented in BOSS for each of the proposed pulse shapes.

3.3.1 Modified Orthogonal SCM System with No Quadrature Subchannels

The method of generating a modified orthogonal SCM line signal described by (3.4) (where $f(t)$ is a nonbandlimited pulse shape) with no quadrature subchannels is as follows. Channel sources operating at a tributary bit rate of $B = 200$ Mbit/s for the baseband symbol shapes of interest were placed with their centre frequencies B Hz apart and staggering the phase of every second channel carrier by 90° . The channels implemented in BOSS for the proposed baseband pulse shapes are as follows: half sine shaped pulses (Figure 3.10a); rectangular shaped pulses (Figure 3.10b); sine square shaped pulses (Figure 3.10c) and low pass filter shaped pulses (Figure 3.10d). Note that the output pulse sequences are binary amplitude shift keyed (BASK) and antipodal, (ie. positive and negative polarity mapping).

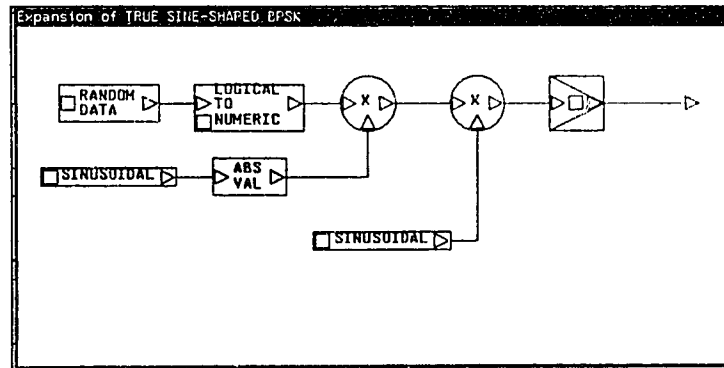


Figure 3.10a- BOSS Module, Random Source of Modulated Half Sine Shaped Pulses, No Quadrature Subchannel

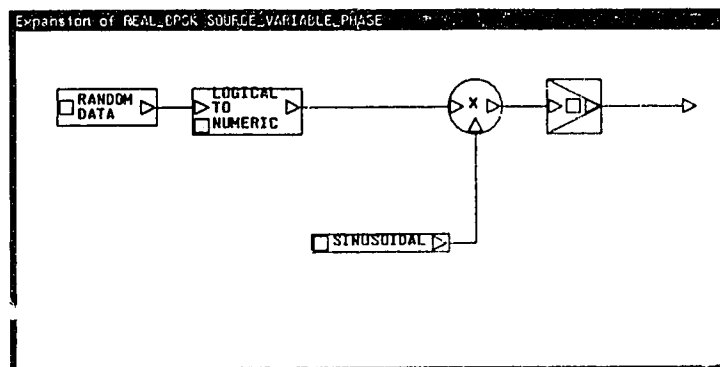


Figure 3.10b- BOSS Module, Random Source of Modulated Rectangular Pulses, No Quadrature Subchannel

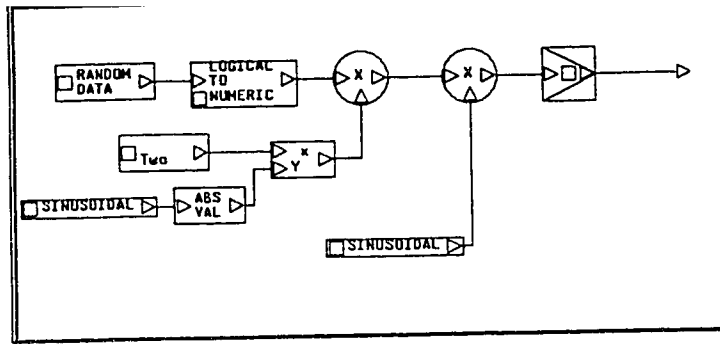


Figure 3.10c- BOSS Module, Random Source of Modulated Sine Square Pulses, No Quadrature Subchannel

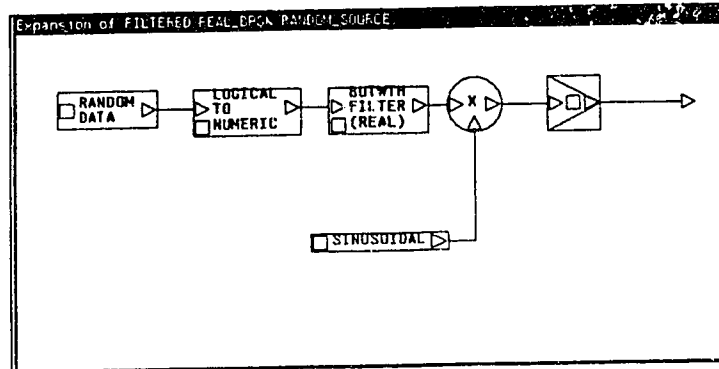


Figure 3.10d- BOSS Module, Random Source of Modulated Low Pass Filter Pulses

The receiver as implemented in BOSS is shown in Figure 3.11 and consists of an ideal multiplier and filtering to attenuate adjacent spectral terms. The low pass filter type was selected to be a Butterworth because of its availability in BOSS. Specifically it was chosen to be a 3rd order with a 3dB bandwidth of 135 MHz so as to maximize the output signal to noise ratio for the 200 Mbit/s symbol rate.

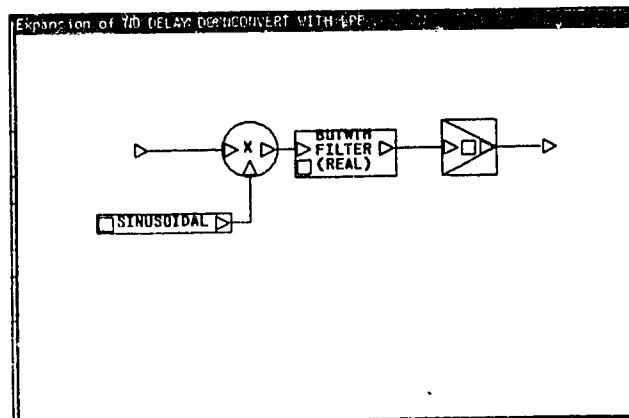


Figure 3.11- BOSS Module, Demodulator of One Subchannel

Meeting the criteria for modified orthogonal SCM results in M orthogonal SCM channels each carrying a random bit stream at B bit/sec, placed B Hz apart in frequency. The bandwidth efficiency of this system would be

$$\eta_{\text{No-Quad}} = \left[\frac{\left(\frac{M}{T}\right)}{(M+1) \cdot \left(\frac{1}{T}\right)} \right] = \frac{M}{(M+1)} \quad (3.29)$$

If M is large then a bandwidth efficiency of approximately 1 bit/sec/Hz may be achieved using double-sideband signals. This is comparable to the bandwidth efficiency of baseband transmission currently employed in conventional optical TDM systems, but in this system no logic operates at a rate greater than 200 Mbit/s.

3.3.2 Modified O-QAM

Implementation of the modified O-QAM system shown in Figure 3.4 with the proposed nonbandlimited baseband pulse shapes was accomplished as follows. Each pair of subchannels on quadrature carriers was grouped by staggering the shaped data streams by a half symbol period relative to each other. The channel centre frequencies were placed B Hz apart, with every second channel's carrier phase offset by 90°. These conditions satisfied the criteria of modified O-QAM. The modified O-QAM modulators implemented in BOSS used the half sine shaped baseband symbol as shown in Figure 3.12a, and the rectangular shaped symbol shown in Figure 3.12b. Sine square shaped symbols were not considered in the modified O-QAM implementation because simulation results with no quadrature subchannel implementation indicated that this shape would be unsuitable. The demodulator for a modified O-QAM channel is shown in Figure 3.13 and is suitable for both baseband pulse shapes.

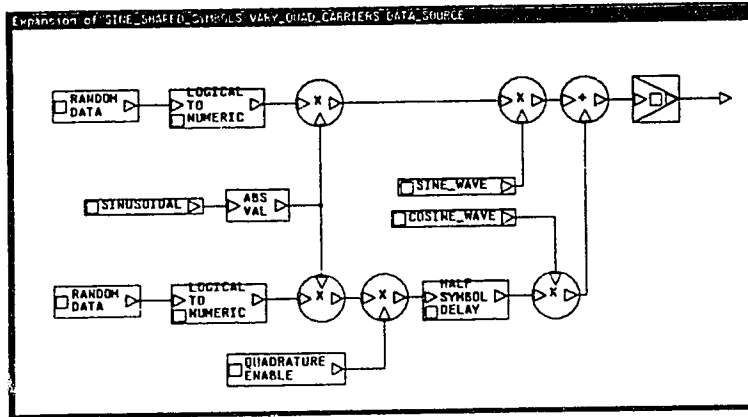


Figure 3.12a- BOSS Module, Random Source of Modulated Half Sine Shaped Pulses, Modified O-QAM

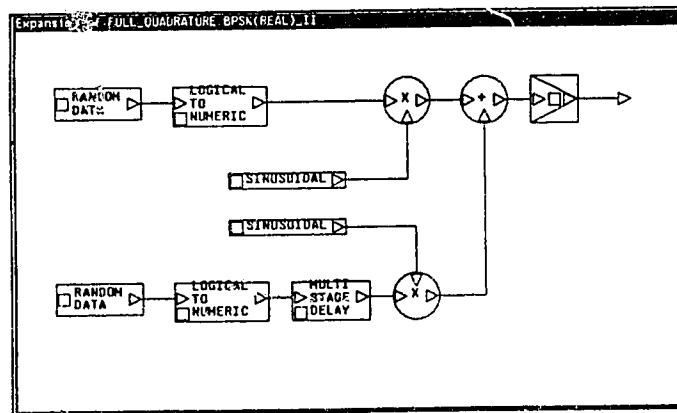


Figure 3.12b- BOSS Module, Random Source of Modulated Rectangular Shaped Pulses, Modified O-QAM

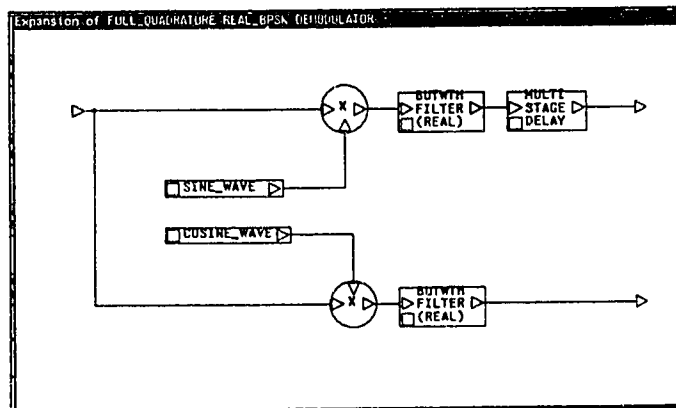


Figure 3.12c- BOSS Module of Demodulator, Modified O-QAM

3.4 POSSIBLE CARRIER AND CLOCK RECOVERY TECHNIQUES AT RECEIVER

In simulating different orthogonal SCM systems, clock recovery was assumed to be ideal. In a real system however, it is necessary to synthesize channel carriers at the transmitter and recover them at the receiver. Consider in this section some ideas as to how accomplish this.

Since the carriers are all equispaced at B Hz, it may be possible to generate these carriers by phase locking onto the harmonics of a very stable reference clock, operating at B Hz and in phase with the parallel data. This will result in carriers spaced at frequencies given by (2.30) in Section 2.1.5. This technique of carrier generation was employed in [49]. The resulting carriers must maintain acceptable phase noise levels, otherwise orthogonality between adjacent channels will not be maintained and modified orthogonal SCM will not work. If quadrature subchannels are transmitted, then generation of the quadrature carriers may be accomplished simply by a bank of 90 degree phase shifters, implemented possibly by delay lines, where each is designed for a specific frequency.

Assuming that delay distortion is not too severe in the transmission medium, it may be possible to send a "cheat clock" from which the local oscillators may be derived in receiver. If a cheat clock is sent at B Hz and recovered at the receiver, the local oscillators may be derived in a similar fashion as the carriers were derived in the transmitter. However, since channels are spaced at precisely B Hz apart, many distortion products will appear at this frequency and therefore it may be more desirable to send the cheat clock at a frequency of $B/2$. This will require a more stable cheat clock, but will avoid introducing unnecessary phase noise in the local oscillators from distortion products.

A second alternative to carrier recovery may be to cross correlate the channel of interest and an adjacent channel and use the result to drive a phase locked loop. With this

type of approach, it may be possible to adapt the local oscillator to minimize any amplitude and phase distortion effects that are introduced by the transmission medium. This may be possible because of the synchronism existing between parallel channels [48], but needs further investigation to determine if it is feasible.

The scope of this thesis has been directed to examine only the performance of the modified orthogonally multiplexed signal, assuming ideal carrier recovery in the receiver. Consequently the specific design issues of how to generate and recover these carriers was not examined any further than the discussion in this section.

Chapter 4

SIMULATION EXPERIMENTS AND RESULTS

In the first chapter of this thesis an introduction to the area of optical subcarrier multiplexing was given. In chapter two the optical transmission medium and its impairments were discussed and it was concluded that resonance distortion and relative intensity noise are the dominant source's of signal degradation at frequencies near the laser's resonance frequency. A model of resonance distortion for a modern semiconductor SCM laser was developed based on the single mode rate equations and was benchmarked by comparing single and two tone distortion test simulation results with analytical expressions given in [28]. This model was found to be conservative for second order distortion products. It was determined that the largest number of resonance distortion products arise from second order intermodulation products. With the carrier frequency plan given by (2.30) the most distortion will appear in channels near the lasers resonance frequency as demonstrated in Figure 2.9.

While keeping the transmission medium in mind, a modulation scheme which appears suitable for the optical SCM link was developed in Chapter 3. By taking advantage of the synchronism between parallel bus lines it was stated that channels could be multiplexed in frequency without any guard bands (orthogonal SCM) provided that criterion (1) through (5) in Section 3.1.1 are met. Removing the bandlimiting constraint on baseband pulses (criterion (1)) while meeting all the other criteria, constituted our proposed new technique of modified orthogonal SCM (with and without quadrature subchannels). It was proposed that since half sine, rectangular and sine square shaped baseband pulses satisfy the conditions of modified orthogonal SCM, therefore each would be evaluated as a candidate in the system simulations.

In Section 4.1 the results of an eye diagram analysis are presented which measured the ICI immunity of each of the proposed baseband pulse shapes, with and without quadrature subchannels present. The ISI introduced from the receiver Butterworth low pass filter is also examined. By trading off the noise equivalent bandwidth, ISI and ICI, the signal to noise ratio before decision was maximized. From the results presented in Section 4.1 it was concluded that only half sine and rectangular pulse shapes implemented with no quadrature subchannels present, and half sine pulse shape in the modified O-QAM implementation, were suitable to be simulated in the optical SCM environment.

Described in Section 4.2 are the simulation experiments that were performed using an eye diagram analysis to determine the relationship between transmission capacity and system margin. As explained in Chapter 2, the worst case noise and distortion was considered in this analysis. This was done to arrive at a worst case SNR. From the SNR a system margin above which a $BER < 10^{-12}$ is maintained was calculated assuming Gaussian noise statistics. Penalties from well understood nonideal system components such as mixers, amplifiers, power combiners, etc.; may be subtracted as penalties from this system margin. Therefore the system margin vs payload size curves for each modified orthogonal SCM configuration provides a measure of how feasible that system is to implement.

4.1 SIMULATION AND PERFORMANCE OF MODIFIED ORTHOGONAL SCM SIGNALS IN AN IDEAL TRANSMISSION MEDIUM

To directly compare performance of the proposed baseband pulse shapes for modified orthogonal SCM, the ISI and ICI characteristics were examined. These simulations were conducted by an eye diagram analysis with an ideal transmission medium between the transmitter and receiver, ie $H(\omega)=1$ in Figure 3.4. The ISI penalty for each baseband pulse shape was determined as follows. A single channel carrying a random bit stream with $B=200$ Mbit/s was upconverted to a carrier frequency of 2 GHz by multiplication with $\cos(\omega_c t)$, and directly connected to the receiver. There it was demodulated by multiplication with $2\cos(\omega_c t)$ and passed through a Butterworth low pass filter. By observing the maximum eye opening from the normalized eye diagram, the ISI penalty introduced by receiver filtering was measured.

Orthogonality between channels as predicted by (3.18) and (3.22) was tested by simulation as follows. To observe if ICI between directly adjacent channels is present, three channels were placed in frequency such that criteria (2) to (5) in Section 3.1.1 were satisfied, and the centre channel was demodulated in the same manner as with the single channel. By observing the maximum eye opening from the normalized eye diagram and comparing it to the previously observed ISI penalty, the ICI due to directly adjacent channels was calculated. To observe the ICI arising from two adjacent and two nonadjacent channels $2B$ away, five channels were multiplexed and the center one demodulated. To observe the ICI arising from a large number of channels, channel 25 from a composite broadband signal of 50 channels was demodulated for the case of no quadrature subchannels present; channel 13 from 25 channels was demodulated with the modified O-QAM system. The results given in Sections 4.1.1 and 4.1.2 using the method outlined above, verify the orthogonality behavior predicted by (3.18) and (3.22) and give a

figure of merit to compare performance of the different baseband symbol shapes in an ideal transmission medium.

In conducting the above simulations, a viable trade off between ICI, ISI and noise equivalent bandwidth was found which maximized the signal to noise ratio before decision, given a Butterworth low pass receiver filter. This was accomplished by varying the bandwidth and order of the Butterworth low pass filter in the receiver and observing the maximum eye opening in each case. By applying a correction factor for noise equivalent bandwidth, the condition for maximum signal to noise ratio was identified to be accomplished using a 3rd order filter with a 3dB bandwidth of 135 MHz; it was the same for all pulse shapes. Each of the baseband pulse shapes were then compared, and the best candidates selected for evaluation in the presence of laser distortion. It was found that the best performance using a system implementation with no quadrature subchannels was achieved with rectangular shaped pulses; the half sine shape was a close second. It was also found that the only suitable shape with modified O-QAM was the half sine shape. Consequently these three modified orthogonal SCM signal configurations were selected for simulations on the optical SCM link.

4.1.1 Modified Orthogonal SCM Signal- No Quadrature Subchannels

Consider the performance of modified orthogonal SCM signals with no quadrature component, as shown in Figure 3.4 exclusive of channels encircled by the dashed line and with $H(\omega)=1$. As a basis for comparing each of the proposed pulse shapes, tests of one, three, five and fifty channels were selected as explained in Section 4.1. The results of using half sine, rectangular, sine square and Butterworth low pass filter shaped pulses are presented next. The modulator and demodulator BOSS modules are shown in Section 3.3.1.

4.1.1a Half Sine Shaped Symbols

Results for the half sine shaped baseband pulse outlined in Section 3.2.2a will now be presented. Consider first the normalized eye diagram generated by demodulating the centre one of three orthogonal SCM channels (each carrying an independent random bit stream at $B = 200$ Mbits/s) shown in Figure 4.1a. The output low pass filter after downconversion was assumed to be a 3rd order Butterworth with a 3dB bandwidth (BW) of 135 MHz; the reason for choosing this filter will be made evident after analyzing the five channel case.

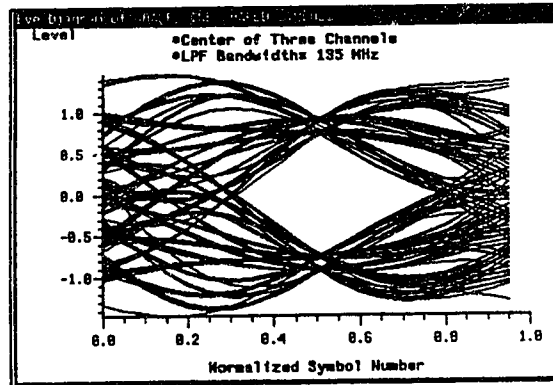


Figure 4.1a- Eye Diagram for Half Sine Shaped Pulses, Centre One of Three Channels

It is observed that a normalized maximum eye value of 0.72 was obtained at the centre of the symbol interval. Note the interference "ribs" appear at instants away from the centre of the symbol interval; this is coherent interference from directly adjacent channels as observed by Saltzberg in [41] and predicted by (3.22) at times other than the sampling time instants $t_n = NT$. Note that this eye is also inclusive of ISI effects arising from the low pass filter in the receiver. Figure 4.1b is the eye diagram generated from a channel with no adjacent channels present, and has a maximum eye value of 0.73, which shows that there is an ISI eye closure penalty of 2.7 dB due to the receive Butterworth filter. This maximum eye value is very close to that in Figure 4.1a; therefore the eye closure in Figure 4.1a is due to ISI not ICI. From this result it may be concluded that directly adjacent channels are orthogonal for half sine shaped pulses with no quadrature subchannels present. This was predicted by (3.22). Therefore ICI for this configuration only arises from nonorthogonal, nonadjacent channels.

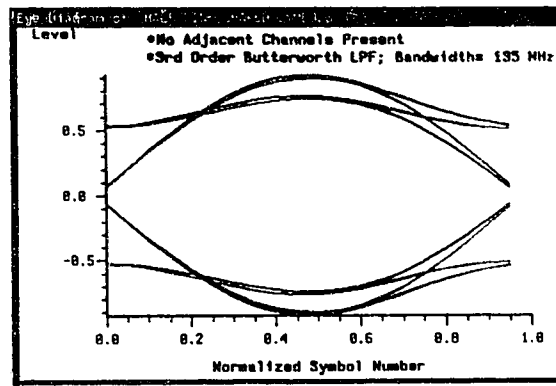


Figure 4.1b- Eye Diagram for Half Sine Shaped Pulses, Single Channel Present

To observe the effects of ICI from two nonorthogonal, nonadjacent channels, a five channel orthogonal SCM signal was generated and the centre channel demodulated in the same manner as in the three channel case. By inspecting Figure 4.2 it is observed that the maximum eye opening is 0.67. Compared to the maximum value of the eye for the stand alone channel, the ICI that arises with two nonadjacent, nonorthogonal channels present is 0.7 dB.

To observe the ICI arising from a large number of channels, channel 25 from a broadband composite signal of 50 channels was demodulated and the eye is shown in Figure 4.17c (for comparison with worst case eye inclusive of laser distortion). An eye opening of 0.66 was observed which corresponds to a further 0.1 dB decrease in eye opening. Therefore it may be concluded that ICI from channels more than two positions away is insignificant.

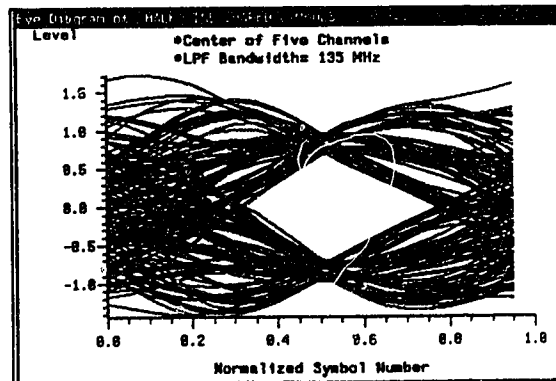


Figure 4.2- Eye Diagram for Half Sine Pulse Shapes, Centre of Five Channels

The output filter in the results above was assumed to be a 3rd order Butterworth with a BW= 135 MHz. The reason for using this particular filter will now be explained. A Butterworth filter was chosen because it was the only filter module available in the BOSS simulator which could operate on a real valued signal (i.e. not in the complex envelope representation). Demodulating the centre of five channels and starting with a 3rd order filter, the demodulator filter BW was varied from 100 to 200 MHz in 5 MHz increments. This resulted in a plot of the maximum eye opening (relative to BW= 100 MHz) versus BW. After iteration for 4th and 5th order filters, a family of curves given in Figure 4.3a was generated, where the eye openings are displayed relative to an eye for a 3rd order filter with BW= 100 MHz.

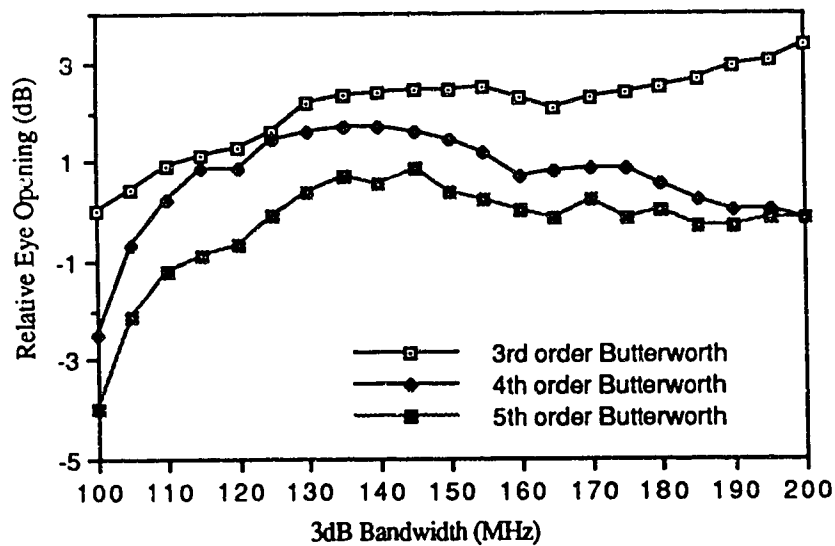


Figure 4.3a- Influence of ICI and ISI on Eye Opening vs. LPF BW for 3rd, 4th and 5th Order Butterworth Filters Relative to a 3rd Order Butterworth Filter, BW= 100 MHz

To evaluate which is the best choice from the sample space of different Butterworth filters given in Figure 4.3a, it is necessary to base the comparison on signal to noise ratio performance. Select any two filters indexed by points $i=1$ and $i=0$ from Figure 4.3a

Where: A_i = Maximum Eye value using filter i

$$f_{NEB\ i} = f_{3dB\ i} \cdot \zeta(n_i)$$

Now:

$$\zeta(n_i) = \frac{f_{NEB\ i}}{f_{3dB\ i}} = \int_0^{\infty} \frac{1}{1+\omega^{2n_i}} d\omega = \frac{\pi}{2n_i \cdot \sin\left(\frac{\pi}{2n_i}\right)} \quad (4.1)$$

n_i = order of Butterworth filter
 N = noise power spectral density input to filter (assumed constant)
 $f_{3dB\ i}$ = 3 dB bandwidth of filter i
 $f_{NEB\ i}$ = Noise equivalent bandwidth of filter i

The difference in signal to noise ratio (Δ SNR or SNR gain) between the two points of comparison $i=1$ and $i=0$ would be

$$\begin{aligned} \Delta\text{SNR} &= \text{SNR}_1 - \text{SNR}_0 \\ &= 10 \log\left(\frac{A_1^2}{N \cdot f_{NEB_1}}\right) - 10 \log\left(\frac{A_0^2}{N \cdot f_{NEB_0}}\right) \\ &= 20 \log\left(\frac{A_1}{A_0}\right) - 10 \log\left(\frac{f_{NEB_1}}{f_{NEB_0}}\right) \\ \Delta\text{SNR} &= 20 \log\left(\frac{A_1}{A_0}\right) - 10 \log\left(\frac{f_{3dB_1} \zeta(n_1)}{f_{3dB_0} \zeta(n_0)}\right) \end{aligned} \quad (4.2)$$

By arbitrarily choosing the point of reference for the SNR comparison to be a 3rd order filter with a $f_{3dB} = 100$ MHz, the Δ SNR or SNR gain of each filter relative to this point was calculated and is shown in Figure 4.3b. By inspecting this graph it is observed that the best SNR at the output of the receiver will be maintained with a 3rd order low pass filter having a BW= 135 MHz. From this analysis it was assumed that a 3rd order receiver filter would be used for the other baseband pulse shape configurations, and the optimum BW determined on the basis of simulation results.

In summary, it was found that when no quadrature subchannels were present and the half sine pulse shape was employed, orthogonality was maintained between directly adjacent channels as predicted by (3.22). Penalties of 2.7 dB due to ISI and 0.7 dB due to ICI from two non-orthogonal channels two positions away, and 0.1 dB from 45 nonadjacent channels were observed. The total penalty due to ISI, and ICI with 50

channels present is therefore 3.6 dB. The optimum Butterworth low pass filter was found to be a 3rd order one with a 3 dB bandwidth of 135 MHz.

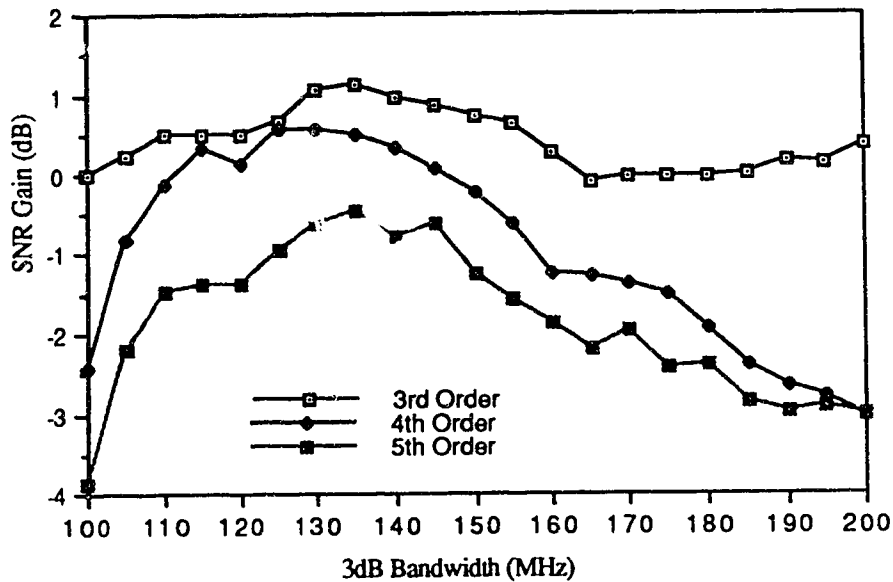


Figure 4.3b- SNR Performance of Half Sine Shape vs. BW of 3rd, 4th and 5th Order Butterworth Filters Relative to a 3rd Order Filter, BW= 100 MHz

4.1.1b. Rectangular Pulse Shape

The next baseband pulse considered was the rectangular shape as described in Section 3.2.2b. From results in Section 4.1.1a it was assumed that a 3rd order filter with BW= 135 MHz initially would be used in the receiver. A stand alone channel was generated and demodulated with the resulting eye diagram shown in Figure 4.4. Its maximum eye opening is 0.95 which translates to an eye closure penalty of 0.45 dB due to ISI. To verify orthogonality for rectangular shaped pulses between directly adjacent channels, the center of three channels was demodulated yielding the second eye shown in Figure 4.4. Its maximum opening was 0.94 which is very close to the value observed for the single stand alone channel. Therefore it is concluded that orthogonality between directly adjacent channels is maintained for rectangular shaped pulses with no quadrature subchannels present.

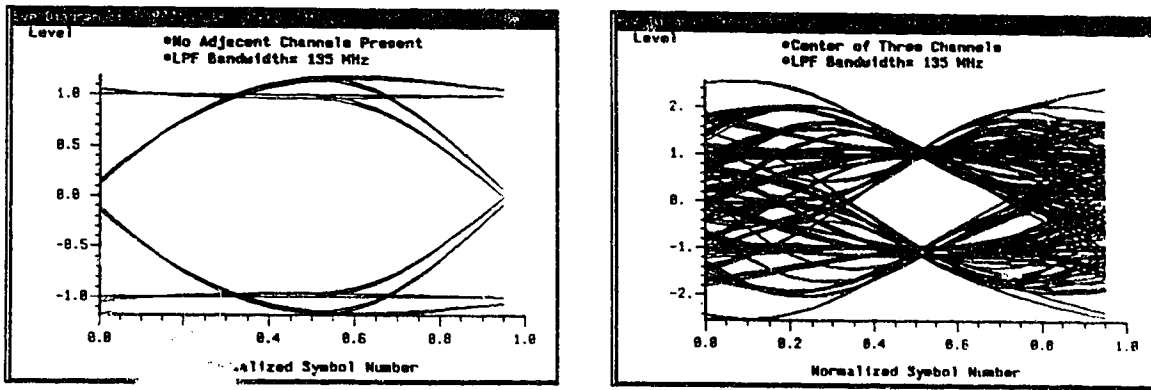


Fig. 4.4- Eye Diagrams for Rectangular Pulse Shape, Channel with No Adjacent Channels Present and a Centre of Three Channels

As with the half sine shaped pulses above, a five channel modified orthogonal SCM signal was generated and the centre channel demodulated to observe the ICI effects from two nonorthogonal channels. As from Figure 4.5 a maximum value of the eye of 0.84 was observed. Compared to the maximum value of the eye for the stand alone channel, the ICI that arises with two nonadjacent, nonorthogonal channels present is 1.1 dB. To observe the ICI arising from a large number of channels, channel 25 from 50 channels was demodulated and is shown in Figure 4.18c. A maximum eye opening of 0.75 was observed which corresponds to a 1 dB increase in ICI above that of the five channel case.

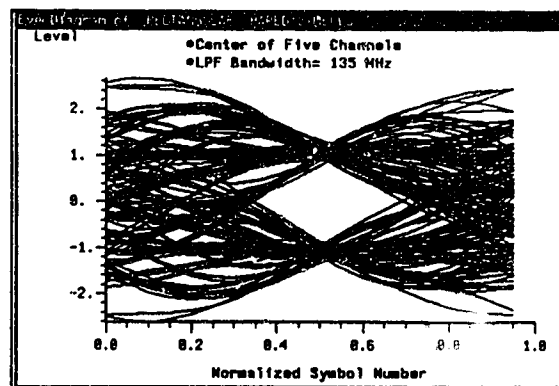


Figure 4.5- Eye Diagram for Rectangular Pulse Shapes, Centre of 5 Channels

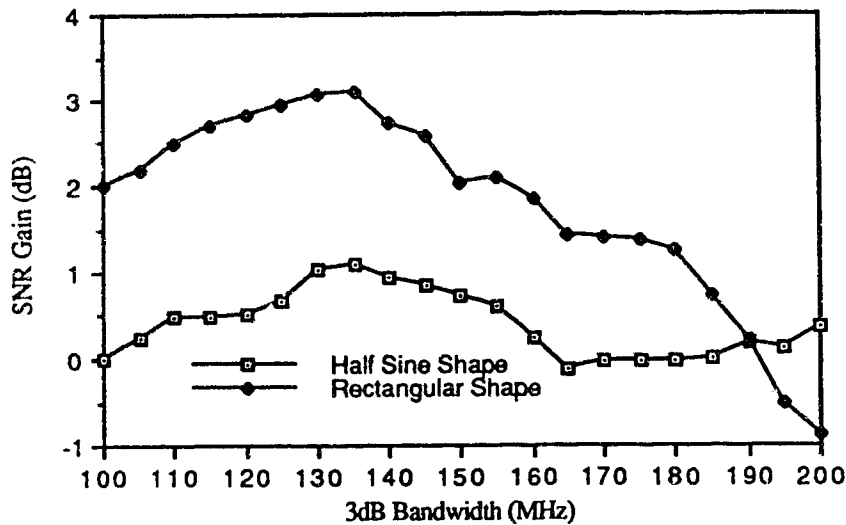


Figure 4.6- SNR Performance of Rectangular Shape Using a 3rd Order Filter vs. LPF Bandwidth, Relative to a 3rd Order Filter, Half Sine Shape with BW= 100 MHz, Centre of 5 Channels

To ensure that the best receiver filter BW was chosen, it was varied between 100 and 200 MHz and the SNR gain relative to BW= 100 MHz was evaluated assuming a 3rd order filter. By inspecting Figure 4.6 it was concluded that BW= 135 MHz was indeed the best choice.

In summary then it was found that for rectangular shaped baseband pulses (with no quadrature subchannels present) orthogonality was maintained between directly adjacent channels as predicted by (3.22). Penalties of 0.45 dB due to ISI and 1.1 dB due to ICI from two non-adjacent channels, and 1.0 dB from 45 nonadjacent channels were observed to be incurred. The total penalty due to ISI, and ICI with 50 channels present is therefore 2.5 dB. The optimum Butterworth low pass filter was found to be a 3rd order, one with a 3 dB bandwidth of 135 MHz.

For a performance comparison between half sine and rectangular shape (with no quadrature subchannels) consider the following discussion. In comparison to transmission with no signal degradation (ie with maximum normalized eye opening of 1.0) the half sine shape had a total signal degradation of 3.6 dB, while the rectangular shape had a degradation of 2.5 dB. Therefore the SNR performance of rectangular shaped pulses is

approximately 1.0 dB better. Examining the baseband signal spectra given in Sections 3.2.2a and 3.2.2b it was observed that the main spectral lobes between nonadjacent channels overlapped for the half sine shape and did not for the rectangular shape. The total ICI eye closure penalties of the half sine and rectangular shapes are 0.9 and 2.1 dB respectively. Therefore ICI from the higher interfering spectral tails of nonorthogonal channels employing the rectangular pulse shaped, is more severe than the main lobe spectral interference of the half sine pulse shape. This however is offset by an ISI penalty of 2.73 dB for half sine shaped symbols compared to only a 0.45 dB penalty for the rectangular shape, therefore the overall rectangular shaped pulse had 1 dB better performance.

4.1.1c. Sine Square Pulse Shape

The final baseband pulse to be considered as a candidate for modified orthogonal SCM, is the sine square shape described in Section 3.2.2c. With a receiver low pass filter BW= 135 MHz, the maximum eye openings were measured to be 0.62 and 0.61 for the single and three channel tests respectively; see Figure 4.7. Since these two eye openings are very close to the same value, it is concluded that directly adjacent channels are orthogonal for the sine square pulse shape. The ISI eye closure penalty is therefore 4.2 dB.

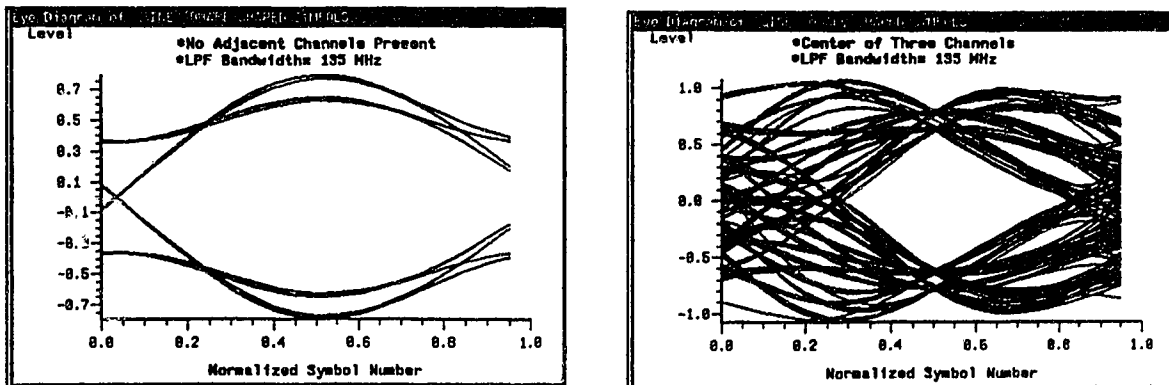


Figure 4.7- Eye Diagram of Sine Squared Pulses for Single and Three Channel Tests

To measure the level of ICI from two nonorthogonal channels, a five channel test was set up as with the previous symbol shapes using a 3rd order receiver filter with a BW= 135 MHz. The maximum value of the eye was observed to be 0.46 (see Figure 4.8), which corresponds to an ICI eye closure penalty of 2.6 dB. To verify that the 3rd order receiver filter was optimized for a maximum SNR, its bandwidth was varied between 100 and 200 MHz. By inspecting Figure 4.9 it may be concluded that a BW= 135 MHz is a reasonable choice since it provides the same SNR performance as any of the lesser bandwidths.

Compared to half sine pulse shape, the SNR performance of sine square pulses is 3.4 dB worse, by Figure 4.9. This arises as a result of both the ISI and ICI penalties being more severe: the ISI penalty has risen from 2.73 dB to 4.2 dB and the ICI from two nonorthogonal channels has increased from 0.7 dB to 2.6 dB. The substantial increase in ICI may be accounted for by noting that the first spectral null of sine square shaped symbols is 2B or 400 MHz (see Section 3.2.2c). Therefore compared to the half sine shape, whose first spectral null is at 300 MHz, the sine squared symbols should have more severe ICI from nonorthogonal channels, as was observed. Since the ICI & ISI penalties are 3.2 dB worse than the half sine shape, it is concluded that this shape is not suitable for implementation in the system outlined here, and therefore will not be considered as a candidate for the modified O-QAM system.

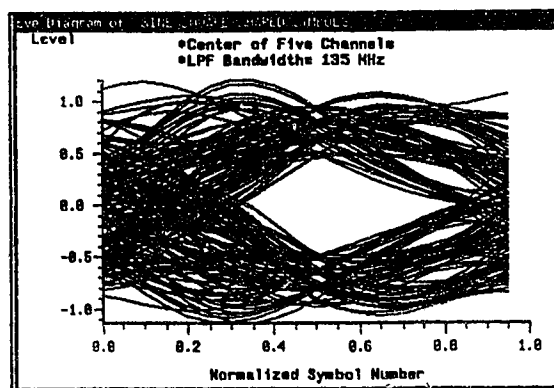


Figure 4.8- Eye Diagram for Sine Square Shaped Pulses, Centre of 5 Channels

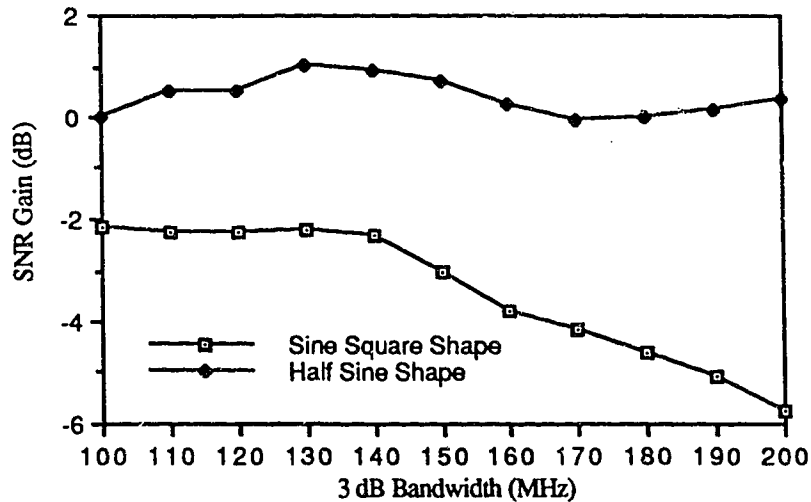


Figure 4.9- SNR Performance of Sine Square Shape vs. LPF Bandwidth, Relative to Half Sine Eye with 3rd Order 100 MHz Filter

4.1.1d. Butterworth Low Pass Filter Shaped Pulses

To verify the hypothesis of Section 3.2.2d that orthogonality between directly adjacent channels cannot be maintained by the baseband phase spectrum of Butterworth low pass filter shaped pulses not satisfying criterion (5) in Section 3.1.1, one and three channel tests were set up. The shaping low pass filter was assumed to be a 3rd order Butterworth and its 3dB bandwidth was arbitrarily chosen to take on values of 100 and 200 MHz. The receive filter was a 3rd order Butterworth as before with a bandwidth of 135 MHz. Figure 4.10 shows eye diagrams for shaping bandwidths of 100 MHz and 200 MHz for a single channel with no adjacent channels present, paralleled by the eye diagrams from the centre of three channels for the same shaping filter bandwidths. By inspecting this figure it is concluded that as expected, orthogonality is not maintained between directly adjacent channels. Therefore the Butterworth low pass filter shaping in the transmitter distorts the baseband pulse's phase spectrum in violation of criterion 5 in Section 3.1, and makes this configuration unacceptable for use in modified orthogonal multiplexing.

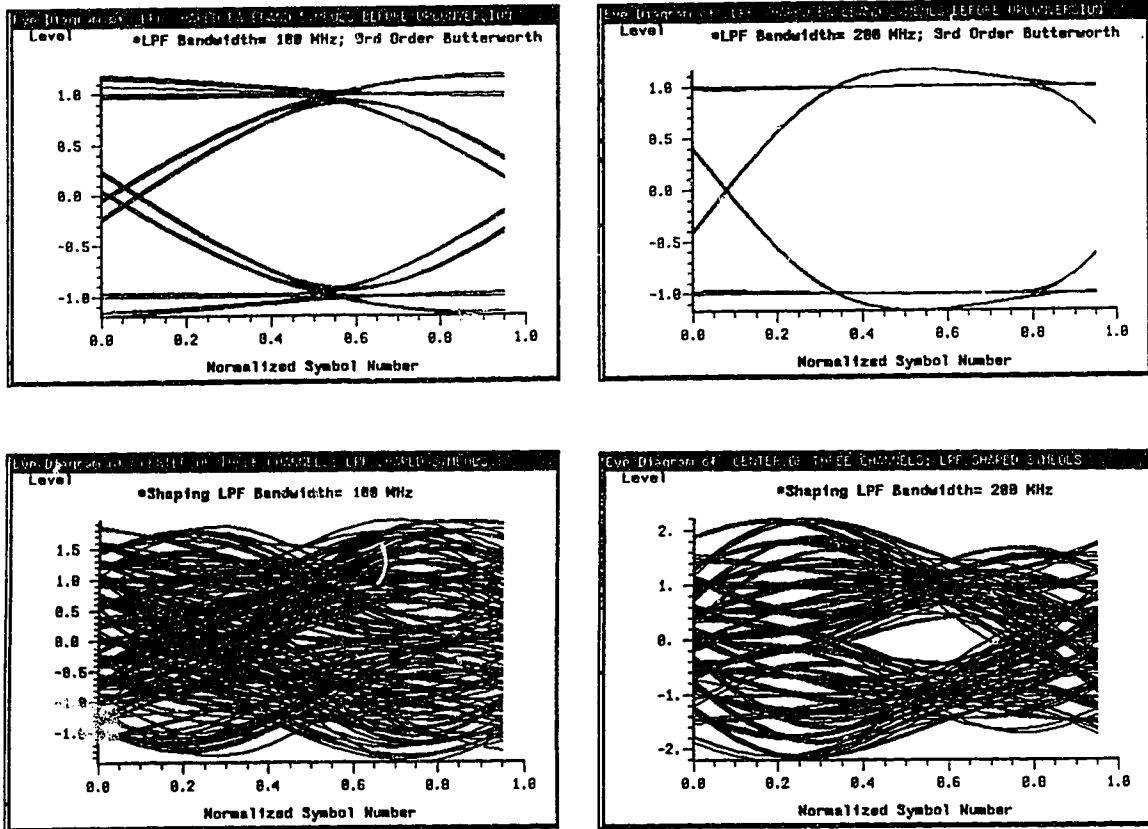


Figure 4.10: Comparison of Single and Three Channel Eyes for Two Low Pass Filter Shapes (BW= 100 MHz and 200 MHz)

4.1.2 Modified O-QAM

Next consider the performance of the modified O-QAM system as shown in Figure 3.4 with $H(\omega)=1$ and $F(\omega)$ not bandlimited. Based on the results in Section 4.1.1 it was concluded that only half sine and rectangular shaped pulses need to be considered in the modified O-QAM system because the sine square and Butterworth low pass filter shaped pulses introduce excessive ICI. The discussion in Section 3.3 explained that orthogonality between adjacent channels is not maintained for channels in the modified O-QAM system. Therefore to evaluate the level of ICI arising from all subchannels with in-phase carriers, simulations were conducted and the results are given here. The modulators and demodulator used in simulations are shown in Section 3.3.2. Note that a 3rd order Butterworth receiver filter with a bandwidth of 135 MHz was assumed for both cases.

4.1.2a. Half Sine Pulse Shape

Consider in this section the performance in an ideal transmission medium of the modified O-QAM system employing the half sine baseband pulse shape. The results shown in Figures 4.11a- 4.11c were obtained by demodulating the centre of single, three and five channel tests respectively for both the sine and cosine subchannels. Observing Figures 4.11a and 4.11b reveals that the maximum eye opening for the single and three channel cases are 0.73 and 0.60 respectively. This corresponds to an ISI penalty of 2.7 dB (which is the same as for the no quadrature subchannel case), and an ICI penalty of 1.7 dB. Therefore perfect orthogonality between adjacent channels is not maintained. This was predicted by the analysis in Section 3.2.1 and is discussed in Section 3.3.

By inspecting Figure 4.11c it is observed that the maximum eye opening is reduced to 0.52 as a result of ICI from two non-adjacent channels. This corresponds to an additional 1.2 dB penalty. The total ICI with five channels present is then 2.9 dB which is 2.2 dB higher than for the half sine shape with no quadrature subchannels as discussed in Section 4.1.1a. It was found that demodulating the 13th of a 25 channel modified O-QAM system resulted in an eye opening of 0.5, which means only a 0.3 dB increase in ICI compared to the five channel system; this was observed on the eye diagram in Figure 4.19c. Compared to the system described in Section 4.1.1a, this technique yields twice the bandwidth efficiency, but at the price of a total increase in ICI of 2.3 dB. Doubling the bandwidth efficiency cuts the number of channels in half and hence twice the signal power is available to each channel in the optical link. Therefore to quantify this trade off between higher bandwidth efficiency and increased ICI, simulations on the optical SCM link had to be conducted to compare this implementation with the other possibilities.

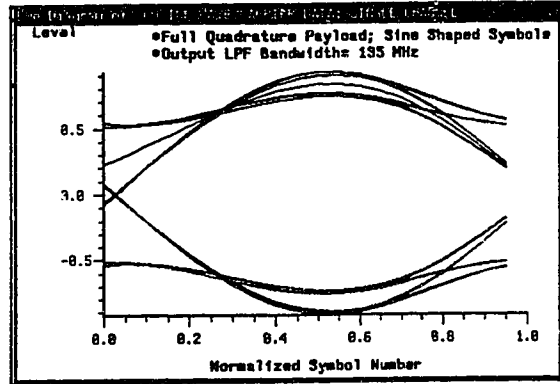
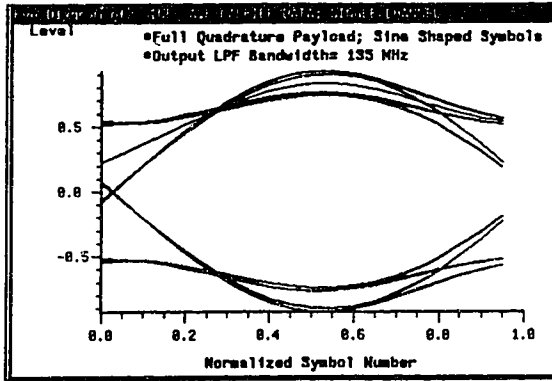


Figure 4.11a- Eye Diagrams for Sine and Cosine Carriers, Half Sine Pulse Shape -Full Quadrature Signal Single Channel

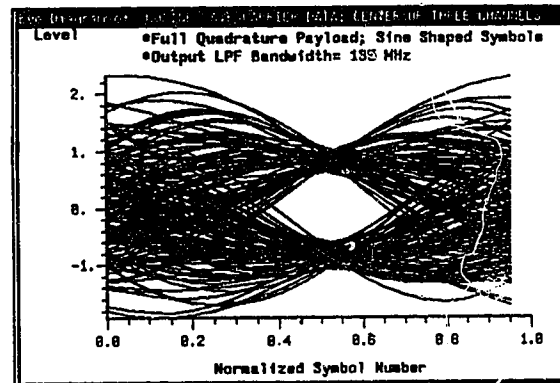
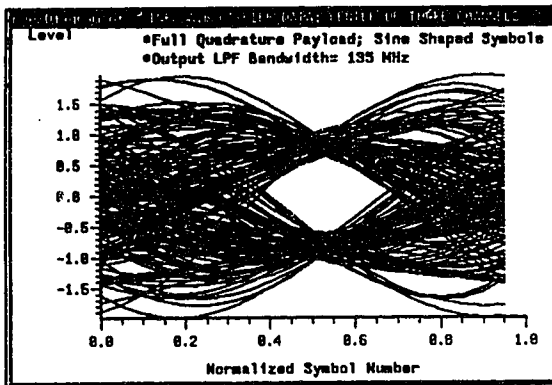


Figure 4.11b- Eye Diagrams for Sine and Cosine Carriers, Half Sine Pulse Shape -Full Quadrature Signal, Centre of Three Channels

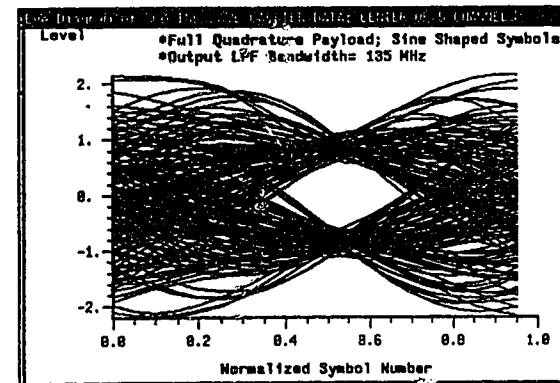
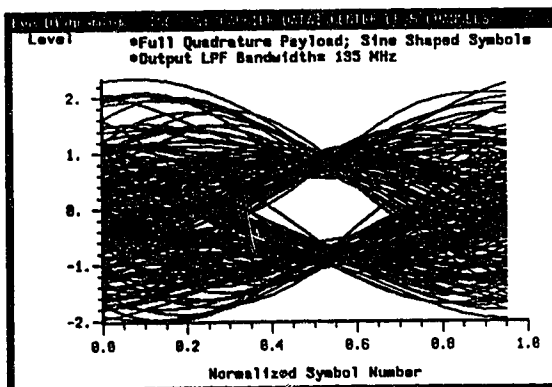


Figure 4.11c- Eye Diagrams for Sine and Cosine Carriers, Half Sine Pulse Shape -Full Quadrature Signal, Centre of Five Channels

4.1.2b. Rectangular Pulse Shape

Consider in this section the performance in an ideal transmission medium of the modified O-QAM system using the rectangular baseband pulse shape. The results from demodulating the centre of single, three and five channel tests are shown in Figures 4.12a, 4.12b and 4.12c respectively for both the sine and cosine subchannels. Comparing Figures 4.12a and 4.12b it may be concluded that orthogonality between directly adjacent channels is not maintained, as was found with the half sine shape, but the eye closure due to ICI is significantly more severe. Considering Figure 4.12c it is observed that complete eye closure due to ICI results, therefore this implementation is not suitable to be a candidate for simulation on the optical link.

This behavior may be explained intuitively as follows. Consider as a mind experiment the condition that there are two channels present with their carriers spaced at B Hz, and both carriers are in phase, ie $\sin(\omega_0 t)$ and $\sin(\omega_0 + 2\pi B)t$. Also let the pulse shape be half sine. Define the centre of pulses in the channel 1 (lower position) to be at $t_n = nT$, and the centre of pulses in channel 2 be at $t_n' = (n+0.5)T$. The signal for each channel is suppressed carrier amplitude modulated, so in time the signal for channel 2 returns to zero at time instants of $t_{\text{zero-2}} = nT$. After downconverting the composite signal (of channels 1 and 2) by multiplication with $\sin(\omega_0 t)$, the downconverted signal from channel 2 must still return to zero at instants of $t_{\text{zero-2}} = nT$. This is the sampling instant for the symbol in channel 1, and therefore doesn't see channel 2. Introduction of non-Nyquist filtering will cause the return to zero instant to shift because of ISI, and some eye closure penalty will result. Therefore the pulses are still separable, even though their channels are not orthogonal. Now in a similar mind experiment replace the half sine shape with a rectangular shaped pulse. This pulse may not return to zero at the end of every symbol. Then by the same argument as above, channel 1 after downconversion will see interference from channel 2, before filtering. Therefore more ICI will arise with the rectangular shape.

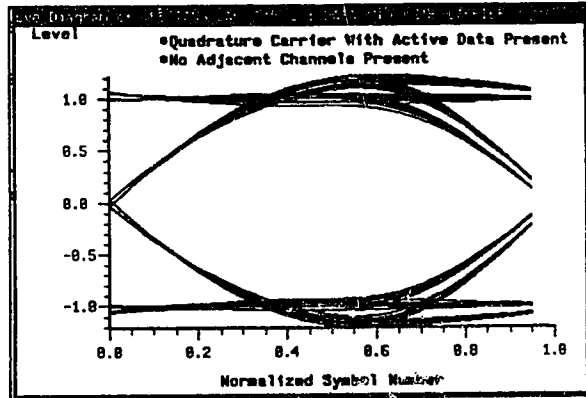
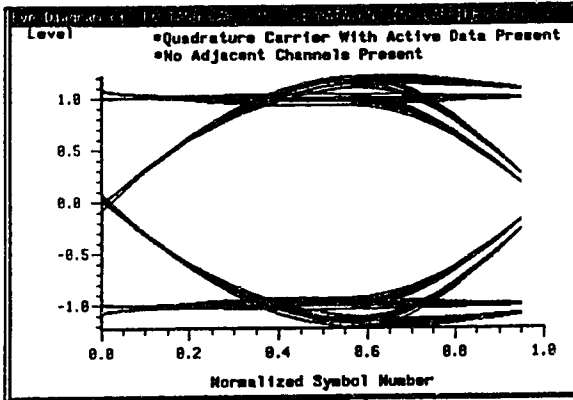


Figure 4.12a- Eye Diagrams for Sine and Cosine Carriers, Rectangular Shaped Pulses- Full Quadrature Signal, Single Channel

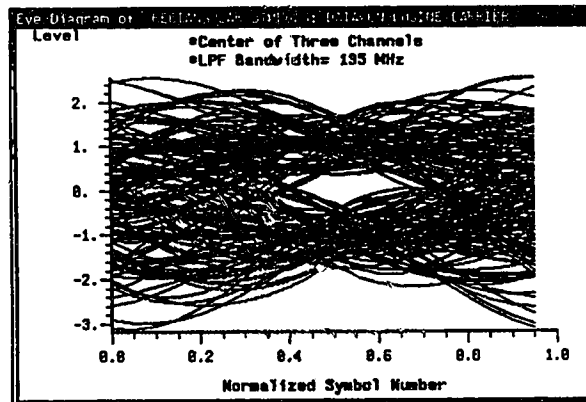
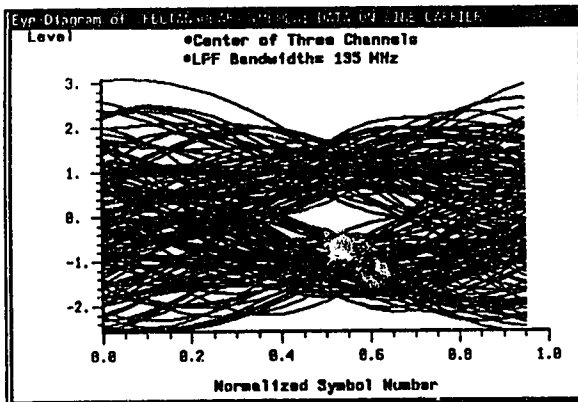


Figure 4.12b- Eye Diagrams for Sine and Cosine Carriers, Rectangular Shaped Pulses- Full Quadrature Signal, Centre of 3 Channels

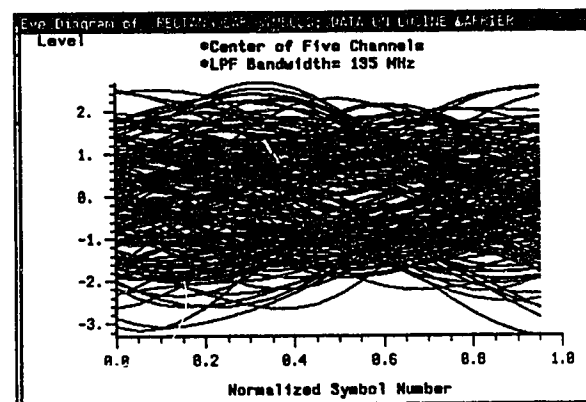
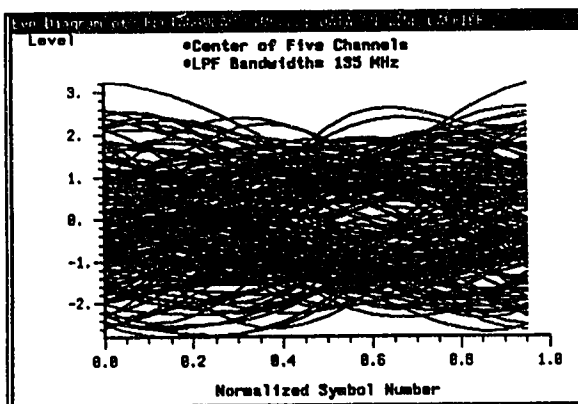


Figure 4.12c- Eye Diagrams for Sine and Cosine Carriers, Rectangular Shaped Pulses- Full Quadrature Signal- Centre of 5 Channels

4.1.3. Performance Summary of Proposed Modified Orthogonal SCM Schemes in an Ideal Transmission Medium

For a performance comparison of all the proposed baseband pulse shapes, the ICI and ISI characteristics were observed by an eye diagram analysis. Assuming a Butterworth low pass filter in the receiver, optimized SNR performance was achieved. This was done by trading off noise equivalent bandwidth, ISI and ICI for half sine, rectangular and sine square shaped pulses to arrive at an optimum 3rd order filter with a 3dB bandwidth of 135 MHz. As predicted in Section 3.2.2d, Butterworth low pass filter shaped pulses were eliminated as a candidate for modified orthogonal SCM because orthogonality between adjacent channels was not maintained. Figure 4.13 summarizes the ISI and ICI penalties incurred for the different modified orthogonal SCM schemes.

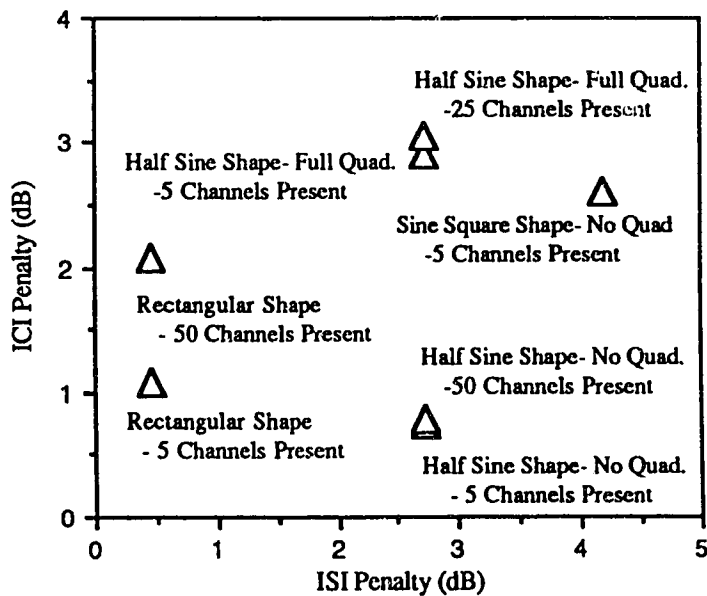


Figure 4.13- ICI and ISI Penalties for Proposed Pulse Shapes of Modified Orthogonal SCM Using Butterworth LPF in the Receiver

From Figure 4.13 it is concluded that the pulse shape which has the least total ISI and ICI penalty is the rectangular one. Note that the ICI penalty for the rectangular pulse shape is larger than for the half sine shape. This may be attributed to spectral tails which roll off proportionally to $1/f$ with the rectangular shape vs. $1/f^2$ for half sine. It may then

be concluded that rectangular shaped pulses are better suited to filtering at the receiver by a Butterworth low pass filter than are half sine shaped ones.

The total eye closure penalties for each configuration carrying 50 active data streams are then

Table 4.1: Summary of Total Eye Closure Penalty and Bandwidth Efficiency

Implementation Type	Total Eye Penalty	Bandwidth Efficiency
Rectangular-No Quad	2.5 dB	1 bit/s/Hz
Half Sine-No Quad	3.5 dB	1
Half Sine-Full Quad	5.9 dB	2
Sine Square-No Quad	6.7 dB	1

Considering only the eye closure penalties of each configuration in Table 4.1 it is concluded that the sine square shape with no quadrature subchannels present is the only implementation which may be eliminated from simulations through the optical link.

4.1.4 Eye Closure Penalties Caused by Phase Errors

O-QAM provides an efficient means to achieve near Nyquist signalling rate with double sideband channels, but is very sensitive to phase errors in both the transmit carrier and receive local oscillator. Saltzberg found that the O-QAM signal was three times more sensitive to receiver phase errors than conventional FDM signals [41]. The modified orthogonal SCM transmission schemes of interest must also then be sensitive to carrier and local oscillator phase errors.

To characterize sensitivity to transmitter carrier phase errors in a five channel test, the centre carrier's phase was varied and eye diagrams were generated from the demodulated centre channel. For this test, the phase of the receiver local oscillator tracked any transmitter phase errors. Results from the series of simulations where the carrier phase error is varied from 0° to 180° are shown in Figure 4.14a; note that for practical purposes, an eye closure penalty of 30 dB corresponds to complete eye closure.

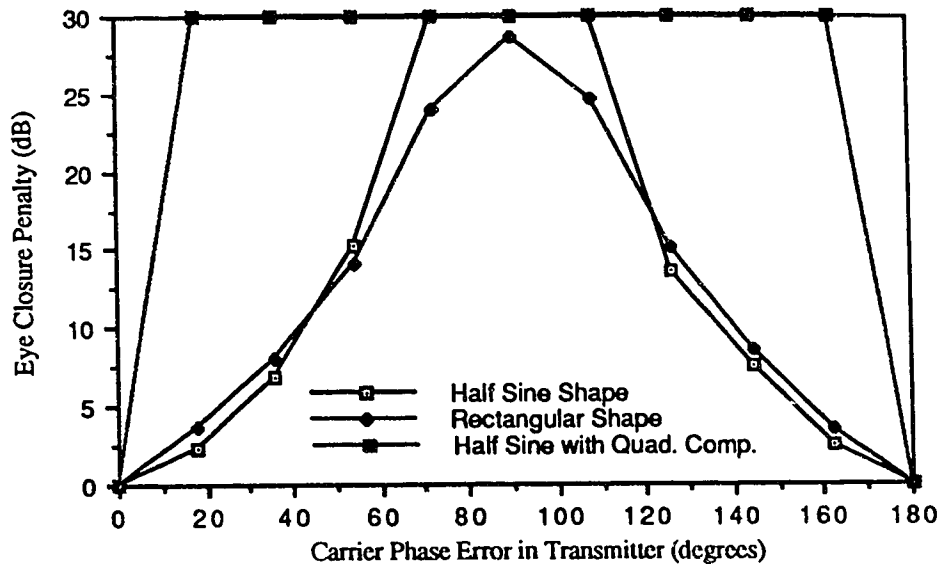


Figure 4.14a- Eye Closure Penalty vs. Large Transmitter Carrier Phase Errors, The Centre of 5 Channels was Demodulated

From Figure 4.14a it is observed that as the phase error approaches 90° , orthogonality between previously orthogonal channels or subchannels is lost. These results show that the signal employing half-sine shaped pulses with no quadrature component is most immune to carrier phase errors less than 45° . However with phase errors greater than 45° , the signal using the rectangular pulse shape performs better. It may also be concluded from Figure 4.14a that the modified O-QAM system is very much more sensitive to carrier phase errors than to the other configurations. Shown in Figure 4.14b are the eye closure penalties for small transmitter carrier phase errors. It is concluded from Figure 4.14b that for carrier phase errors below 36° , the same trends exist as were observed in Figure 4.14a.

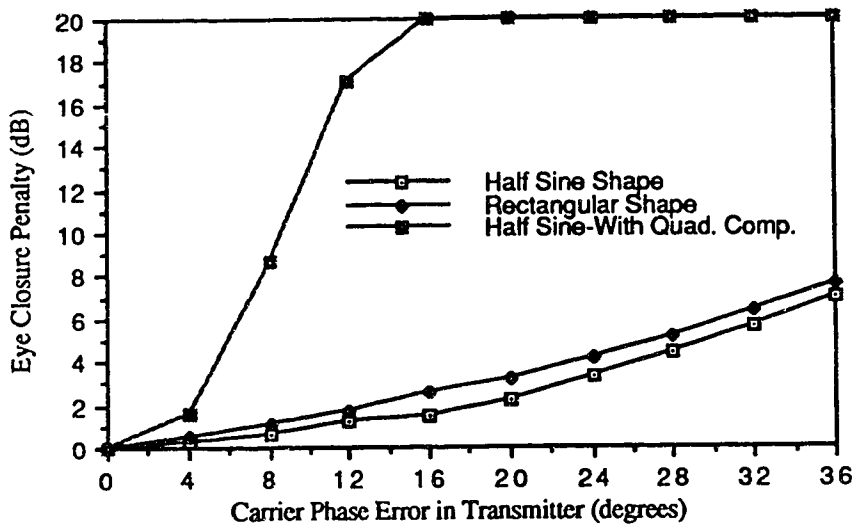


Figure 4.14b- Eye Closure Penalty vs. Small Transmitter Carrier Phase Errors, The Centre of Five Channels was Demodulated

The second system location at which there may be signal degradations due to phase errors is the receiver. If the local oscillator (LO) has some static phase error, the output pulses will experience distortion. To characterize this degradation, a similar test as above was run except the phase error of the downconversion local oscillator was varied in 4° increments from 0° to 36°, and the phase error in the transmitter carrier was set to zero. The results for the three signal configurations are given in Figure 4.14c.

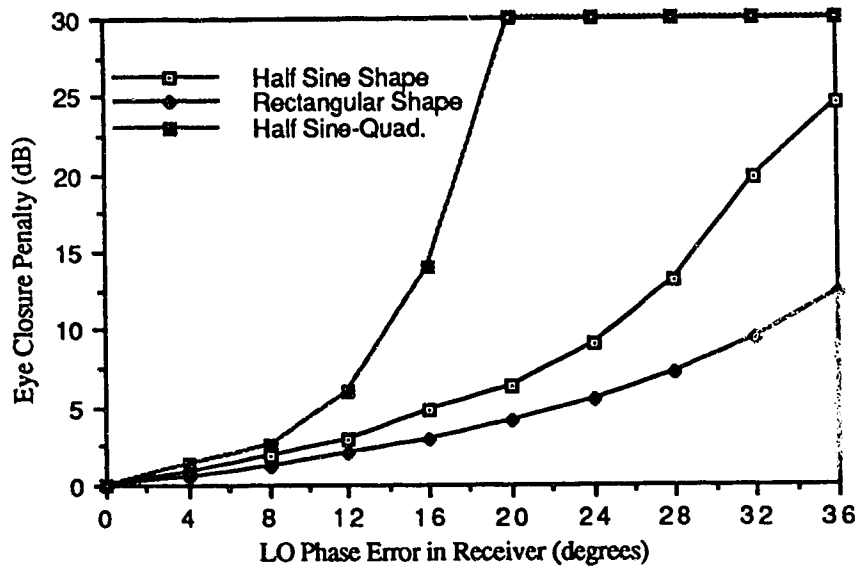


Figure 4.14c- Eye Closure Penalty vs. Receiver Local Oscillator Phase Errors, The Centre of Five Channels was Demodulated

By inspection of Figure 4.14c it is observed that the eye closure penalty versus receiver LO phase error is least severe for rectangular shaped pulses, followed by half sine shaped pulses; it is most severe for half sine shaped pulses in the modified O-QAM system.

Comparing Figures 4.14b and 4.14c it is observed that the penalties for receiver local oscillator phase errors are more severe than those observed for transmitter carrier phase errors. This may be explained as follows. In the case where the phases of all carriers are correct and there is no downconversion phase error for the channel of interest, a certain level of ICI arises due to nonorthogonal channels. As a thought experiment, remove the channel of interest and apply downconversion and filtering as if the channel of interest was still there. There will be an appearance of the same interference power as if the channel of interest were present. Now if the phase of the downconversion local oscillator is in error, the level of ICI appearing will increase. This is because the phase spectra of orthogonal channels after downconversion will no longer be completely orthogonal to the channel of interest. By the principle of superposition, place the channel of interest back into its position and apply the same downconversion phase error. This will result in additional symbol degradation because downconversion of the channel of interest is also incorrect. Therefore there are two sources of signal degradation due to downconversion phase errors: first in not maintaining orthogonality at the adjacent channels and the second arising from demodulation phase error of the channel itself.

In the case where there is a transmitter carrier phase error which is tracked by the demodulating local oscillator, signal degradation will arise only from reduction of orthogonality, as in the above thought experiment. Therefore penalties will be less severe in this case than if a receiver local oscillator phase error occurred.

To evaluate which signal configuration is least sensitive to phase errors, the combined signal degradation caused by the carrier and local oscillator must be considered. By inspecting Figures 4.14b it is observed that for all phase errors plotted, the rectangular shape introduces approximately 1 dB more than the half sine shape; whereas in Figure

4.14c the rectangular shape was more than 1 dB below the half sine shape for errors greater than 10°. Since it is more difficult to manage phase errors at the receiver due to the issue of carrier recovery, using the rectangular pulse shape would be the best choice in terms of phase error immunity. In summary it is concluded that the signal employing rectangular shaped pulses is least sensitive to static phase errors in this system, and that these errors may be managed in a real system by including the corresponding penalty (given in Figures 4.14b and 4.14c) in the link budget.

4.1.5 Signal Statistics of Fifty Multiplexed Active Data Streams

The carrier plan in this system given by (2.30) in combination with the coherent phase relationship presents an area of concern, because the addition of all carriers is deterministic. Modulating each carrier with an independent random bit stream alters this deterministic addition, but the data is also synchronous. The statistics of this modified orthogonal SCM signal are therefore unknown. To examine this issue, the signal statistics of each configuration were observed by simulating a composite broadband signal of fifty active and independent random data streams (@ 200 Mb/s) multiplexed together as demonstrated in Figure 3.4 (where $F(\omega)$ is not bandlimited). The multiplexed signal simulated is described analytically by (4.3a) for the case with no quadrature subchannels being present, and (4.3b) for the modified O-QAM implementation.

$$s(t_n) = \sum_{m \text{ odd}} \sum_{k=0}^{200} a_{km} f(t_n - kT) \sin[(\omega_o + m(2\pi B))t_n] + \sum_{m \text{ even}} \sum_{k=0}^{200} b_{km} f(t_n - kT) [\cos(\omega_o + m(2\pi B))t_n] \\ \text{(for } 1 \leq m \leq 50 \text{) and (for } 0 \leq k \leq 200 \text{)} \quad (4.3a)$$

$$s(t_n) = \sum_{m \text{ odd}} \sum_{k=0}^{200} a_{km} f(t - kT) \sin(\omega_o + m(2\pi B))t_n + \sum_{m \text{ even}} \sum_{k=0}^{200} b_{km} f(t - kT) \cos(\omega_o + m(2\pi B))t_n + \\ \sum_{m \text{ even}} \sum_{k=0}^{200} a_{km} f\left(t - kT - \frac{T}{2}\right) \sin(\omega_o + m(2\pi B))t_n + \sum_{m \text{ odd}} \sum_{k=0}^{200} b_{km} f\left(t - kT - \frac{T}{2}\right) \cos(\omega_o + m(2\pi B))t_n \\ \text{(for } 1 \leq m \leq 25 \text{) and (for } 0 \leq k \leq 200 \text{)} \quad (4.3b)$$

Where: $\omega_0 = 2\pi(400 \text{ MHz})$

$$B = 200 \text{ MHz} = 1/T$$

a_{nm} and b_{nm} = binary symbols which take on values of either +1 or -1

$t_n = n\Delta T = n(6.25 \text{ pSec})$ = discrete time instants used in simulations,
 $f(t)$ = baseband pulse shape employed; (descriptions given in Section 3.2.2)

The multiplexed signal was simulated and a probability distribution function of the signal values $s(t_n)$ was determined using the post processor in BOSS. Since the symbols were assigned a unit amplitude, the multiplexing of all channels resulted in a random variable $s(t_n)$, normalized to the maximum amplitude of one pulse. Therefore if all the multiplexed data streams add in time on a peak basis, the maximum value of the random variable (defined as $s(t_n)_{\text{peak}}$) will be fifty for the non-quadrature system and twenty five for the modified O-QAM implementation.

The other extreme is the condition that the channels are completely uncorrelated in which case they may be added on a power or rms basis. The rms value of the random variable will then be;

$$s(t_0)_{\text{Uncorrelated, rms}} = \sqrt{N} \rightarrow \text{where } N = \text{number of channels} \quad (4.3c)$$

If the signal's statistics were Gaussian then the pdf would be:

$$g(x) = \frac{1}{\sigma\sqrt{2\pi}} \exp\left(-\frac{x^2}{2\sigma^2}\right) \quad \text{for } -\infty \leq x \leq \infty \quad (4.3d)$$

where σ is the standard deviation, which is physically equivalent to the rms value.

Therefore:

$$\sigma = \sqrt{N} \quad (4.3e)$$

To compare the simulated signal statistics with the Gaussian distribution, examine Figures 4.15a - 4.15c for each of the three configurations selected in Section 4.1.3. In each case the simulated pdf is overlaid with the corresponding Gaussian pdf calculated using (4.3d) and

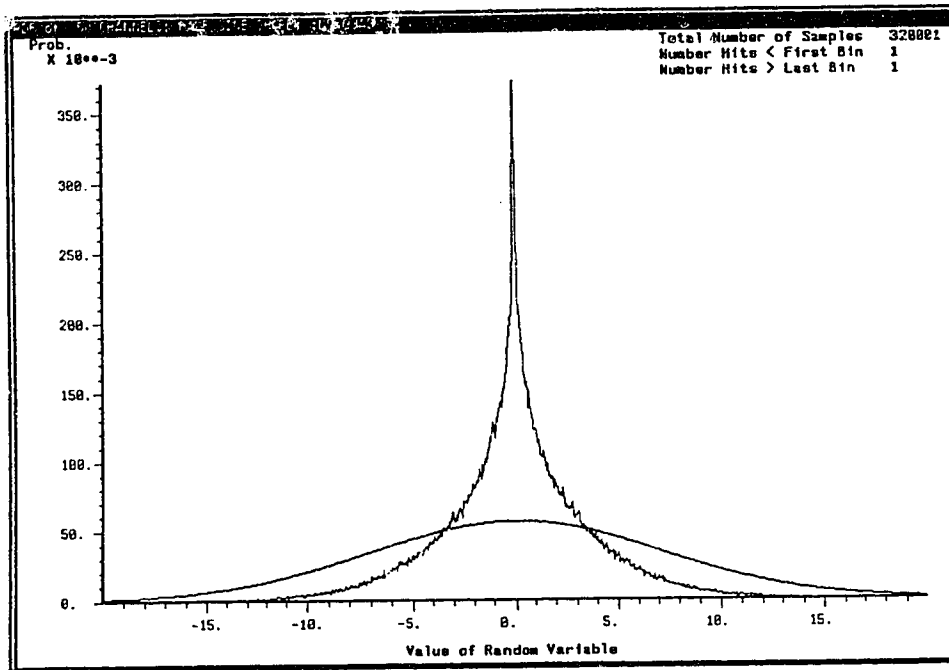


Figure 4.15a- Simulated PDF of 50 Channel Modified Orthogonal SCM Signal Employing the Half Sine Shape with No Quadrature Subchannels Present, Overlaid with the Corresponding Gaussian Distribution

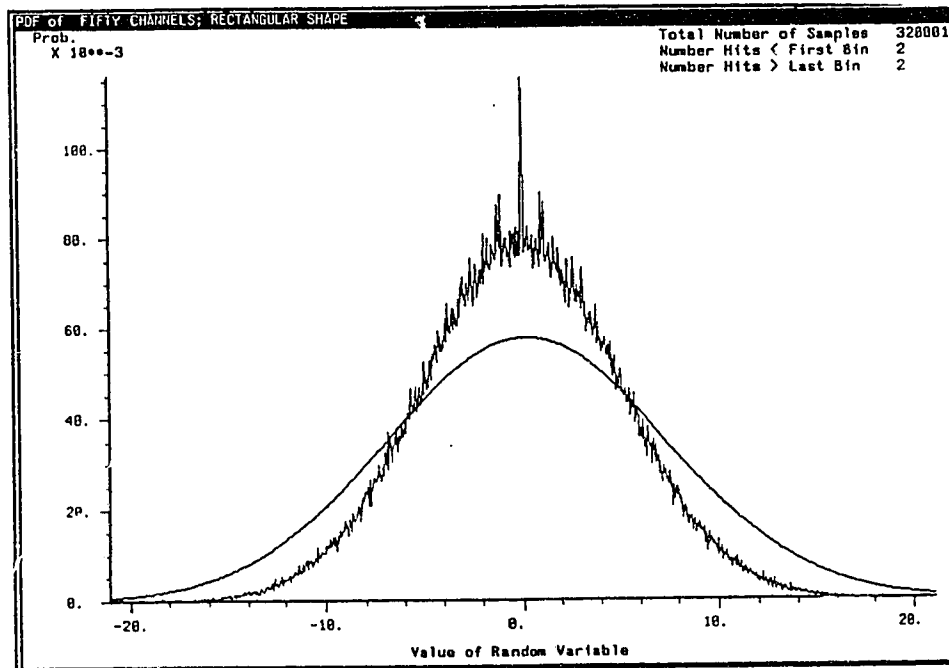


Figure 4.15b- Simulated PDF of 50 Channel Modified Orthogonal SCM Signal Employing the Rectangular Shape with No Quadrature Subchannels Present, Overlaid with the Corresponding Gaussian Distribution

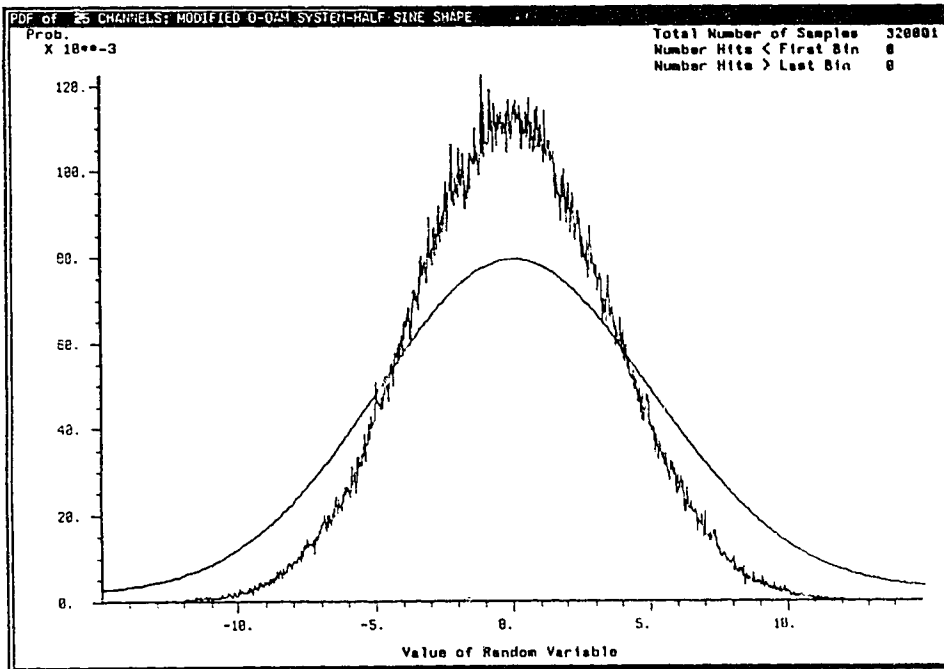


Figure 4.15c- Simulated PDF of 25 Channel Modified Orthogonal SCM Signal Employing the Half Sine Shape with Quadrature Subchannels Present, Overlaid with the Corresponding Gaussian Distribution

From Figures 4.15a - 4.15c the rms and peak values for $s(t_n)$ of each configuration were determined and are given in Table 4.2: note that the exact rms values of $s(t_n)$ are not known because they were calculated graphically. The following are also tabulated: the rms value σ of the corresponding Gaussian distribution; a peaking factor Ψ of each modified orthogonal SCM signal which is defined as:

$$\Psi \equiv \frac{s(t_n)_{\text{peak}}}{s(t_n)_{\text{rms}}} \quad (4.3f)$$

Also given is a factor χ , which compares the rms value of each modified orthogonal signal with its corresponding Gaussian equivalent. It is defined as

$$\chi \equiv \frac{s(t_n)_{\text{rms}}}{\sigma} \quad (4.3g)$$

Table 4.2- Statistical Characteristics of Modified Orthogonally Multiplexed Signals

Implementation Type	N	$\sigma = \sqrt{N}$	$s(t_n)_{\text{rms}}$	$s(t_n)_{\text{peak}}$	$\Psi \equiv \frac{\text{peak}}{\text{rms}}$	χ
Half Sine-No Quad	50	7.1	$5.1 \pm 7\%$	20	$3.9 \pm 7\%$	$0.72 \pm 7\%$
Rectangular-No Quad	50	7.1	$4.9 \pm 5\%$	21	$4.3 \pm 5\%$	$0.69 \pm 5\%$
Half Sine-Full Quad	25	5.0	$3.5 \pm 5\%$	15	$4.3 \pm 5\%$	$0.70 \pm 5\%$

Observing Figures 4.15a - 4.15c it is observed that the signal statistics of $s(t_n)$ are better than Gaussian. Also by noting the χ factor in Table 4.2, it is concluded that the rms value of $s(t_n)$ is approximately 0.7 times the rms value of $s(t_n)$ calculated if they were added on a power basis. This may be explained by considering that the line signal $s(t_n)$ is made up of frequency and phase related carriers, each modulated by an independent random bit stream. The channels therefore do not add on a power basis because they are correlated. This is important in our system because it means that the rms optical modulation depth (OMD_{rms}) of the linearly modulated laser is approximately 0.7 times the MOD. MOD was arbitrarily defined for simulation purposes as being the equivalent rms modulation depth calculated from addition of the channels signal current amplitude on a power basis. See Section 4.2.1 for further details.

The lower rms value of the modified orthogonal SCM signal was observed to have a peaking factor Ψ of approximately 4. The line signal $s(t_n)$ consisted of 320,000 simulation samples with the time interval between samples being 6.25 psec. This high sampling rate (160 GHz) was required because a 10 GHz composite broadband signal was simulated and it was suggested for simulations in BOSS to have a sampling rate of at least 15 times higher than the maximum signal frequency [54]. The tributary symbol rate was set at 200 Mbit/s which resulted in 800 samples per symbol. In generating the pdf of each line signal it was observed that the peak value of $s(t_n)$ occurred only once in 320,000 points. Therefore the peak "hit" occurred only for one 6.25 psec sample, which corresponds to $1/800^{\text{th}}$ the period of one symbol. Passing the line signal $s(t_n)$ through a nonlinear device creates opportunity for hits causing pulse distortion. However for this distortion to be relevant it must occur near the centre of a modulating pulse, which is a rare event.

The peaking characteristic which may cause distortion was accounted for in payload capacity simulations by passing the scaled broadband composite signal ($s(t)$) through the laser distortion model. Time domain effects of this distortion were observed by

demodulating a sample set of channels which experienced the most distortion, and performing an eye diagram analysis on each one. The effects of peaking were accounted for, but only over a time frame of 500 symbols. Simulation runs of 500 symbols in length resulted in 400,000 points in one simulation which caused this approach to be computationally complex. The high simulation sampling rate (160 GHz) was necessary because the laser model became inaccurate if a lower sampling rate was used, and because a 10 GHz wide broadband signal had to be simulated with no aliasing. See Section 4.2.1 for further details.

The final concern with the time domain behaviour of this signal is what happens when the carriers all add coherently when the data symbols in all subchannels simultaneously have the same value. To address this issue, the probability of having a logical one was set to 1.0 for simulating the modified O-QAM signal described by (4.3b). A time domain plot was obtained and is shown in Figure 4.15d. From this figure it is observed that a spike 200 psec wide in time, appears once every half baud period with alternating polarity. Its peak value was 16.5, only 1.1 times the peak value observed above. It was also observed that when one of the quadrature components was removed the spike occurred once every baud period with the same amplitude and polarity. A similar result was obtained for the signal employing rectangular shaped pulses as demonstrated in Figure 4.15e, except a peak signal of 30.5 was observed. Therefore the peak with all ones present was approximately 1.5 times greater than the maximum peak of 20 which occurred with random data.

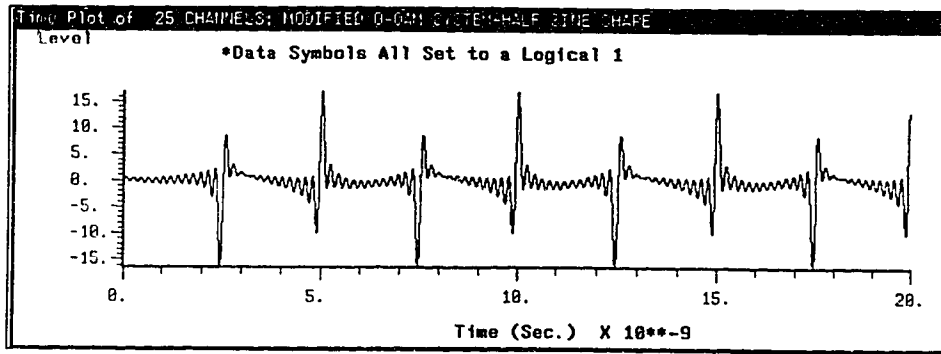


Figure 4.15d: Time Plot of $s(t)$ with All Data Symbols Set to a Logical One for Half Sine Shape with Quadrature Subchannels Present

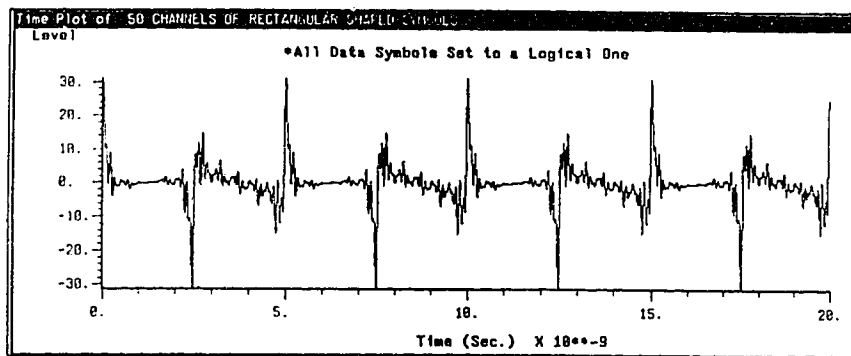


Figure 4.15e: Time Plot of $s(t)$ with All Data Symbols Set to a Logical One for Rectangular Shaped Symbol

In summary, statistics of the modified orthogonal SCM signal in three different configurations have been characterized and are nonGaussian. It has been determined that the composite signal has an rms level which is 0.7 times the level expected if channels added on a power basis, which suggests that less than independent addition occurs. A peaking factor of 4.0 was observed, which is less than for a Gaussian distributed signal. Also observed was that the signal becomes deterministic when the data symbols all acquire the same value, and that it appears as a train of spikes. The above statistical characteristics will influence the amplitude of distortion products appearing throughout the composite signal when passed through a nonlinear device. These distortion effects may be accounted for by passing this composite broadband signal through a simulation model of the distorting device.

4.2 SIMULATION AND RESULTS OF MODIFIED ORTHOGONAL SCM SIGNALS TRANSMITTED THROUGH THE LIGHTWAVE LINK

Now that the performance and characteristics for each of the modified orthogonal SCM signal configurations have been examined in an ideal transmission medium, consider what payload capacity may be achieved through the optical link using this technique. To accomplish this, a worst case eye diagram analysis was conducted by passing an active composite broadband signal of 5 to 10 Gbit/s through the large signal laser model and observing the time domain effects of distortion introduced (inclusive of ICI and ISI characterized above). The eye values were referenced to the worst case system noise level. Using the maximum value of the eye and the system noise, a BER calculation was performed and system margin estimated for each payload size assuming a BER $< 10^{-12}$. Effects due to nonideal system components such as amplifiers, mixers power combiner, etc were not included in this analysis but may be considered by subtracting the appropriate penalty to the system margin.

How these simulation experiments were conducted is described in Section 4.2.1. In Section 4.2.1a the method that the modulation or "MOD" level of the laser was maximized by simulation is presented. The MOD was arbitrarily defined for simulation purposes as being the equivalent rms modulation depth calculated from the addition of channels on a power basis. Section 4.2.1b presents the method used for calculating BER performance and system margin. Finally in Section 4.2.2 the payload size vs. system margin results are presented for each configuration and observations are discussed.

4.2.1 Simulation Experiments of the Digital SCM System

Described in this section is how the simulation experiments were conducted to estimate transmission capacity for the digital SCM link employing the different implementations of modified orthogonal SCM. The transmission capacity is a function of the available signal power, which is determined by the modulation depth of the laser, the received photocurrent, and the system noise. The received photocurrent and system noise for this particular link were straight forward to calculate (see Sections 2.2 and 2.3) and are used in the BER calculations explained in Section 4.2.1b. The more difficult variable to work with in this analysis is the modulation depth of the laser. It was shown in Section 4.1.5 that the individual channel currents do not add on a power basis because they are correlated. Therefore the modulation depth cannot be chosen simply on the basis of analytically summing together predicted distortion product levels to arrive at an acceptable signal to distortion ratio.

To account for distortion introduced onto the modified orthogonal SCM signal, a composite broadband signal carrying between 5 and 10 Gbit/s of data was generated by simulations, scaled to an optimum modulation depth determined by iteration, and passed through the large signal laser model. Due to the enormous bandwidth being simulated (ie 10 GHz) a sampling rate of 160 GHz was required which resulted in 800 samples per data symbol, at a parallel tributary rate of 200 Mbit/s per channel. This approach required 400,000 sample points per 500 symbol simulation run, therefore a Monte Carlo simulation approach was deemed unfeasible. Alternatively an eye diagram analysis was performed on demodulated channels experiencing the worst case distortion introduced by the laser, and the maximum eye values referenced to the system noise to permit a BER calculation to find system margin.

For simulation purposes the modulation depth was determined in terms of the arbitrary parameter MOD. MOD was defined to be the equivalent rms modulation depth

calculated from the addition on a power basis of the individual channel current amplitudes (which were assumed to be equal).

$$\text{MOD} \equiv \left(\frac{\sqrt{\sum_{n=1}^N i_n^2}}{(I_{\text{bias}} - I_{\text{thres}})} \right) = \frac{\sqrt{N} \cdot i_{\text{Chann, Tx}}}{(I_{\text{bias}} - I_{\text{thres}})} \quad (4.4)$$

where: i_n = amplitude of the channel current for channel $n = i_{\text{Chann, Tx}}$
 I_{bias} = bias current of laser model = 105 mA corresponding to f_{relax} of 10 GHz
 I_{thres} = threshold current of laser model = 15 mA
 N = the number of subcarrier channels

As shown in Section 4.1.5, channels in the modified orthogonal SCM signal add such that its rms equivalent is 0.7 times the rms level calculated if the channels added on a power basis, that is:

$$s(t_n)_{\text{rms}} = \chi \sigma \equiv 0.7 \cdot \sigma \quad (4.5)$$

It then follows that the rms modulation depth of the laser when modulated by a modified orthogonal SCM signal is:

$$\text{OMD}_{\text{rms}} = 0.7 \cdot \text{MOD} \quad (4.6)$$

The modulation depth of the laser determines the amount of available signal power, and it must be optimized to maximize the received signal to noise ratio. But as the modulation depth of the laser increases, we limited it because of distortion. Therefore the optimum MOD level had to be determined by iterative simulations where an active modified orthogonal SCM broadband composite signal is passed through the laser model to include distortion “hits” resulting from the signals high peaking characteristic.. This was done in Section 4.2.1a, and it was found that the MOD level before which significant eye closure penalties were observed was MOD=0.20. See Section 4.2.1a for further details.

In determining an estimate of the transmission capacity using each of the modified orthogonal SCM configurations, the MOD must be divided among the subcarrier channels. Since MOD was fixed at 0.20, the power allocated to each channel decreased as the number

of subcarrier channels or payload size, increased. The magnitude of the channel current for each channel was assumed to be the same, and was calculated as follows:

$$i_{\text{Chann,Tx}} = \left(\frac{\text{MOD}}{\sqrt{N}} \right) (I_{\text{bias}} - I_{\text{thres}}) = \left(\frac{0.20}{\sqrt{N}} \right) (105 \text{ mA} - 15 \text{ mA}) = \frac{18 \text{ mA}}{\sqrt{N}} \quad (4.7)$$

Where: $i_{\text{Chann,Tx}}$ = magnitude of the current of one channel input to the laser
 MOD = modulation depth of laser (found to be 0.20)
 I_{bias} = bias current of large signal laser distortion model (105 mA)
 I_{thres} = threshold current of large signal laser distortion model (15 mA)
 N = total number of subcarrier channels

The composite broadband signal was generated in the same manner as in Section 4.1.5, given by (4.3a) and (4.3b), except the resulting line signal is scaled by $i_{\text{Chann,Tx}}$. This signal was then passed through the large signal laser model. Since the passive optical components are distortionless, the optical signal output from the laser junction model was scaled so that the mean value of the received signal corresponded to the expected dc photocurrent at the output of the photodetector, and was 250 μA . This scaling was accomplished by the "optical scaling coefficient" shown in Figure 4.16 and was calculated by (2.38).

Using an eye diagram analysis, the worst case laser distortion vs. payload size of this system was observed for each modulation scheme inclusive of ICI and ISI. This method is stated diagrammatically in Figure 4.16. The worst case distorted channels were observed by demodulating a sample set of channels near the laser's resonance frequency where the most distortion appears. This maximum distortion condition is demonstrated in Figure 2.9.

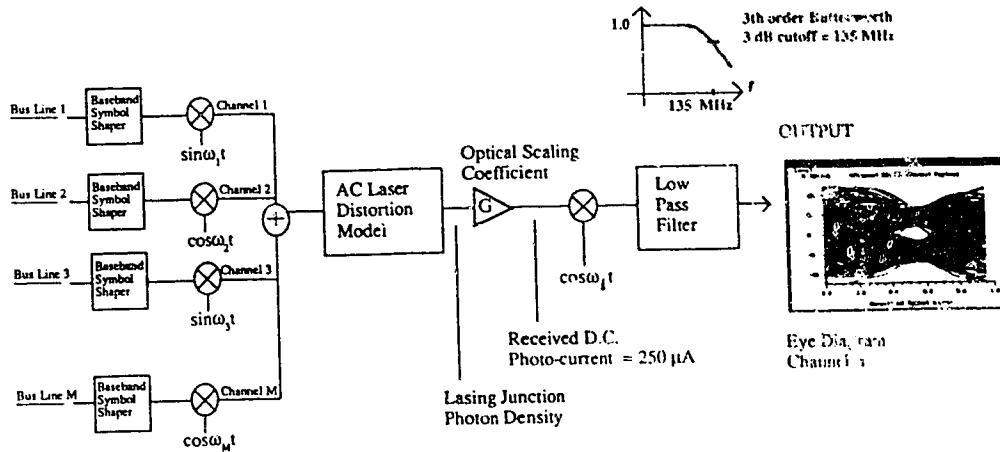


Figure 4.16: Method of Generating Simulations of a Modified Orthogonal SCM Signal on the Optical Link

Demodulation of any given channel was accomplished by multiplying this photocurrent by a unit amplitude sinusoidal local oscillation synchronized in frequency and phase with the incoming channel of interest, and passing the result through a 3rd order Butterworth low pass filter. This filter had a unit gain at dc and a 3dB bandwidth of 135 MHz. The output of the demodulator then was a sequence of symbols where the maximum amplitude of each symbol was some current $i_{\text{Chann,Rx}}$ (4.8), degraded by ISI, ICI and laser distortion.

$$i_{\text{Chann,Rx}} = \frac{1}{2} \left(\frac{\text{MOD}}{\sqrt{N}} \right) I_{\text{Photo}} = \frac{1}{2} \left(\frac{0.20}{\sqrt{N}} \right) 250 \mu\text{A} = \left(\frac{25 \mu\text{A}}{\sqrt{N}} \right) \quad (4.8)$$

Where: $i_{\text{Chann,Rx}}$ = signal current of one channel output from demodulator
 I_{Photo} = expected photo-current output from photodetector (250 μA)

The 1/2 factor in (4.8) arises from multiplication by a unit amplitude sinusoid in the demodulator. Since the BOSS system simulation modules simulating each of the proposed system configurations are very similar, only the one for employing rectangular shaped pulses is given in Appendix 3 with a brief description and sample simulation parameters.

Superimposing all these output symbols resulted in an eye diagram whose vertical size was scaled by (4.4b) to yield an eye opening which was a current directly referenced to

the system noise. Analytically applying the same demodulation procedure on the equivalent noise current referenced to the output of the photodetector (given by (2.39)), resulted in a equivalent peak sinusoid noise current referenced directly to the demodulated signal eye opening for the purposes of BER calculations.

To find the worst case distortion channel, a sample set of four channels was demodulated, three of which were from the six highest channel positions in the payload because this is where the most laser distortion appeared (see Section 2.1.5). Simulations were conducted varying the payload between 5 to 10 Gbit/s to find the worst eye opening for each signal configuration and payload size. The system margin vs. payload size curves were then generated and are given in Section 4.2.2. This was done by calculating the SNR for each case using the peak system noise current, and the worst observed maximum signal current eye opening. The peak noise level and method of calculating system margin by SNR are described in more detail in Section 4.2.1b.

To maintain a BER of 10^{-12} at the receiver output, a signal to noise ratio of 13.9 dB is required assuming Gaussian noise and antipodal binary amplitude shift keying. On this basis, the worst case system margin above a SNR of 13.9 dB was determined, from which penalties may be subtracted for well understood nonideal system components such as mixers, amplifiers, power combiners, etc. The system margin vs payload size curves given in Section 4.2.2 for the different modified orthogonal SCM signals then provides a measure of how feasible this system is to implement.

4.2.1a Method of Determining Modulation Depth (MOD)

In determining the optimum MOD, a system with the half sine baseband pulse shape was assumed with no channels placed in quadrature, having a payload of 25 channels (an equivalent data payload of 5 Gbit/sec) as described by (4.9).

$$i_{sig}(t_n) = i_{Chann,Tx} \cdot s(t_n) \quad (4.9)$$

Where:

$$s(t_n) = \sum_{m \text{ odd}} \sum_{k=0}^{500} a_{nm} f(t_n - kT) \sin(\omega_o + m(2\pi B))t_n + \sum_{m \text{ even}} \sum_{k=0}^{500} b_{nm} f(t_n - kT) \cos(\omega_o + m(2\pi B))t_n$$

{for $1 \leq m \leq 25$ } and {for $0 \leq k \leq 500$ } (4.10)

Where: $\omega_o = 2\pi(400 \text{ MHz})$

$B = 200 \text{ MHz} = 1/T$

a_{nm} and b_{nm} = binary symbols which take on values of either +1 or -1

$t_n = n\Delta T = n(6.25 \text{ pSec})$ = discrete time instants used in simulations,

$f(t)$ = baseband pulse shape employed; (descriptions given in Section 3.2.2)

The laser was biased to $f_{\text{relax}} = 10 \text{ GHz}$, the frequency channels were placed starting at 3 GHz and the receiver low pass filter was a 3rd order Butterworth with a 3 dB bandwidth of 200 MHz. The MOD given by (4.4a) was initially set at 5% and every fifth channel of the 25 channels was demodulated (ie channels 0, 5, 10, 15, 20 & 24). The simulation was run for 500 symbols (or 2.5 μsec) and eye diagrams were generated for all the channels and no significant distortion penalty due was observed. The MOD was incremented in steps of 0.05 through to MOD= 0.40 and the resulting eye diagrams observed. See Appendix 2 to compare the resulting eye diagrams of all channels demodulated for each MOD. It was observed that for MOD levels of greater than 0.20, distortion was observed first of all in the highest frequency channel (channel 24) for MOD= 0.25 and in lower channel positions for higher modulation depths. Therefore it was concluded that for estimating performance of payloads varying from 5 to 10 Gbit/s, a fixed of MOD= 0.20 should be adopted to avoid a burdensome approach of iterating on the MOD for each payload size of interest to find its best MOD.

4.2.1b Calculation of Signal to Noise Ratio and System Margin

To estimate the system margin vs. payload size for each of the proposed modified orthogonal SCM techniques on the optical SCM link, it was necessary to calculate a signal to noise ratio from which a bit error rate estimate could be made. The SNR was calculated by dividing the worst case observed eye opening by the rms noise that would be observed at the output of the receiver. As shown in Figure 4.16 the signal level at the input to the receiver multiplier is equivalent to the received photo-current in the real system. The one-

sided system noise current spectral density at the output of the photo-diode will be $i_{N-rms} = 29.3 \text{ pA}/\sqrt{\text{Hz}}$ (see Section 2.3).

To demodulate any given channel, the photocurrent was multiplied by a unit amplitude sinusoidal carrier and passed through a third order Butterworth low pass filter having a bandwidth of 135 MHz. The system noise current power spectral density at the output from the photodiode is passed through the same demodulator. From all the noise power at the output of the photodiode, what is relevant is only the narrowband noise which appears after demodulation. The noise at the output of the receiver low pass filter may be represented as bandpass narrowband noise before the demodulator which allows splitting the narrowband noise up into quadrature components.

Multiplying this narrowband noise current by a unit carrier then reduces the amplitude of the noise current spectral density by half. Therefore the noise placed at the output of the multiplier would appear as $i'_{N-rms} = i_{N-rms}/2 = 14.65 \text{ pA}/\sqrt{\text{Hz}}$ and is input to the low pass filter. The rms noise current at the output of the low pass filter may then simply be found by multiplying i'_{noise} by the square root of the filter's noise equivalent bandwidth (NEB or $f_{3dB-noise}$). This will result in the equivalent rms noise level at the point where the eye diagram is generated. Required for the BER calculation below is that the noise represented in the form of rms noise:

$$I_{n-rms} = \sqrt{N \cdot NEB} = (i'_{n-rms}) \sqrt{NEB} \quad (4.11)$$

Where: N = noise power spectral density specified at the output of receiver

$$NEB = \zeta(3) \cdot f_{3dB} = 1.0472 \cdot 135 \text{ MHz} = 141.37 \text{ MHz} \quad (*\text{note: using (4.1)})$$

$$i'_{N-rms} = 14.65 \text{ pA}/\sqrt{\text{Hz}}$$

Therefore:

$$(I_{n-rms})^2 = (14.65 \text{ pA}/\sqrt{\text{Hz}})^2 \cdot 141.37 \text{ MHz} = 60.43 \cdot 10^{-15} \text{ A}^2$$

$$I_{n-rms} = 0.1768 \text{ } \mu\text{A}$$

The noise is RIN dominated. Therefore the statistical characteristics of the noise are given by a Poisson distribution (Langevan shot noise source terms in the rate equations as

described in Section 2.1.6) operated on by the coupled rate equations, given the large signal modulation of the bias by the composite broadband signal current. The noise is therefore signal dependent with its statistical behavior influenced by the signal statistics. The statistics of RIN noise are therefore considered too complex for analysis, and consequently we assume that the statistics are Gaussian. The BER is then given by the following analysis:

- a) Assume that the random noise is Gaussian distributed then at the output of the receiver for binary pulses, the bit error rate is

$$\text{BER} = \frac{1}{2} \text{Erfc} \left(\frac{A_1 - A_0}{2\sqrt{2N}} \right) \quad (4.12a)$$

where:

- A_1 = signal amplitude of a logical one
- A_0 = signal amplitude of a logical zero
- N = rms noise power in the bandwidth specified.
= $f_{3\text{dB-Noise}} (i'_{\text{noise}})^2$

- b) In this system an antipodal symbol sequence has been assumed (originated as an NRZ sequence) with an output photocurrent of
 $+I_{\text{eye-max}}$ = maximum value of the eye corresponding to a logical 1
 $-I_{\text{eye-max}}$ = minimum value of the eye corresponding to a logical 0
therefore:

$$\frac{A_1 - A_0}{2} = \frac{I_{\text{eye-max}} - (-I_{\text{eye-max}})}{2} = I_{\text{eye-max}} \quad (4.12b)$$

- c) Noise: The noise power has been defined in terms of the rms spectral noise current, (in units of $A/\sqrt{\text{Hz}}$) therefore multiplication by the square root of the noise equivalent bandwidth (NEB or $f_{3\text{dB-Noise}}$) and will yield the rms noise current

$$I_{n\text{-rms}} = \sqrt{N} = i'_{N\text{-rms}} \sqrt{f_{3\text{dB-noise}}} = 0.1768 \mu\text{A} \quad (4.12c)$$

- d) Thus the BER equation for this implementation reduces to

$$\text{BER} = \frac{1}{2} \text{Erfc} \left(\frac{I_{\text{eye-max}}}{\sqrt{2} I_{n\text{-rms}}} \right) \quad (4.12d)$$

- e) Assume that BER maximum = 10^{-12} then from tables

$$\left(\frac{I_{\text{eye-max}}}{\sqrt{2} I_{n\text{-rms}}} \right)_{\text{BER} < 10^{-12}} = 4.9738 \rightarrow \text{SNR}_0 \equiv 20 \log \left(\frac{I_{\text{eye-max}}}{\sqrt{2} I_{n\text{-rms}}} \right) = 13.9 \text{ dB} \quad (4.12c)$$

The system margin over which a BER= 10^{-12} may be maintained for any given payload simulation may therefore be obtained by knowing the worst case maximum eye opening (in μA) and subtracting 13.9 dB:

$$\text{System Margin} \equiv \text{SNR}(\text{dB}) - 13.9 \text{ dB} \quad (4.13a)$$

where:

$$\text{SNR} \equiv 20 \cdot \log \left(\frac{I_{\text{eye-max}}}{\sqrt{2} I_{\text{N-rms}}} \right) \quad (4.13b)$$

The system margin then tells us how much the system assumptions may change in a real system due to imperfections causing degradations (such as non-ideal mixers, amplifiers, power splitters/combiners, etc.) in the received SNR (as defined by (4.13b) and therefore how feasible it is to physically implement this system.

4.2.2 Results of Simulated Transmission of Orthogonal SCM Signals on Lightwave Link

Finally we will consider the SNR performance as a function of payload size on the assumed optical link of modified orthogonal SCM system with half sine and rectangular shaped pulses without quadrature components, and modified O-QAM using the half sine shape. The procedure for generating the system margin curves is briefly revisited, followed by the results. The modified orthogonal SCM broadband composite signal was generated for each configuration and scaled by the magnitude of the current calculated by (4.7) given the number of channels, M. The modified orthogonal SCM signal was then passed through the laser model. The output of the laser model was scaled by the "optical scaling coefficient" given by (2.38) to result in an expected photocurrent with an average level of $250 \mu\text{A}$. Each channel of interest was demodulated and the eye diagram was generated which was equivalently scaled by (4.8) to yield a maximum eye value referenced directly to the rms noise level given by (4.12c). The SNR was then calculated using (4.13b). Subtracting 13.9 dB according to (4.13a) then resulted in a system margin; the margin versus payload size for different systems is shown in Figures 4.17a, 4.18a and 4.19a.

To identify how much laser distortion was present, the expected system margin without laser distortion was calculated. The system margin of a distortionless system with the same received signal as in our system model was calculated using (4.13a) and (4.13b) (where $I_{eye-max}$ is calculated from (4.8); note that N , the number of channels, is replaced by M for clarity) and subtracting the ICI and ISI penalties (in dB) corresponding to the scheme used. This relation is described by (4.14), and plotted in Figures 4.17a, 4.18a and 4.19a.

$$SNR_{NoDistortion} \equiv 20 \cdot \log \left(\frac{MOD}{2\sqrt{M}} \frac{I_{Photo}}{\sqrt{2} I_{N-rms}} \right) - ICI_{dB} - ISI_{dB} \quad (4.14)$$

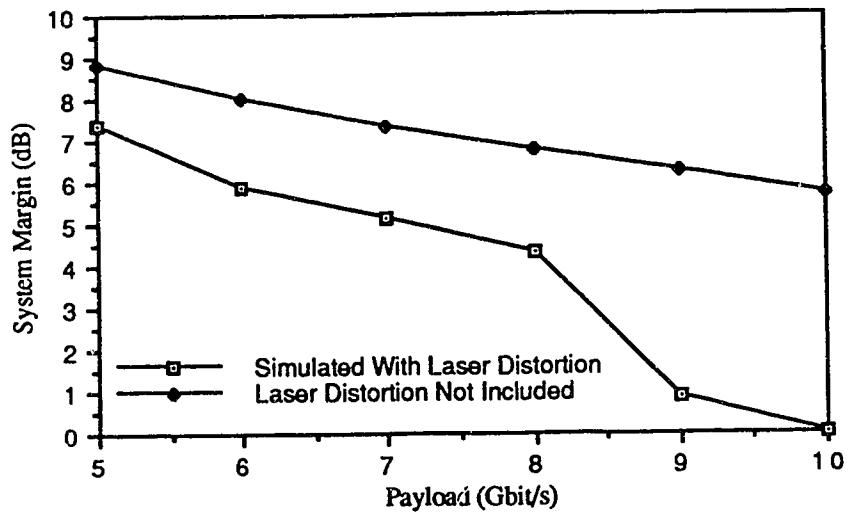


Figure 4.17a- Trade Off Between Payload Size and Link Margin for Half Sine Shape, No Quadrature Component

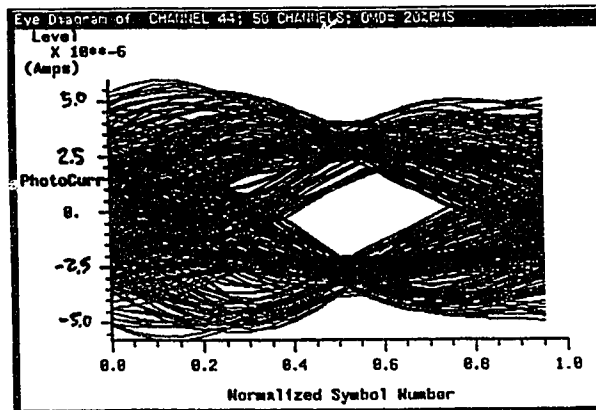


Figure 4.17b- Worst Case Eye Diagram for Half Sine Shaped Pulses- No Quadrature Component, 10 Gbit/s

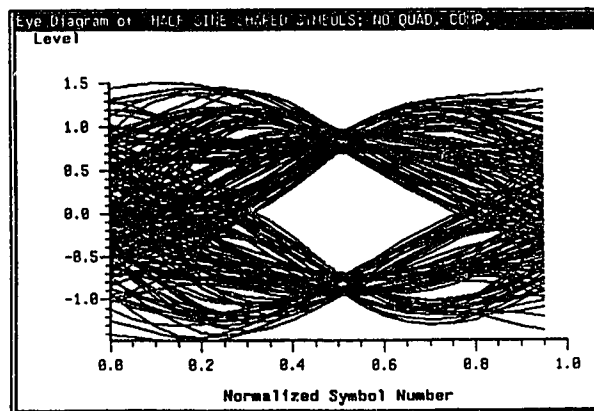


Figure 4.17c- Eye Diagram with No Laser Distortion Present- Half Sine Shape, No Quadrature Subchannels

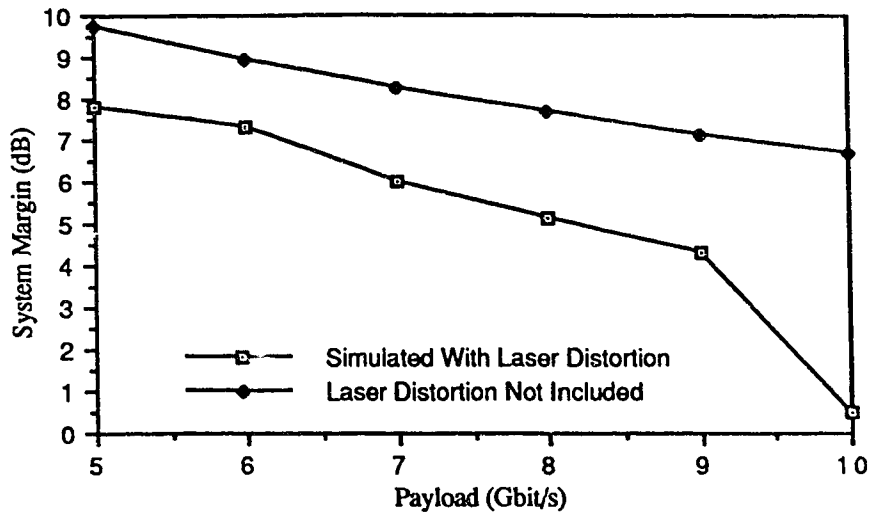


Figure 4.18a- Trade Off Between Payload Size and Link Budget Margin for Rectangular Shape Pulses

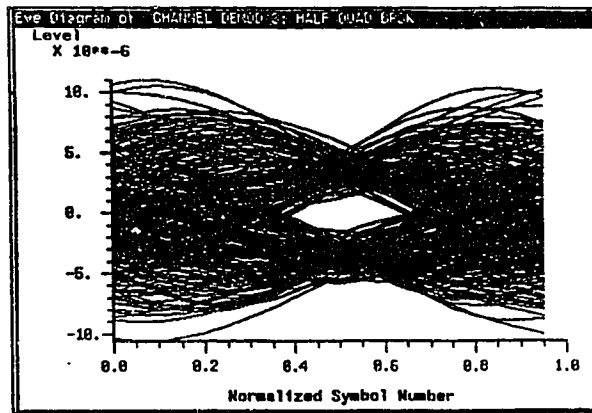


Figure 4.18b- Worst Case Eye Diagram for Rectangular Pulse Shape, 10 Gbit/s

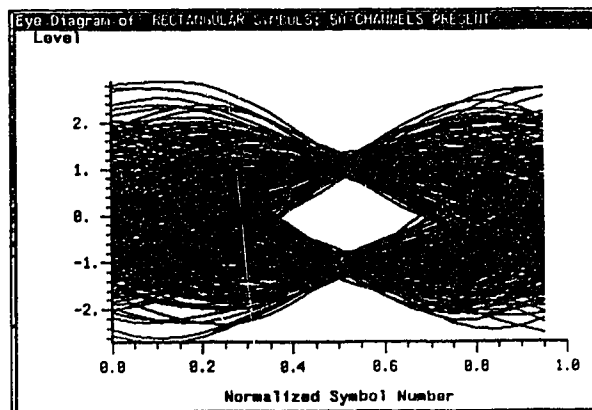


Figure 4.18c- Eye Diagram with No Laser Distortion Present-Rectangular Shape

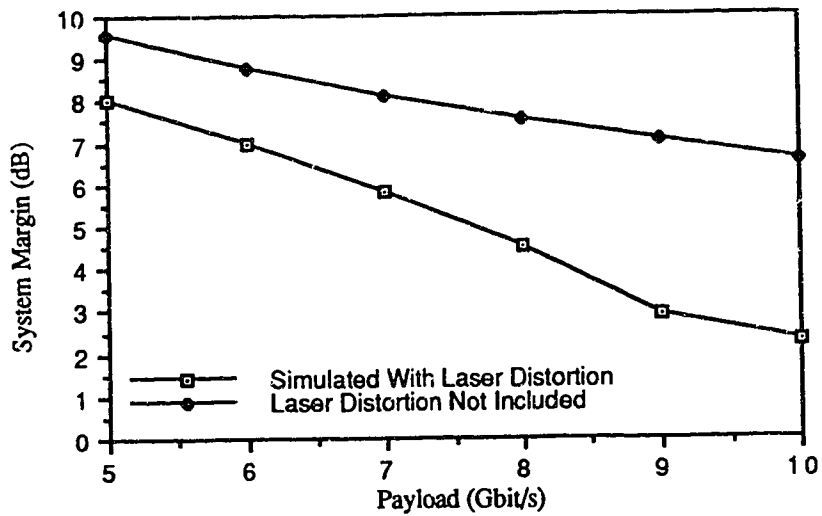


Figure 4.19c- Trade Off Between Payload Size and System Margin for Half Sine Pulses, With Quadrature Component

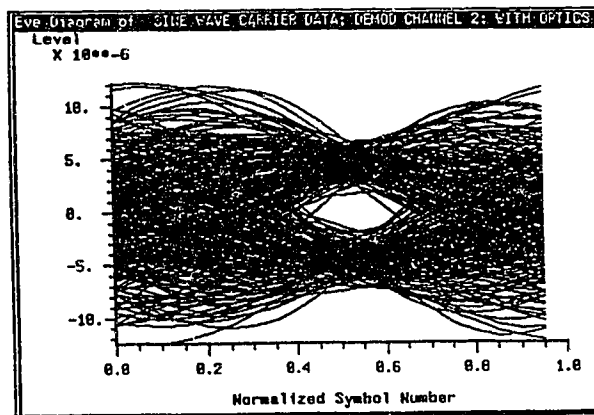


Figure 4.19b- Worst Case Eye Diagram for Half Sine Shaped Pulses- With Quadrature Component, 10 Gbit/s

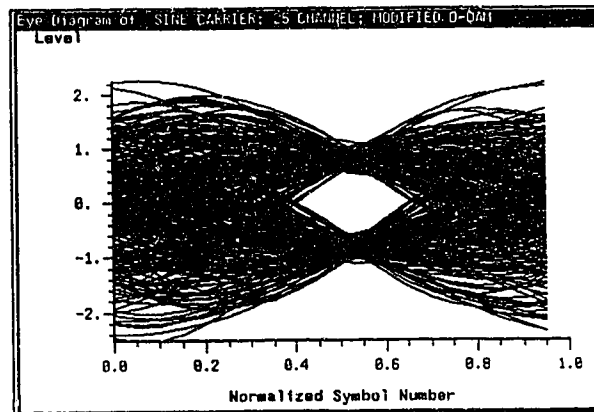


Figure 4.19c- Eye Diagram with No Laser Distortion Present-Half Sine Shape, Full Quadrature Subchannels Present

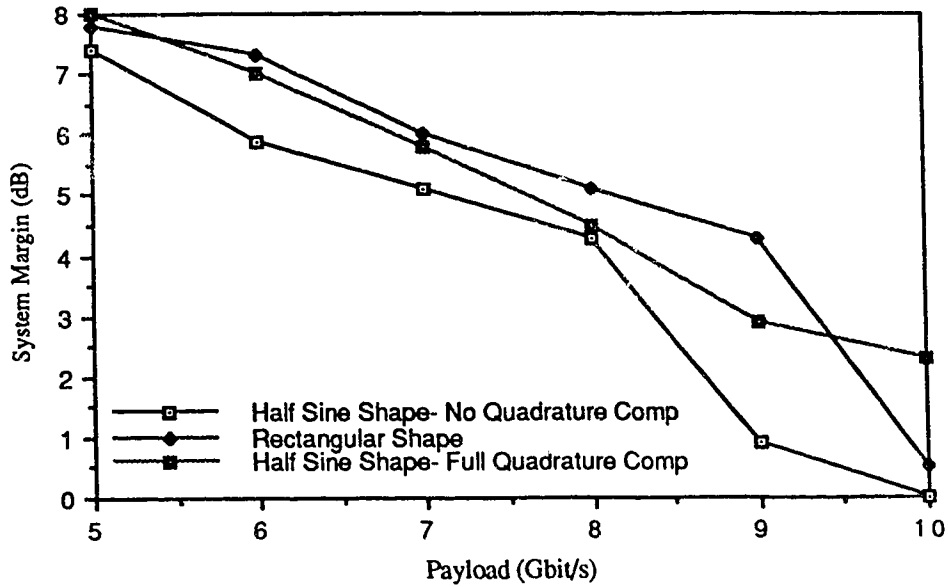


Figure 4.20d- Summary Plot of the System Margin vs. Payload Size Tradeoff

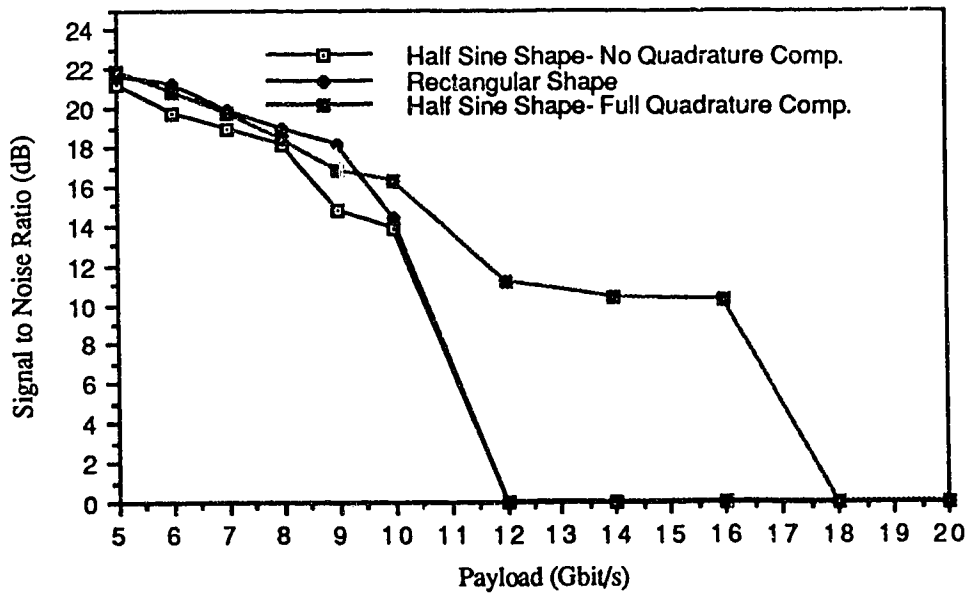


Figure 4.20e- Trade Off Between SNR and Payload Size for All Shapes

From these results we can make the following observations:

1. Figures 4.17b, 4.18b and 4.19b demonstrate that the system with half sine shaped pulses and no quadrature subchannels has the widest sampling region in the eye compared to other configurations in the presence of distortion.

2. The distortion penalty introduced by the laser is approximately 2 dB for payload sizes less or equal to 8 Gbit/s, and is less severe at 9 and 10 Gbit/s for modified O-QAM employing the half sine shape, than for other configurations. This arises because the modified O-QAM signal only has a bandwidth of 5 GHz carrying 10 Gbit/s whereas the other configurations have a 10 GHz bandwidth and therefore are subject to more severe distortion in the highest channels.

3. Assuming no phase degradations in the transmitter or receiver, full quadrature half sine shaped pulse system yields better performance than the one with rectangular shaped pulses at 10 Gbit/s; for lower rates, the opposite is the case.

4. Figure 4.21 demonstrates that the performance of the modified O-QAM system employing half sine shaped pulses is acceptable up to 16 Gbit/s, although the eye opening is reduced. Above 16 Gbit/s complete eye closure was observed.

Chapter 5

SUMMARY AND CONCLUSIONS

This thesis has introduced the modulation technique of modified orthogonal SCM as an alternate method to multiplex a high speed computer bus for a point to point transport on a conventional lightwave SCM link. A thesis summary, conclusions and suggestions for further work are now presented.

5.1 THESIS SUMMARY

In Chapter 1 the problem of multiplexing a 100 line computer bus operating at a clock rate of 200 MHz was identified for a point to point 100 m transport. Since the size of the payload is 20 Gbit/s, it was necessary to consider optical transmission technology. Due to the complexity and cost of using a conventional TDM system, it was concluded that digital subcarrier multiplexing (SCM) techniques would be considered. Some background information was given about SCM and the intense research interest in this area which has resulted in significant improvements in laser linearity and noise.

Following the background information in Chapter 1, Chapter 2 identified the most significant signal impairments introduced by the optical link and how they could be modelled in a worst case analysis. Resonance distortion and relative intensity noise were the dominant degradations in this system. Resonance distortion was modelled by numerically solving in time the coupled single mode rate equations whose parameters represented a multimode InGaAsP SCM laser. The laser resonance distortion model was benchmarked with analytical expressions and found to be conservative for the dominant second order products. With the carrier plan given by (2.30) it was found that the most distortion appeared at frequencies closest to the laser's resonance frequency and were caused by second order intermodulation products. Also it was found that system noise in the receiver was RIN limited.

Keeping the transmission medium in mind, the moderate complexity and bandwidth efficient technique of modified orthogonal SCM was developed in Chapter 3. It was shown that channels carrying synchronous data symbols which employed simple baseband pulse shaping may be multiplexed in frequency with no guard bands. This was accomplished by taking advantage of synchronism in the data streams and phasing of the equispaced carriers to force half of the channels to be orthogonal. It was shown that any carrier modulated by an amplitude shift keyed symbol stream at a rate of B symbols/s is orthogonal to all other channels whose carriers are an integer multiple of B Hz away in frequency and offset by 90° . The only requirement for the symbol shape is that it be symmetrical. This extends the previously known technique of orthogonal SCM which required that the baseband pulse shape be bandlimited to B Hz for no ICI to occur. Modified orthogonal SCM then relaxes this bandlimiting constraint for the benefit of allowing baseband pulse shapes which are suitable for a multiGbit/s application; this permits removal of the Nyquist filtering constraint. The price for that, however, is some signal degradation appearing in the form of ICI and ISI. Assuming antipodal BASK, two implementation types were identified. The first type was one with no quadrature subchannels which achieved a bandwidth efficiency of 1 bit/s/Hz. The second implementation type involved a bank of quadrature subchannels resulting in a bandwidth efficiency of 2 bit/s/Hz; it was called modified O-QAM.

Chapter 4 reports performance of the efficient modified orthogonal SCM technique employing simple baseband pulse shapes, first in an ideal transmission medium, then in the presence of laser distortion and noise. An eye diagram analysis was conducted to determine how much ICI and ISI arose when Nyquist baseband symbol shaping and receiver filtering was removed. A Butterworth receiver filter was assumed, and it was found that the SNR before decision was maximized by using a 3rd order filter with a 3dB bandwidth of 135 MHz. It was also found that the configuration employing the rectangular shape with no quadrature subchannels resulted in a total eye closure penalty of 2.5 dB due

to ICI and ISI. The half sine shape was a close second with a total penalty of 3.5 dB. The sine square shape was also examined, however it was eliminated as a candidate because it had a total penalty of 6.7 dB. The only shape suitable for modified O-QAM was observed to be the half sine, and resulted in a total eye closure penalty of 5.9 dB. It was found that the implementation using rectangular shaped pulses was least sensitive to phase errors in the receiver, where they are the most difficult to control. The signal statistics of each configuration were examined by generating a modified orthogonal SCM line signal carrying 50 random uncorrelated data streams. It was found that the channels add in such a manner that their combined power is less than that of the Gaussian equivalent case, and the peak excursions which create possibility for distortion "hits" when passed through a nonlinear device were found to be less severe than for the Gaussian case.

In the second section of Chapter 4 the transport capacity of the digital SCM system employing modified orthogonal SCM was examined. To observe the time domain effects of the frequency dependent laser distortion, it was necessary to have all active subcarrier channels present. This required 800 samples per symbol, making a Monte Carlo simulation impossible with available computing power. Alternatively an eye diagram analysis was performed with simulations running for 500 symbols. The modulating current for each channel was calculated on an rms basis from a MOD value of 0.20. The parameter MOD was arbitrarily defined for simulation purposes as being the equivalent rms modulation depth calculated from the addition of channels on a power basis. This MOD was determined by iteration. It was concluded from the signal statistics of each configuration that the true rms level of the sum of all channels was in fact less than that calculated assuming addition of channels on a power basis. However, the benefit of lower total power was offset by large peak excursions. This made it imperative to use a laser distortion model with all active channels present to accurately predict how an active modified orthogonal SCM signal is distorted by the laser.

To examine the worst case of laser distortion an eye diagram analysis was performed by demodulating a sample set of channels closest to the laser's resonance frequency, which was set at 10 GHz. Demodulation was accomplished using homodyne downconversion and an optimized Butterworth low pass filter. Assuming that the RIN dominated noise (predicted in Chapter 2) is Gaussian and a BER $< 10^{-12}$ is desired, system margins were calculated for different payload sizes from the eye diagram analysis in the presence of laser distortion. A 10 Gbit/s transport capacity was observed for each configuration with 0 dB margin using the half sine shape with no quadrature subchannels, 0.5 dB margin using the rectangular shaped pulses and 2.5 dB margin with modified O-QAM utilizing the half sine shape. For capacities smaller than 9 Gbit/s rectangular shaped pulses were observed to perform 0.5 dB better than modified O-QAM using the half sine shape and 1.0 dB better than the half sine shape with no quadrature subchannels present.

Summary of System Parameters and Technology

- Bandwidth efficiencies of 1 to 2 bit/s/Hz are achievable using no guard bands and simple or no baseband pulse shaping with modified orthogonal multiplexing.
- Conventional microwave components may be used to generate and demodulate the modified orthogonally multiplexed signal.
- Using a resonance distortion model for a "1984" semiconductor laser gave 10 Gbit/s throughput with a 2.5 dB system margin for internal system distortion; possible phase error penalties will reduce this margin.

5.2 CONCLUSIONS

- Considering only the observed system capacity, the modified O-QAM implementation employing half sine shaped pulses has the largest system margin at 10 Gbit/s, however this scheme is very sensitive to downconversion phase errors and therefore would be difficult to realize. Rectangular shaped pulses performed better for capacities less than 10 Gbit/s

and possess the best immunity to phase errors in the receiver where they are most difficult to control. Therefore it is concluded that the best performance could be achieved with the rectangular shaped pulses and no quadrature subchannels present. A bandwidth efficiency of 1 bit/s/Hz may be achieved using this technique.

-The dominant source of distortion from the directly modulated semiconductor laser are second order intermodulation products, which are most significant near the lasers resonance frequency.

-The system noise is RIN dominated. A significant increase in system margin may be achieved by reducing the RIN because of the large received optical power. This is shown in Figure 5.1. Reducing the RIN level for this system results in system margin increases of up to 5.5 dB for RIN = -155 dB/Hz. Little is gained by further reducing the RIN because the noise then becomes limited by receiver shot noise and preamplifier thermal noise.

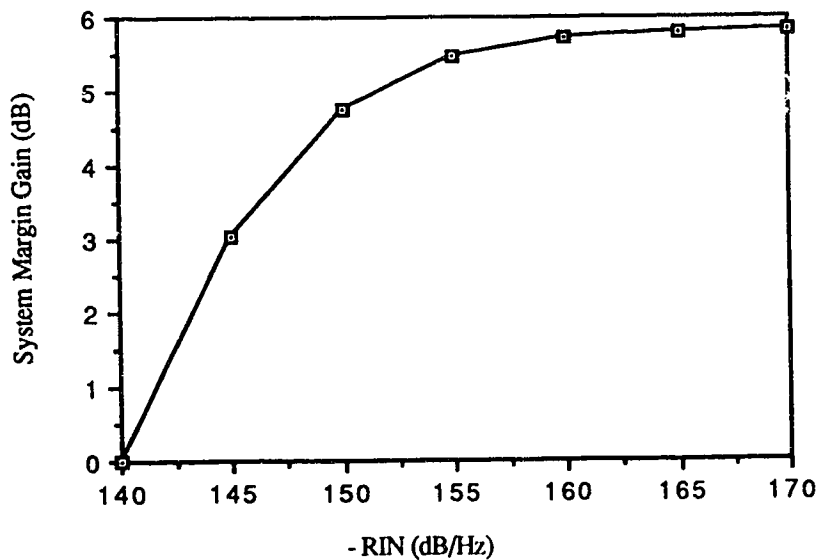


Figure 5.1- System Margin Gain as a Function of Laser RIN, Relative to RIN=-140 dB/Hz

-System margins of less than or equal to 2.5 dB have been achieved when all the system components except the laser are ideal. Penalties due to phase errors, delay distortion, or amplitude distortion of all other components have not been included in the margin calculation. Therefore it is concluded that transporting 10 Gbit/s in a real link of this type is not possible unless the system margin is increased.

-Maximum RIN levels of -155 dB/Hz over a 10 GHz range are possible in commercially available Nd:YAG lasers [50]. A Nd:YAG laser cannot be directly modulated as a semiconductor laser, and therefore an external modulator is required. External modulators are inherently nonlinear, but if biased properly, the second harmonics may be cancelled out [23]. Using predistortion circuitry it is possible to minimize third order distortion products [51]. This has been one of the most recent developments in the area of SCM analog TV distribution satisfying the tight noise and linearity requirements for video signals. Therefore a change in approach toward using a source and modulator of this type will reduce the RIN and second order distortion levels, which currently limit system performance.

5.3 FURTHER WORK

Since this has been the first exploration of the technique of modified orthogonal SCM applied to subcarrier multiplexing, more research can be done. The following are but a few avenues that further work might take.

(1) Formulation of a carrier and clock recovery scheme which is phase adaptive to minimize the effects of delay and amplitude distortion on the modified orthogonal SCM signal. One approach may be to utilize the high degree of synchronism existing between signals in different channels and use their cross-correlations to adapt a number of local oscillators and

the decision timing clock [50]. Another approach may be to send a carrier along with the payload from which the carriers may be derived in the receiver.

(2) An analysis should be conducted into the effects of delay distortion on the modified orthogonal SCM signal and how they may be minimized.

(3) A study should be pursued to examine using an externally modulated low noise Nd:YAG laser to increase the system margin by lowering the levels of RIN and second order intermodulation distortion products. Current technology suggests that an increase in system margin of at least 5 dB will result.

(4) A survey should be conducted of conventional microwave components available to generate the modified orthogonal SCM. By identifying the maximum phase and distortion penalties introduced, a realistic estimate of the system margin required to implement a modified orthogonal SCM signal may be found.

(5) If sufficient system margin is made possible, examination of multilevel amplitude shift keying (instead of binary) in the modified orthogonal SCM signal may provide higher bandwidth efficiencies. It may be possible to build logic necessary for multilevel modulators and demodulators using CMOS; current technology is close to 200 MHz.

(6) Other areas of application for modified orthogonal SCM may be;

- Long haul transmission with aid of low noise fibre amplifiers.
- Metropolitan and local area fibre network distribution of synchronous payloads; such as uncompressed digital video.
- Wireless local area networks operating in the 18 GHz range for inbuilding applications [53].

References

1. R. S. Tucker, et. al., "16 Gbit/s Fibre Transmission Experiment using Optical Time-Division Multiplexing", *Electronics Letters*, Nov. 19, 1987, Vol. 23, No. 24, pp. 1270-1271.
2. R. Olshansky, et. al., "Subcarrier Multiplexed Lightwave Systems for Broad Band Distribution", *L. of Lightwave Tech.*, Vol. 7, No. 9, Sept. 1989, pp. 1329-1341.
3. T. E. Darcie, "Subcarrier Multiplexing for Multiple-Access Lightwave Networks", *L. of Lightwave Tech.*, Vol. LT-5, No. 8, Aug., 1987, pp. 1103-1108.
4. W. Way, R. S. Wolff, and M. Krain, "A 1.3 μ m 35 km Fiber Optic Microwave Multicarrier Transmission System for Satellite Earth Stations", *J. of Lightwave Technology*, Vol. LT-5, pp. 1325-1332, 1987.
5. H. Blauvelt et. al., "Reduced Insertion Loss of X-Band RF Fiber-Optic Links", *IEEE Trans. on Microwave Theory and Techniques*, Vol. 38, No. 5, pp. 662-663, May 1990.
6. L. Linnell, "A Wide-Band Local Access System Using Emerging Technology Components", *IEEE J. Selected Areas Commun.*, vol. SCA 4, p. 612, 1986.
7. C. A. Brackett, "Dense WDM Networks", in *Proc. 14th Euro., Conf. Opt. Commun.*, Brighton, U.K., Sept. 11-15, 1988, pp. 533-540.
8. E. J. Bachus, et. al., "Ten Channel Coherent Optical Fiber Transmission", *Electron. Lett.*, Vol. 22, pp. 1002-1003, 1986.
9. T. E. Darcie, et. al., "Resonant pin-FET Receivers for Lightwave Subcarrier Systems", *J. of Lightwave Tech.*, Vol. 6, No. 4, pp. 582-589, April 1988.
10. P. M. Hill, "A 20-Channel Optical Communication System Using Subcarrier Multiplexing for the Transmission of Digital Video Signals", *J. of Lightwave Technology*, Vol. 8, No. 4, pp. 554-560, April, 1990.
11. D. D. Tang, "Multigigabit Capacity Fiber-Optic Video Distribution using BPSK Microwave Subcarriers", *OFC 89*, Wed., 8th, pg WC4.
12. W. I. Way, "Fiber-Optic Transmissions of Microwave 8-phase-PSK and 16-ary Quadrature-Amplitude-Modulated Signals at the 1.3 μ m Wavelength Region", *IEEE/OSA J. Lightwave Technology*, Vol. 6, No. 2, Feb., 1988, pp. 273-280.
13. T. E. Darcie, et. al., "Multichannel Bidirectional 1.44 Gbit/s Lightwave Distribution System using Subcarrier Multiplexing," *Electronics Letters*, May 26, 1988, Vol. 24, No. 11, pp. 649- 650.
14. J. E. Bowers, "Optical Transmission using PSK Modulated Subcarriers to 16 GHz", *Electron. Lett.*, Vol. 22, pp. 1110-1120, 1986.

15. R. Olshansky, et. al., "InGaAsP Buried Heterostructure Laser with 22-GHz Bandwidth and High Modulation Efficiency", *Electron. Lett.*, Vol. 23, pp. 839-841, 1987.
16. William B. Jones, Jr., "Introduction to Optical Fiber Communication Systems", Holt, Rinehart & Winston, Inc., 1988.
17. C. B. Su and V. A. Lanzisera, "Ultra-High-Speed Modulation of 1.3 μm InGaAsP Diode Lasers", *IEEE J. of Quantum Electron.*, Vol. QW-22, No. 9, Sept. 1986, pp. 1568-1578.
18. R. Olshansky et. al., "Frequency Response of 1.3 μm InGaAsP High Speed Semiconductor Lasers", *IEEE J. of Quantum Electron.*, Vol. QE-23, No. 9, Sept. 1987, pp. 1410-1418.
19. J. E. Bowers et. al., "High-Speed InGaAsP Constricted-Mesa Lasers", *IEEE J. of Quantum Electron.*, Vol QE-22, No. 6, June 1986, pp. 833-844.
20. R. S. Tucker and I. P. Kaminow, "High-Frequency Characteristics of Directly Modulated InGaAsP Ridge Waveguide and Buried Heterostructure Lasers", *J. of Lightwave Technology*, Vol. LT-2, No. 4, Aug. 1984, pp. 385-393.
21. R. S. Tucker, "High-Speed Modulation of Semiconductor Lasers", *J. of Lightwave Technology*, Vol. LT-3, No. 6, Dec. 1985, pp. 1180-1192.
22. K. A. Simons, "The Decibel Relationships Between Amplifier Distortion Products", *Proceedings of the IEEE*, Vol.-88, No.7, July 1970, pp. 1071-1086.
23. T. E. Darcie and G. E. Bodeep, "Lightwave Subcarrier CATV Transmission Systems", *IEEE Trans on Microwave Theory and Tech.*, Vol. 38, No. 5, May 1990, pp. 524-533.
24. W. I. Way, "Subcarrier Multiplexed Lightwave Systems", Tutorial OFC 89, Houston, Texas, Feb 6-9, 1989, pp. 55-103.
25. W. I. Way, "Frequency-Dependant and Frequency-Independent Nonlinear Characteristics of a High-Speed Laser Diode", *IEEE MTT-S Digest*, Vol. KK-6, 1988, pp. 991-994.
26. K. Y. Lau and A. Yariv, "Intermodulation Distortion in a Directly Modulated Semiconductor Injection Laser", *Applied Physics Letters*, Vol 45, No. 10, 15 November, 1984, pp. 1034-1036.
27. T. E. Darcie, et. al., "Intermodulation and Harmonic Distortion in InGaAsP Lasers", *Electronics Letters*, Vol. 21, pp. 665-666, 1985, erratum, *ibid.*, Vol. 23, pp. 619, 1986.
28. P. Iannone and T. E. Darcie, "Multichannel Intermodulation Distortion in High-Speed GaInAsP Lasers", *Electronics Letters*, 1987, Vol. 23, No. 25, pp. 1361-1362.
29. W. I. Way, "Large Signal Nonlinear Distortion Prediction for a Single-Mode Laser Diode Under Microwave Intensity Modulation", *J. of Lightwave Tech.*, Vol. LT-5, No. 3, March, 1987, pp. 305-315.

30. W. I. Way, "Optical Feedback on Linearity Performance of 1.3- μ m DFB and Multimode Laser Under Microwave Intensity Modulation", *J. of Lightwave Tech.*, Vol. 6, No. 1, Jan. 1988, pp. 100-108.
31. P. Neusy, W. F. McGee, "Effects of Laser Nonlinearities on TV Distribution using Subcarrier Multiplexing", *Canadian Conference on Electrical and Computer Engineering*, Montreal, PQ, Canada, Sept. 17-20, 1989, pp. 833-836.
32. Klaus Peterman and Gunther Arnold, "Noise and Distortion Characteristics of Semiconductor Lasers in Optical Fiber Systems", *IEEE J. of Quantum Electronics*, Vol. QE-18, No. 4, April 1982, pp. 543-555.
33. P. Hill et. al., "Reduction of Relative Intensity Noise in 1.3 μ m InGaAsP Semiconductor Lasers", *Applied Physics Letters*, Vol 50, No. 20, May 18, 1987, pp. 1400-1402.
34. W. W. Ng, et. al., "Dynamic Characteristics of High Speed p-Substrate GaInAsP Buried Crescent Lasers", *J. of Lightwave Tech.*, Vol. 7, No. 3, March 1989, pp. 560-567.
35. K. Sato, "Intensity Noise of Semiconductor Laser Diodes in Fiber Optic Analog Video Transmission", *IEEE J. of Quantum Electron.*, Vol QE-19, No. 9, Sept., 1983, pp. 1380-1391.
36. J. E. Bowers et. al., "Long Distance Fiber-Optic Transmission of C-Band Microwave Signals to and from a Satellite Antenna", *J. of Lightwave Tech.*, Vol. LT-5, No. 12, Dec. 1987, pp. 1733-1741.
37. J. L. Gimlett, "Ultrawide Bandwidth Optical Receivers", *J. of Lightwave Tech.*, Vol. 7, No. 10, Oct., 1989, pp. 1432-1437.
38. M. A. R. Violas, et. al., "10 GHz Bandwidth Low-Noise Optical Receiver using Discrete Commercial Devices", *Electron. Lett.*, Vol. 26, No. 1, Jan. 4, 1990, pp. 35-36.
39. R. W. Chang, "Synthesis of Band-Limited Orthogonal Signals for Multichannel Data Transmission", *Bell Systems Technical Journal*, Vol. 45, Dec. 1966, 1775-1796.
40. D. D. Tang "Design and Performance of a Fiber-Optic Video Distribution System using BPSK Microwave Subcarriers". *IEEE J. on Selected Areas in Comm.*, Vol. 8, No. 7, Sept. 1990, pp. 1304-1312.
41. B. R. Saltzberg, "Performance of an Efficient Parallel Data Transmission System", *IEEE Trans. on Communications*, Vol. Com-15, Dec. 1967, pp. 805-811.
42. B. Hirosaki, "Advanced Groupband Data Modem Using Orthogonally Multiplexed QAM Technique", *IEEE Tran. on Communications*, Vol. Com-34, Vol. 6, June 1986, pp. 587-592.
43. B. Hirosaki, "An Orthogonally Multiplexed QAM System Using the Discrete Fourier Transform", *IEEE Trans. on Communications*, Vol. Com-29, No. 7, July 1981, pp. 982-989.

44. B. Hirosaki, "An Analysis of Automatic Equalizers for Orthogonally Multiplexed QAM Systems", IEEE Trans. on Communications, Vol. Com-19, No. 1, Jan. 1980, pp. 73-83.
45. S. B. Weinstein, "Data Transmission by Frequency-Division Multiplexing Using the Discrete Fourier Transform", IEEE Trans. on Communications, Vol. Com-19, No. 5, Oct. 1971, pp. 628-634.
46. J. A. C. Bingham, "Multicarrier Modulation for Data Transmission: An Idea Whose Time Has Come", IEEE Communications Magazine, May 1990, pp. 5-14.
47. Hansell, "Filter Design and Evaluation", Wiley, London, 1976.
48. L. Petermann, "Laser Diode Modulation and Noise", Kluwer Academic Publ., Boston, MA, 1990.
49. G. deWitte, Private Communication.
50. Wisper 1.3 Product Line; Amoco Laser Company, 1251, Frontenac Rd. Naperville, Illinois.
51. R. B. Childs and V. A. O'Byrne, "Predistortion Linearization of Directly Modulated DFB Lasers and External Modulators for AM Video Transmission", OFC 90.
52. D. L. Harnett, "Statistical Methods", third edition, 1982, Addison-Wesley Publ. Co.
53. T. E. Bell, "Global Cellular System Planned", The Institute, A news supplement to IEEE Spectrum, Vol. 14, No. 8, Sept., 1990, page 11.
54. BOSS Simulation Manual.

Appendix 1- Derivation of Received Channel Spectra

This appendix presents the derivation of (3.9a) and (3.11a) given in the orthogonal analysis of nonbandlimited channels. Required in Section 3.2.1 is the spectrum of the signal received by transmitting a single nonbandlimited pulse $f(t)$, modulating a cosine or sine carrier in the system represented by Figure 3.4. Without any loss of generality, an even numbered k^{th} cosine subchannel was selected to be the reference subchannel in which the ICI from all other subchannels appear. To derive whether or not ICI arises from any other cosine subchannel, a general expression of the received spectrum for a pulse transmitted in any $(k+L)^{\text{th}}$ channel is required (where k is even and L is any positive or negative integer). The result for any cosine subchannel was stated by (3.9a). Similarly (3.11a) was given for any $(k+L)^{\text{th}}$ sine subchannel.

A1.1 Interference from a Cosine Subchannel

Shown in Figure 3.4 for any cosine subchannel, is that the transmitted baseband pulse for all even numbered positions is $f(t)$, and in any odd cosine subchannel it is $f(t - T/2)$ (where $T = 1/B$). For any $(k+L)^{\text{th}}$ cosine subchannel the transmitted symbol may be represented as follows:

$$f_{\text{cos},(k+L)}(t) = b_{k+L} f\left(t - \frac{T}{4} (1 - (-1)^L)\right) \quad (\text{A1.1})$$

where: b_{k+L} is the information symbol

The Fourier transform of (A1.1) is

$$F_{\text{cos},(k+L)}(\omega) = \int_{-\infty}^{\infty} b_{k+L} f\left(t - \frac{T}{4} (1 - (-1)^L)\right) e^{-j\omega t} dt = b_{k+L} F(\omega) \exp\left\{-j\omega \frac{T}{4} (1 - (-1)^L)\right\} \quad (\text{A1.2})$$

where $F(\omega)$ is the Fourier transform of $f(t)$.

With the assumed subchannel spacing of B Hz, the corresponding modulated signal in the $(k+L)^{\text{th}}$ cosine subchannels will be:

$$s_{\text{Tx},\text{cos},(k+L)}(t) = \cos(\omega_k + 2\pi L B) \cdot b_{k+L} f\left(t - \frac{T}{4} (1 - (-1)^L)\right) \quad (\text{A1.3})$$

In frequency this corresponds to the convolution:

$$S_{Tx,cos,(k+L)}(\omega) = b_{k+L}F(\omega)\exp\left\{-j\omega\frac{T}{4}(1-(-1)^L)\right\} \otimes \frac{1}{2}\left\{\delta(\omega+\omega_k+2\pi BL) + \delta(\omega-\omega_k-2\pi BL)\right\} \quad (A1.4)$$

Simplifying (A1.4) results in:

$$S_{Tx,cos,(k+L)}(\omega) = \frac{b_{k+L}F(\omega+\omega_k+2\pi B)}{2}\exp\left\{-j(\omega+\omega_k+2\pi BL)\frac{T}{4}(1-(-1)^L)\right\} + \frac{b_{k+L}F(\omega-\omega_k-2\pi B)}{2}\exp\left\{-j(\omega-\omega_k-2\pi BL)\frac{T}{4}(1-(-1)^L)\right\} \quad (A1.5)$$

This signal transmitted via a link with the transfer function $H(\omega)$ yields the received signal, whose spectrum is given by:

$$S_{Rx,cos,(k+L)}(\omega) = \frac{b_{k+L}H(\omega)}{2}F(\omega+\omega_k+2\pi BL)\exp\left\{-j(\omega+\omega_k+2\pi BL)\frac{T}{4}(1-(-1)^L)\right\} + \frac{b_{k+L}H(\omega)}{2}F(\omega-\omega_k-2\pi BL)\exp\left\{-j(\omega-\omega_k-2\pi BL)\frac{T}{4}(1-(-1)^L)\right\} \quad (A1.6)$$

A1.2 Interference from a Sine Subchannel

Figure 3.4 also demonstrates that for any even sine subchannel, the transmitted baseband pulse is $f(t - T/2)$, and in any odd cosine subchannel it is $f(t)$. Thus, for any $(k+L)^{th}$ sine subchannel the transmitted symbol may be represented as follows:

$$f_{sin,(k+L)}(t) = a_{k+L}f\left(t - \frac{T}{4}(1+(-1)^L)\right) \quad (A1.7)$$

where: a_{k+L} is the information symbol

The

corresponding modulated signal in the $(k+L)^{th}$ sine subchannel will be:

$$S_{Tx,cos,(k+L)}(t) = \sin(\omega_k+2\pi BL) \cdot a_{k+L}f\left(t - \frac{T}{4}(1+(-1)^L)\right) \quad (A1.8)$$

which in the frequency domain yields:

$$S_{Tx,sin,(k+L)}(\omega) = a_{k+L}\left(\frac{j}{2}\right)F(\omega+\omega_k+2\pi BL)\exp\left\{-j(\omega+\omega_k+2\pi BL)\frac{T}{4}(1+(-1)^L)\right\} - a_{k+L}\left(\frac{j}{2}\right)F(\omega-\omega_k-2\pi BL)\exp\left\{-j(\omega-\omega_k-2\pi BL)\frac{T}{4}(1+(-1)^L)\right\} \quad (A1.9)$$

This signal is transmitted via link with the transfer function $H(\omega)$ yields the received signal, whose spectrum is given by:

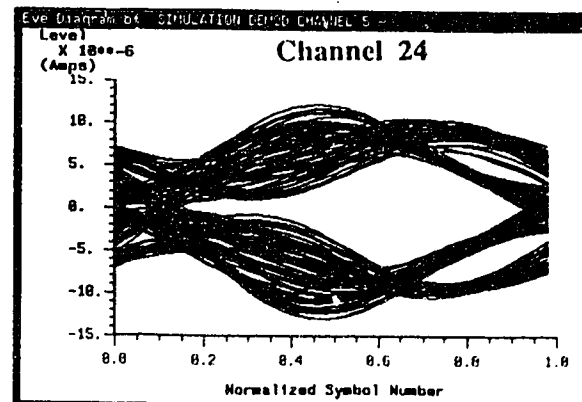
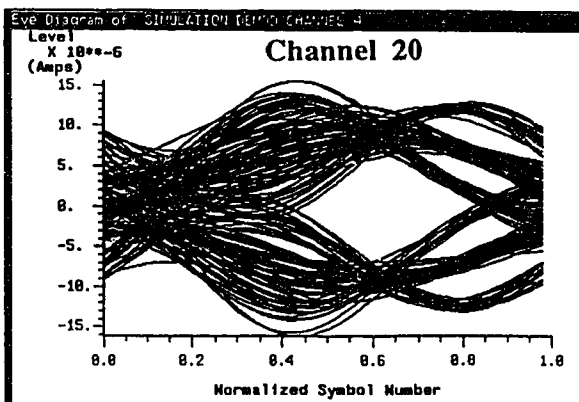
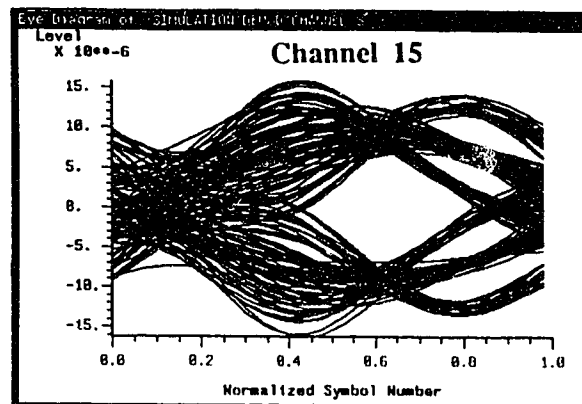
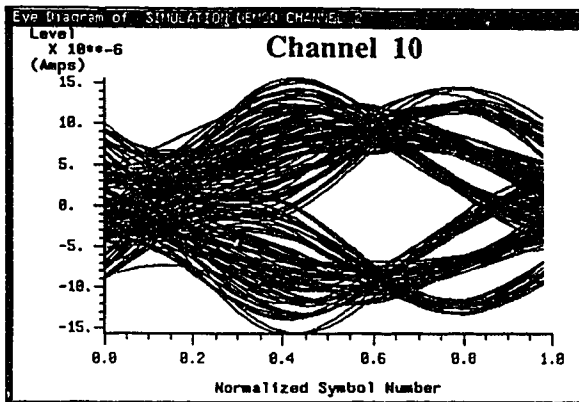
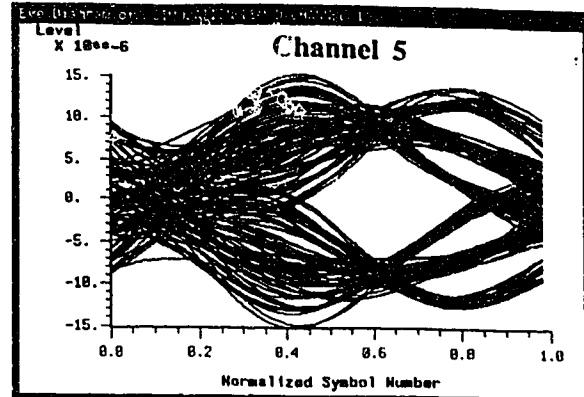
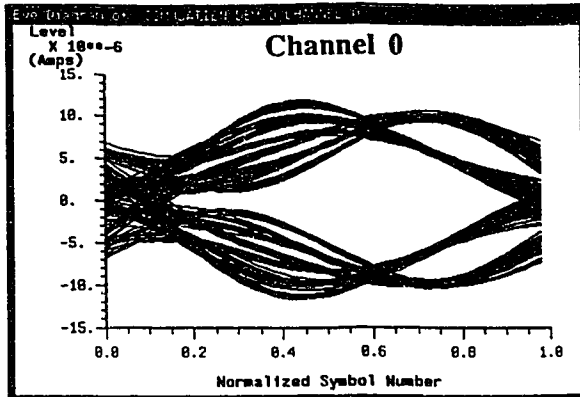
$$S_{Rx,sin,(k+L)}(\omega) = a_{k+L}\left(\frac{j}{2}\right)H(\omega)F(\omega+\omega_k+2\pi BL)\exp\left\{-j(\omega+\omega_k+2\pi BL)\frac{T}{4}(1+(-1)^L)\right\} - a_{k+L}\left(\frac{j}{2}\right)H(\omega)F(\omega-\omega_k-2\pi BL)\exp\left\{-j(\omega-\omega_k-2\pi BL)\frac{T}{4}(1+(-1)^L)\right\} \quad (A1.10)$$

This was given as (3.11a) in Section 3.2.1.

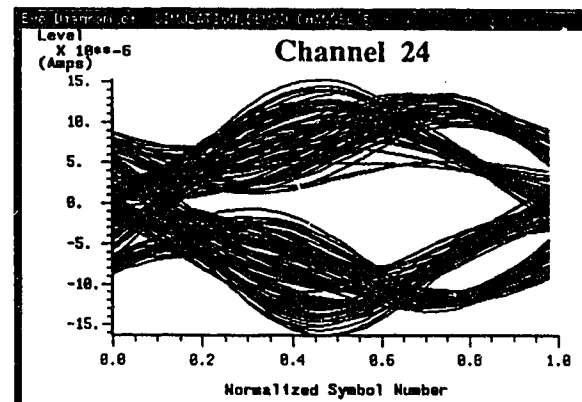
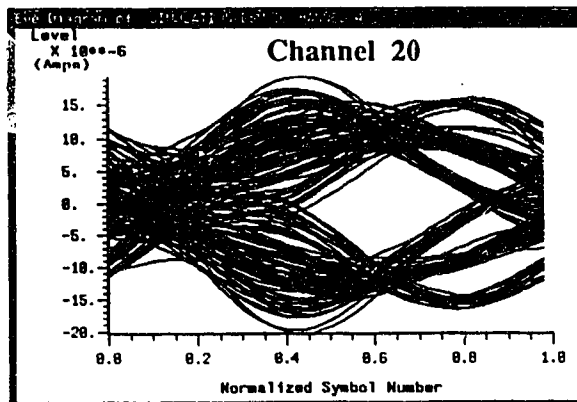
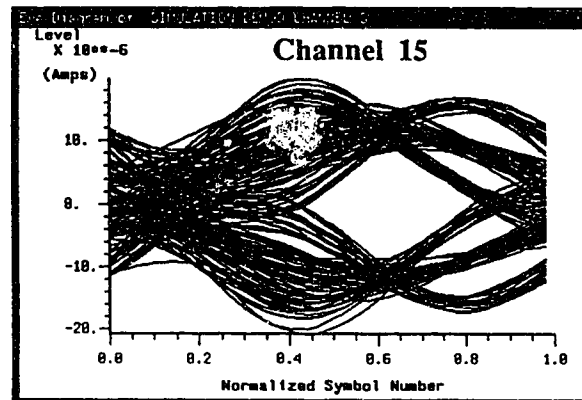
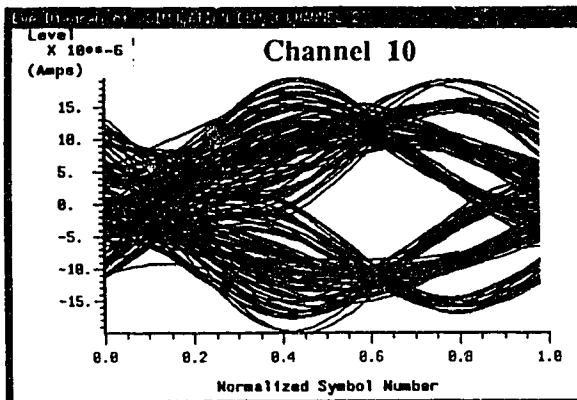
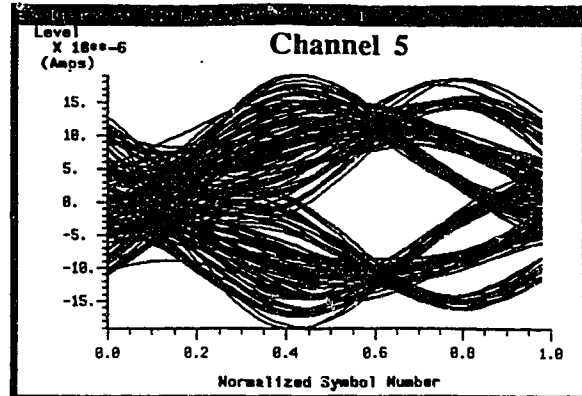
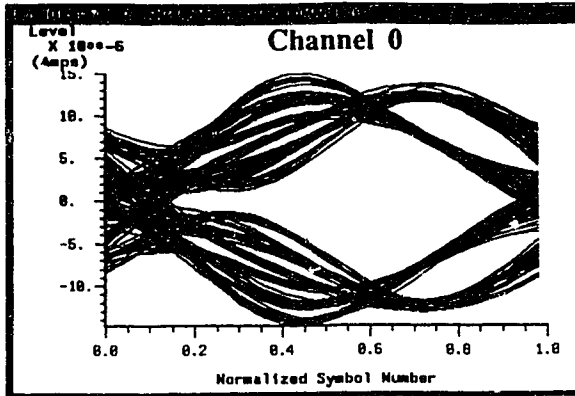
Appendix 2- Eye Diagrams for Determining MOD

This appendix gives eye diagrams for different MOD levels referenced from Section 4.2.1a to determine the maximum MOD level beyond which excessive distortion penalties are introduced. As explained in Section 4.2.1a, channels 0, 5, 10, 15, 20 and 24 were demodulated from a 25 channel modified orthogonally multiplexed payload (employing half sine shaped pulses) for each MOD. By simulating MOD levels of 0.05, 0.10, 0.15, ... 0.40, eight sets of demodulated channels were obtained. For MOD levels of 0.05, 0.10 and 0.15 no observable laser distortion was introduced, therefore they are not included here. The remaining sets of eye diagrams are presented on the following five pages, where the six channels from each MOD simulation are grouped together on the same page.

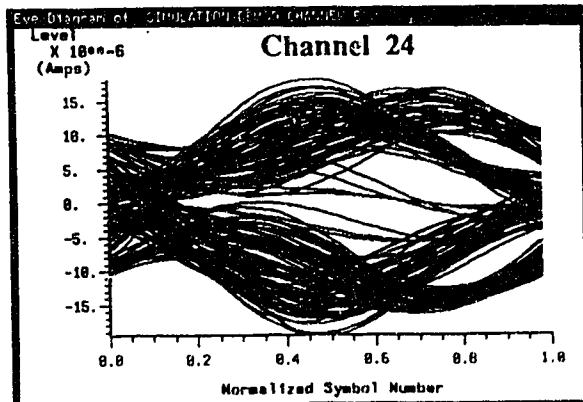
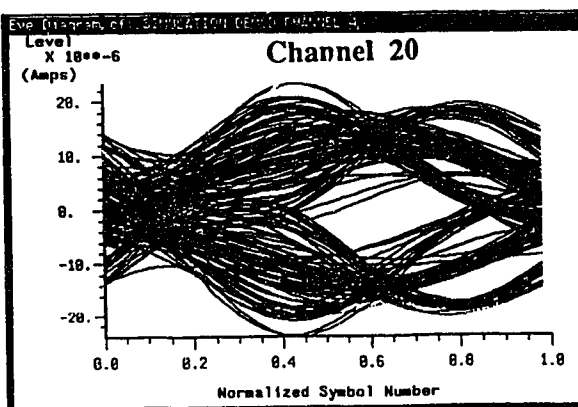
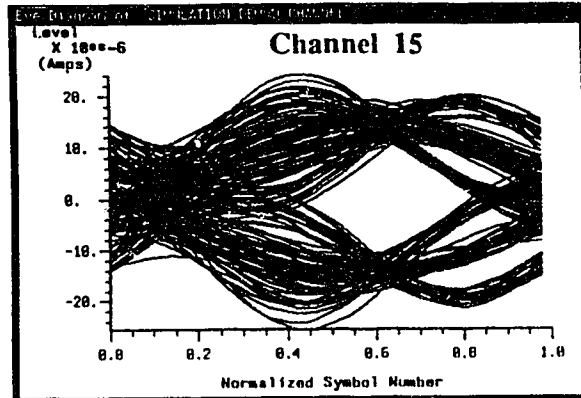
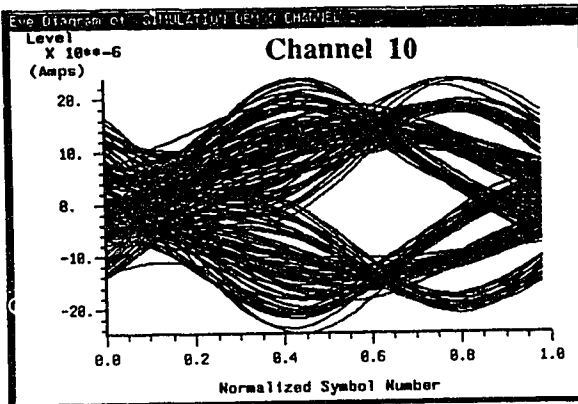
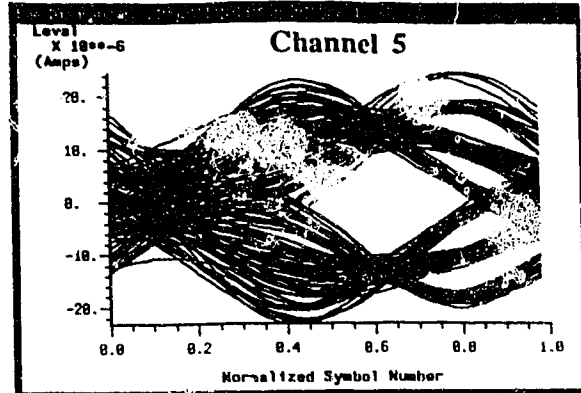
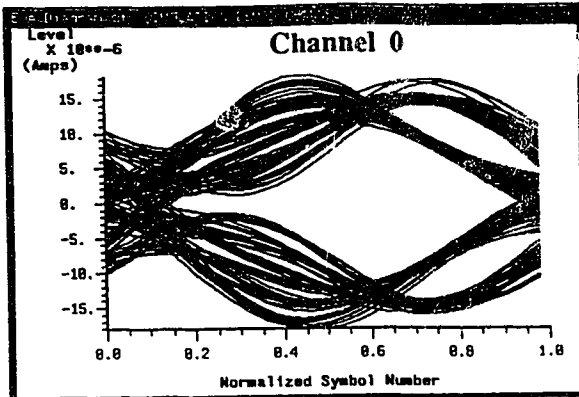
A2.1 Eye Diagrams with MOD= 0.20



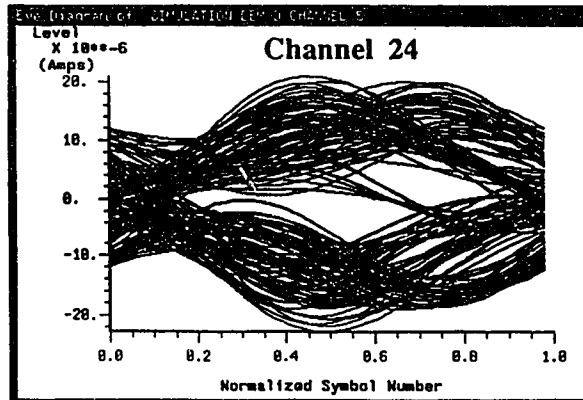
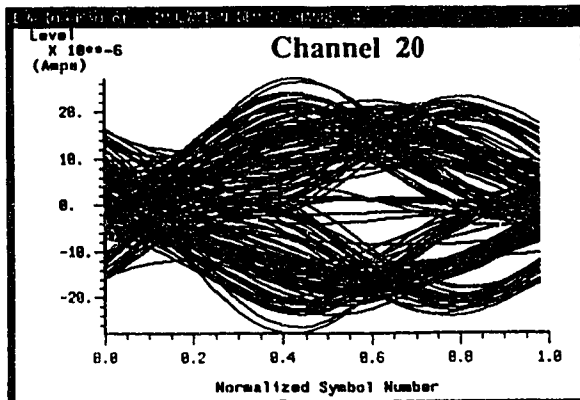
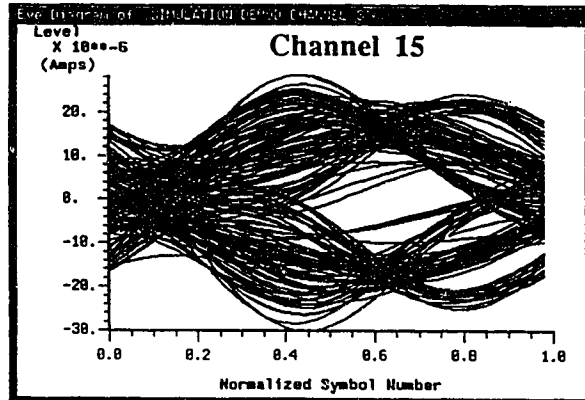
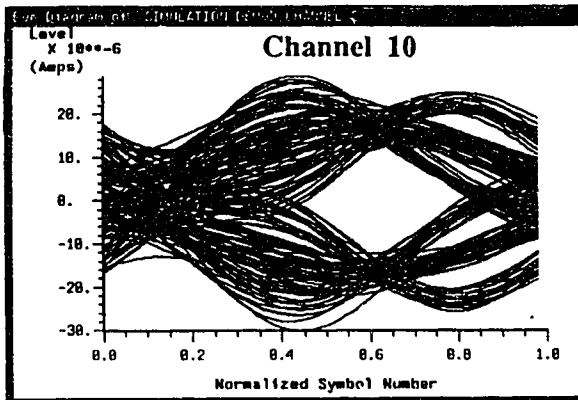
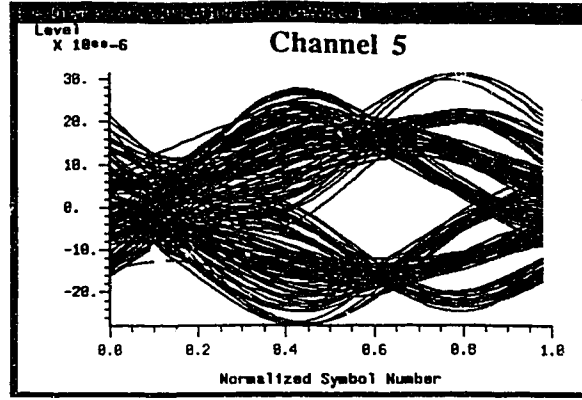
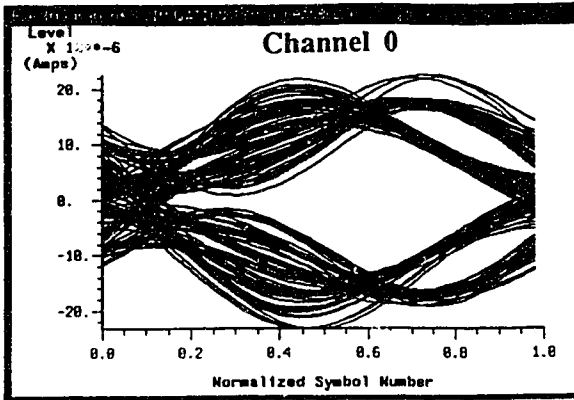
A2.2 Eye Diagrams with MOD= 0.25



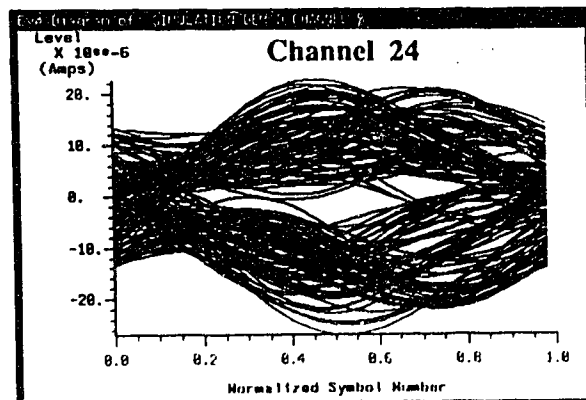
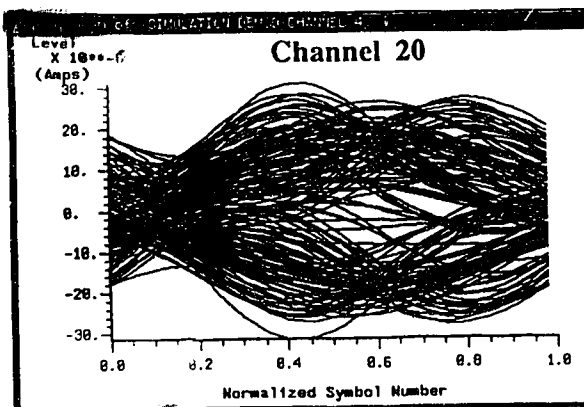
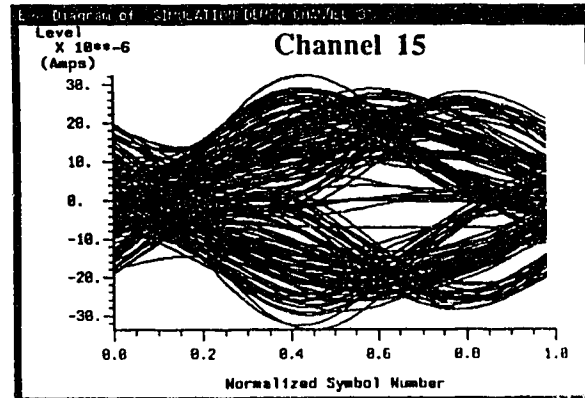
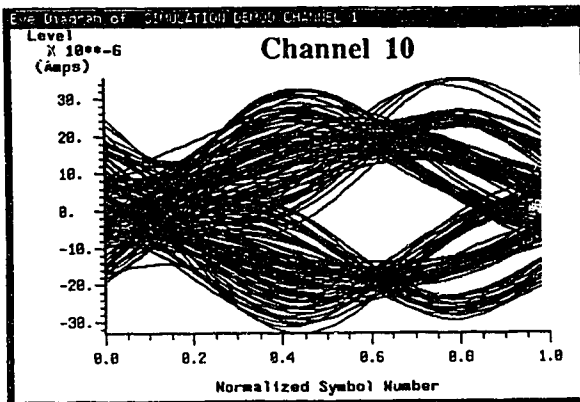
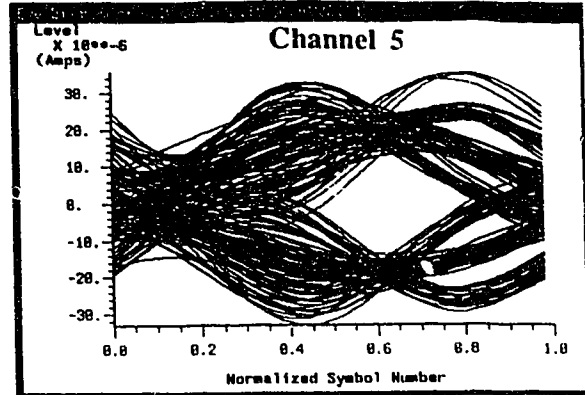
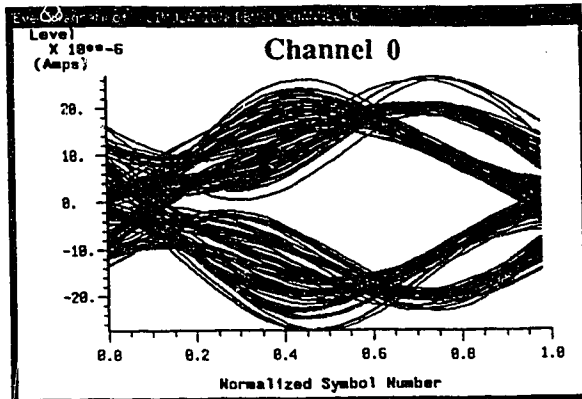
A2.3 Eye Diagrams with MOD= 0.30



A2.4 Eye Diagrams with MOD= 0.35



A2.5 Eye Diagrams with MOD= 0.40



Appendix 3- BOSS System Model of a 10 Gb/s Modified Orthogonal SCM Digital Lightwave Link Using Rectangular Shaped Pulses

This appendix gives the BOSS block diagrams and documentation for a fifty channel modified orthogonal SCM digital lightwave link employing rectangular modulating pulses and the laser resonance distortion model. This system gave the best performance in payload capacity simulations. All of the system simulation models in BOSS had a very similar structure, therefore only the one employing the rectangular shape is presented here.

In Section A3.1 the block diagram, description and parameter explanation of this system are presented along with the specific parameters for one simulation. The simulation described by these parameters was 500 symbols in duration. The sample intervals set at 6.25 psec and the symbol rate of 200 Mbit/s. All fifty channels were enabled, each having a current calculated from (4.4a) in Section 4.2.1 assuming $MOD= 0.20$ and ($I_{bias}= 7I_{thres} = 105$ mA). Note that any group of channels could be disabled simply by setting their group channel current to zero. The frequency position of the first channel was defined by "Fcarrier 1". The "Optical Scaling Coefficient" parameter was calculated in Section 2.2 by (2.38). "Samples of Delay" was the parameter used to adjust the downconversion local oscillators phase for each channel, because there was a time delay of 25 psec for all frequencies through the laser module. To select a channel for demodulation, the "Demod Channel Position" was specified by an integer, and the "LO Phase" had to match this channels carrier. Finally the receiver filter was defined and the output scaling coefficient was set to 1.

Presented in A3.2 is the BOSS module of a group of 10 modified orthogonally multiplexed channels. The parameters of this module are defined either as numerical values, or in terms of the simulation variables for the fifty channel system. The seed numbers for the random data generator in each channel of this group were selected from a

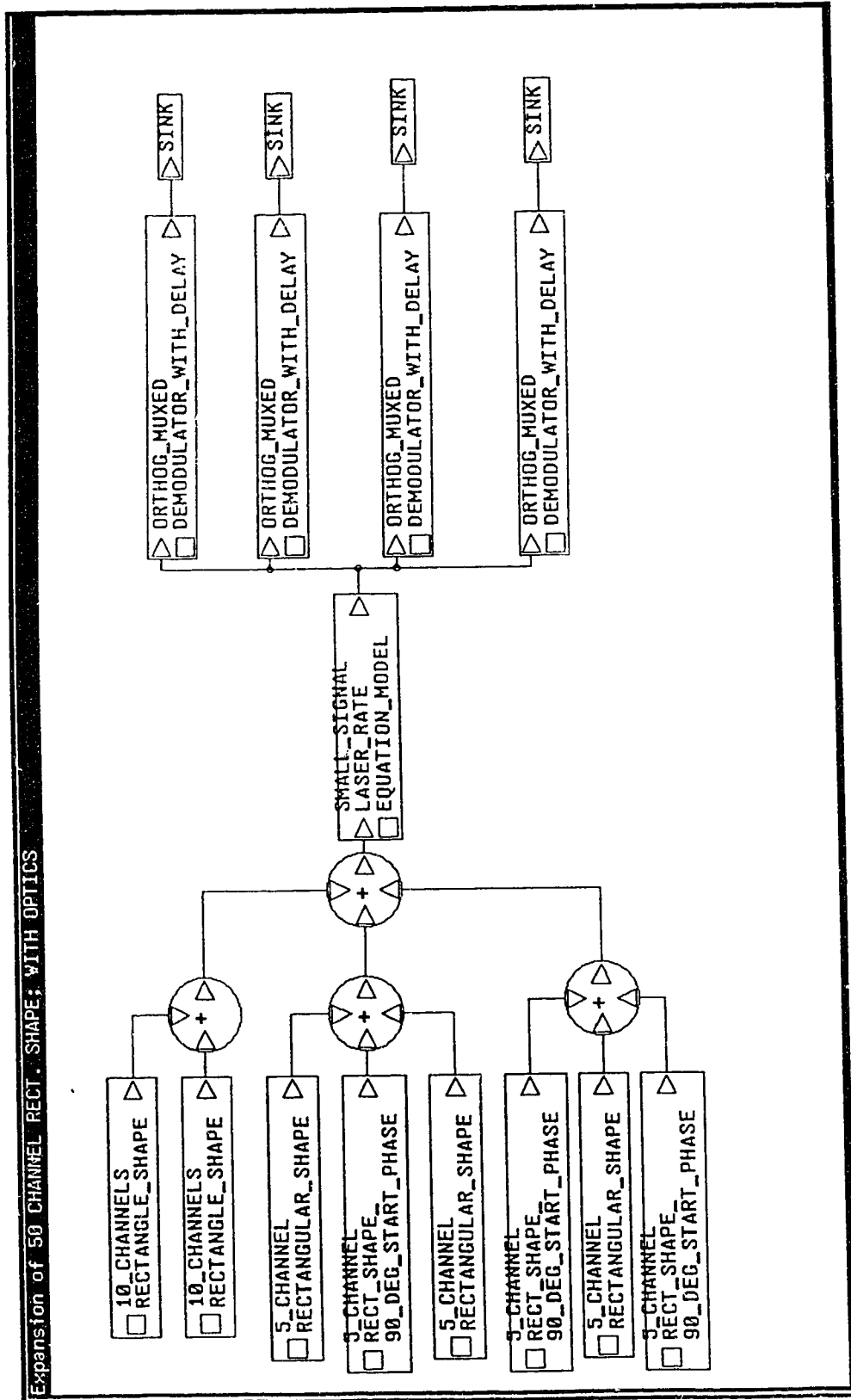
random digits table in [52]. The channel positions of each channel were defined in terms of the system variables "Fcarrier 1" and "Channel Spacing". The modules that make up "10_Channels Rectangular_Shape" are modules "5_Channel Rectangular Shape" and "5_Channel Rect_Shape 90_Deg_Start_Phase" which are described in Section A3.3.

In Section A3.3 is a description of the modules "5_Channel Rectangular Shape" and "5_Channel Rect_Shape 90_Deg_Start_Phase". These are simply a group of five modified orthogonally multiplexed channels employing rectangular shaped pulses with no quadrature subchannels present. The first channel of "5_Channel Rectangular Shape" is a sine carrier (ie phase is set to zero) while the first channel of "5_Channel Rect_Shape 90_Deg_Start_Phase" is a cosine carrier (ie. phase is set to 90°). Also given in this Section is a description of module "Rectangular Shape" which generates a single BPSK signal whose carrier phase and frequency are defined at a higher level in BOSS where channels are grouped together appropriately and create a modified orthogonally multiplexed signal.

The "small signal laser rate equation model" is presented in Section A3.4. Only the top level of this module is presented because the lower level BOSS modules are given and explained in Figures 2.2a, 2.2b, 2.2c and 2.2d.

The final component of the system, the "orthogonally multiplexed demodulator with delay" is presented in Section A3.5. This module performs a homodyne downconversion on the received photo-current by a phase matched local oscillator, and filters the result with a Butterworth low pass filter. The phase of the local oscillator was matched to the received signal by delaying the output of a sinusoidal oscillator by 25 psec. This delay was determined by trying different delays until the best result was obtained.

A3.1 System BOSS Block Diagram, Description and Parameters



STOP-TIME = 2.5E-6
DT = 6.25E-12
FCARRIER 1 = 4.0E8
CHANNEL SPACING = 2.0E8
CURRENT CHANNELS 0-9 = 0.0025456
CURRENT CHANNELS 10-19 = 0.0025456
CURRENT CHANNELS 20-24 = 0.0025456
CURRENT CHANNELS 25-29 = 0.0025456
CURRENT CHANNELS 30-34 = 0.0025456
CURRENT CHANNELS 35-39 = 0.0025456
CURRENT CHANNELS 40-44 = 0.0025456
CURRENT CHANNELS 45-49 = 0.0025456
DC BIAS CURRENT = 0.105
INITIAL INJECTION CURRENT = 0.105
INITIAL CARRIER DENSITY N = 2.12740002E24
INITIAL PHOTON DENSITY = 1.5480001E21
OPTICAL SCALING COEFFICIENT = 6.4E24
SAMPLES OF DELAY = 4
DEMODO CHANNEL POSITION 1 = 35
DEMODO CHANNEL POSITION 2 = 40
DEMODO CHANNEL POSITION 3 = 47
DEMODO CHANNEL POSITION 4 = 48
LO PHASE 1 = 1.5707963
LO PHASE 2 = 0.0
LO PHASE 3 = 1.5707963
LO PHASE 4 = 0.0
DEMODO FILTER BANDWIDTH = 1.35E8
DEMODO FILTER ORDER = 3
OUTPUT SCALING COEFFICIENT = 1.0

MODULE NAME: 50 CHANNEL RECT. SHAPE; WITH OPTICS
GROUP: SYSTEM
DATABASE: /home/suns/benterud/DROF-project/
AUTHOR: benterud
CREATION DATE: 28-Aug-1990 19:47:22

DESCRIPTION:

Fifty channel test with optics of an orthogonally multiplexed signal using rectangular shaped pulses without a quadrature component.

REVISIONS:

Author : benterud
Date : 28-Aug-1990 19:47:22
Description:

28-Aug-1990 19:47:28
Module CREATION.

INPUT SIGNALS:
(none)

OUTPUT SIGNALS:
(none)

PARAMETERS:

STOP-TIME Type: REAL
Lower Limit: 2.999998E-39
Upper Limit: 1.7E38

Specifies the maximum value of time for the simulation (in seconds).
The simulation clock runs from time=0.0 to time=STOP-TIME
in steps of DT, all in seconds.

DT Type: REAL
Lower Limit: 2.999998E-39
Upper Limit: 1.7E38

Time between discrete simulation signal samples (in seconds).
DT must be small enough to satisfy the Sampling
Theorem for all signals at all points in the simulation.

NOTE:

If the specified period or rate of a periodic function results

in a period that is not a multiple of DT, then BOSS will round the period to the nearest value that IS a multiple of DT.

For example, if $DT=0.125(\text{sec})$ and a rate was specified as $\text{rate}=1.4(\text{hz})$ which corresponds to a period of $T=0.714(\text{sec})$ which is $5.7*DT$, then BOSS will round this period to be $6.0*DT$ and thus the effective rate will be $1.333(\text{hz})$.

Because of this, the choice for DT can affect the periods of the periodic signals in the simulation.

```
-----
FCARRIER 1                                Type: REAL
Lower Limit: 0.0
Upper Limit: 1.7E38
```

The frequency of the generated sinusoidal tone in Hertz which is the center frequency of the desired channel allocation.

```
-----
CHANNEL SPACING                             Type: REAL
Lower Limit: 0.0
Upper Limit: 1.7E38
```

channel spacing

```
-----
CURRENT CHANNELS 0-9                       Type: REAL
Lower Limit: -1.7E38
Upper Limit: 1.7E38
```

output = gain constant * input

This is a scaling coefficient which converts the output signal of the modulated random data into a signal drive current which is fed into the laser

```
-----
CURRENT CHANNELS 10-19                    Type: REAL
Lower Limit: -1.7E38
Upper Limit: 1.7E38
```

output = gain constant * input

This is a scaling coefficient which converts the output signal of the modulated random data into a signal drive current which is fed into the laser

```
-----
CURRENT CHANNELS 20-24                    Type: REAL
Lower Limit: -1.7E38
```

Upper Limit: 1.7E38

output = gain constant * input

This is a scaling coefficient which converts the output signal of the modulated random data into a signal drive current which is fed into the laser

CURRENT CHANNELS 25-29

Type: REAL

Lower Limit: -1.7E38

Upper Limit: 1.7E38

output = gain constant * input

This is a scaling coefficient which converts the output signal of the modulated random data into a signal drive current which is fed into the laser

CURRENT CHANNELS 30-34

Type: REAL

Lower Limit: -1.7E38

Upper Limit: 1.7E38

output = gain constant * input

This is a scaling coefficient which converts the output signal of the modulated random data into a signal drive current which is fed into the laser

CURRENT CHANNELS 35-39

Type: REAL

Lower Limit: -1.7E38

Upper Limit: 1.7E38

output = gain constant * input

This is a scaling coefficient which converts the output signal of the modulated random data into a signal drive current which is fed into the laser

CURRENT CHANNELS 40-44

Type: REAL

Lower Limit: -1.7E38

Upper Limit: 1.7E38

output = gain constant * input

This is a scaling coefficient which converts the output signal of the modulated random data into a signal drive current which is fed into the laser

CURRENT CHANNELS 45-49
Lower Limit: -1.7E38
Upper Limit: 1.7E38

Type: REAL

output = gain constant * input

This is a scaling coefficient which converts the output signal of the modulated random data into a signal drive current which is fed into the laser

DC BIAS CURRENT
Lower Limit: -1.7E38
Upper Limit: 1.7E38

Type: REAL

This is the value to be output by the module and is the dc bias current for the laser which is constant throughout the simulation.

INITIAL INJECTION CURRENT
Lower Limit: 0.0
Upper Limit: 1.7E38

Type: REAL

Initial value for unit delay. This value will be the output of the unit delay precisely the first time the module is executed.

INITIAL CARRIER DENSITY N
Lower Limit: 0.0
Upper Limit: 1.7E38

Type: REAL

Initial value for unit delay. This value will be the output of the unit delay precisely the first time the module is executed. This value will be pre-defined by user as the initial carrier density, $N(0)$.

INITIAL PHOTON DENSITY
Lower Limit: 0.0
Upper Limit: 1.7E38

Type: REAL

Initial value for unit delay. This value will be the output of the unit delay precisely the first time the module is executed. This initial value of photon density must be consistent with the other input parameters, if it is not, the result will be erroneous.

OPTICAL SCALING COEFFICIENT
Lower Limit: 0.0
Upper Limit: 1.7E38

Type: REAL

This is the scaling coefficient to translate the average photon density to the expected received photo current at the receiver.

SAMPLES OF DELAY Type: INTEGER
Lower Limit: 0
Upper Limit: 2147483647

Is the number of simulation samples that the local oscillator is to be delayed to match the absolute time delay that is introduced by passing the signal through the laser.

DEMOD CHANNEL POSITION 1 Type: INTEGER
Lower Limit: 0
Upper Limit: 2147483647

demod channel position 1

DEMOD CHANNEL POSITION 2 Type: INTEGER
Lower Limit: 0
Upper Limit: 2147483647

demod channel position 2

DEMOD CHANNEL POSITION 3 Type: INTEGER
Lower Limit: 0
Upper Limit: 2147483647

demod channel position 3

DEMOD CHANNEL POSITION 4 Type: INTEGER
Lower Limit: 0
Upper Limit: 2147483647

demod channel position 4

LO PHASE 1 Type: REAL
Lower Limit: -1.7E38
Upper Limit: 1.7E38

The phase of the generated sinusoidal tone in radians.

LO PHASE 2 Type: REAL

Lower Limit: -1.7E38

Upper Limit: 1.7E38

The phase of the generated sinusoidal tone in radians.

LO PHASE 3 Type: REAL

Lower Limit: -1.7E38

Upper Limit: 1.7E38

The phase of the generated sinusoidal tone in radians.

LO PHASE 4 Type: REAL

Lower Limit: -1.7E38

Upper Limit: 1.7E38

The phase of the generated sinusoidal tone in radians.

DEMOD FILTER BANDWIDTH Type: REAL

Lower Limit: 2.99E-39

Upper Limit: 1.7E38

3 db bandwidth (single sided) of lowpass filter (Hertz) which is used to remove all higher frequency components that are produced by down-conversion.

DEMOD FILTER ORDER Type: INTEGER

Lower Limit: 0

Upper Limit: 2147483647

Order of filter.

OUTPUT SCALING COEFFICIENT Type: REAL

Lower Limit: -1.7E38

Upper Limit: 1.7E38

output = gain constant * input

MODULES USED IN BLOCK DIAGRAM:

ADDER

3 INPUT ADDER

10 CHANNELS RECTANGLE_SHAPE

5 CHANNEL RECTANGULAR_SHAPE

5 CHANNEL RECT_SHAPE_90_DEG_START_PHASE

SINK
SMALL SIGNAL LASER RATE EQUATION_MODEL
ORTHO_G_MUXED DEMODULATOR_WITH_DELAY

INITIALIZATION CODE:
(none)

A3.2 Description of 10 Channel Groups in BOSS

10_CHANNEL RECTANGLE_SHAPE Page 1

13-Nov-1990 2:25:37

MODULE NAME: 10_CHANNEL RECTANGLE_SHAPE
GROUP: DIGITAL SOURCES // *INTERNALS*
DATABASE: /home/suns/benterud/DROF-project/
AUTHOR: benterud
CREATION DATE: 9-Nov-1990 14:10:28

DESCRIPTION:

This module contains two groups of five channel clusters of modified orthogonal subcarrier multiplexed channels. The rectangular baseband pulse shape is employed. No quadrature subchannels are present.

The tributary data streams are operating at 200 Mbit/s and the signalling period are aligned in time. Carriers are spaced by the parameter "channel spacing" which must be set at 200 MHz for the modified orthogonal subcarrier multiplexing technique to work. The phase of adjacent carriers are offset by 90 degrees to its neighbour, ie sine, cosine, sine carriers.

REVISIONS:

Author : benterud
Date : 9-Nov-1990 14:10:28
Description:

9-Nov-1990 14:11:08
Module CREATION.

INPUT SIGNALS:
(none)

OUTPUT SIGNALS:

FIVE SINESHAPED BPSK'S Type: REAL
Lower Limit: -1.7E38
Upper Limit: 1.7E38

This module outputs 5 individual channels each sourcing a 200 Mbit/s pulse sequence modulating a carrier. The pulse shape is rectangular and the signalling is antipodal, ie it takes on values of +1 or -1. The carriers are spaced according to the parameter "channel spacing" and alternate sine, cosine, sine, etc. Channel spacing must be set to 200 MHz for the modified orthogonal SCM configuration to work. No quadrature subchannels are present.

PARAMETERS:

FCARRIER 1 Type: REAL
 Lower Limit: 0.0
 Upper Limit: 1.7E38

The frequency of the generated sinusoidal tone in Hertz which is the center frequency of the desired channel allocation.

CHANNEL SPACING Type: REAL
 Lower Limit: 0.0
 Upper Limit: 1.7E38

channel spacing

CHANNEL CURRENT Type: REAL
 Lower Limit: -1.7E38
 Upper Limit: 1.7E38

output = gain constant * input
 This is a scaling coefficient which converts the output signal of the modulated random data into a signal drive current which is fed into the laser

PROBABILITY OF FALSE Type: REAL
 Lower Limit: 0.0
 Upper Limit: 1.0

Probability the the output will be a .false.

ISFED1 Type: INTEGER
 Lower Limit: 1
 Upper Limit: 2147483647

Initial seed for the uniform random number generator. Should be a large odd integer.

ISEED2 Type: INTEGER
 Lower Limit: 1
 Upper Limit: 2147483647

Initial seed for the uniform random number generator. Should be a large odd integer.

ISEED3 Type: INTEGER
 Lower Limit: 1

Upper Limit: 2147483647

Initial seed for the uniform random number generator. Should be a large odd integer.

ISEED4 Type: INTEGER
Lower Limit: 1
Upper Limit: 2147483647

Initial seed for the uniform random number generator. Should be a large odd integer.

ISEED5 Type: INTEGER
Lower Limit: 1
Upper Limit: 2147483647

Initial seed for the uniform random number generator. Should be a large odd integer.

ISEED6 Type: INTEGER
Lower Limit: 1
Upper Limit: 2147483647

Initial seed for the uniform random number generator. Should be a large odd integer.

ISEED7 Type: INTEGER
Lower Limit: 1
Upper Limit: 2147483647

Initial seed for the uniform random number generator. Should be a large odd integer.

ISEED8 Type: INTEGER
Lower Limit: 1
Upper Limit: 2147483647

Initial seed for the uniform random number generator. Should be a large odd integer.

ISEED9 Type: INTEGER
Lower Limit: 1
Upper Limit: 2147483647

Initial seed for the uniform random number generator. Should be a large odd integer.

ISEED10 Type: INTEGER
Lower Limit: 1
Upper Limit: 2147483647

Initial seed for the uniform random number generator. Should
be a large odd integer.

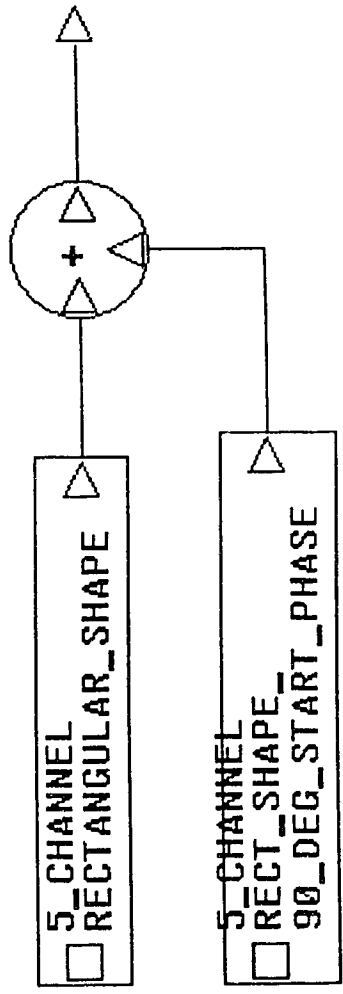
MODULES USED IN BLOCK DIAGRAM:

ADDER
5_CHANNEL RECTANGULAR_SHAPE
5_CHANNEL RECT_SHAPE_90_DEG_START_PHASE

INITIALIZATION CODE:

(none)

10_CHANNEL_RECTANGLE_SHAPE



A3.3 Description of Single and 5 Channel Groups in BOSS

FIVE CHANNEL RECTANGLE SHAPE Page 1

13-Nov-1990 2:36:11

MODULE NAME: FIVE CHANNEL RECTANGLE SHAPE
GROUP: DIGITAL SOURCES // *INTERNAL*
DATABASE: /home/suns/benterud/DROF-project/
AUTHOR: benterud
CREATION DATE: 13-Nov-1990 2:34:35

DESCRIPTION:

This module outputs 5 individual channels each sourcing a 200 Mbit/s pulse sequence modulating a carrier. The pulse shape is rectangular and the signalling is antipodal, ie it takes on values of +1 or -1. The carriers are spaced according to the parameter "channel spacing" and alternate sine, cosine, sine, etc. Channel spacing must be set to 200 MHz for the modified orthogonal SCM configuration to work. No quadrature subchannels are present.

REVISIONS:

Author : benterud
Date : 13-Nov-1990 2:34:35
Description:

13-Nov-1990 2:35:20
Module CREATION.

INPUT SIGNALS:
(none)

OUTPUT SIGNALS:

FIVE SINESHAPED BPSK'S Type: REAL
Lower Limit: -1.7E38
Upper Limit: 1.7E38

This module outputs five sineshaped BPSK random data channels which are modulated up at carrier frequencies specified by the exported carrier frequency parameters.

PARAMETERS:

FCARRIER 1 Type: REAL
Lower Limit: 0.0

Upper Limit: 1.7E38

The frequency of the generated sinuaoidal tone in Hertz
which is the center frequency of the desired channel alloca
tion.

CHANNEL SPACING Type: REAL
Lower Limit: 0.0
Upper Limit: 1.7E38

channel spacing

CHANNEL CURRENT Type: REAL
Lower Limit: -1.7E38
Upper Limit: 1.7E38

output = gain constant * input

This is a scaling coefficient which converts the
output signal of the modulated random data into a signal
drive current which is fed into the laser

PROBABILITY OF FALSE Type: REAL
Lower Limit: 0.0
Upper Limit: 1.0

Probability the the output will be a .false.

ISEED1 Type: INTEGER
Lower Limit: 1
Upper Limit: 2147483647

Initial seed for the uniform random number generator. Should
be a large odd integer.

ISEED2 Type: INTEGER
Lower Limit: 1
Upper Limit: 2147483647

Initial seed for the uniform random number generator. Should
be a large odd integer.

ISEED3 Type: INTEGER
Lower Limit: 1
Upper Limit: 2147483647

Initial seed for the uniform random number generator. Should

be a large odd integer.

ISEED4
Lower Limit: 1
Upper Limit: 2147483647

Type: INTEGER

Initial seed for the uniform random number generator. Should
be a large odd integer.

ISEED5
Lower Limit: 1
Upper Limit: 2147483647

Type: INTEGER

Initial seed for the uniform random number generator. Should
be a large odd integer.

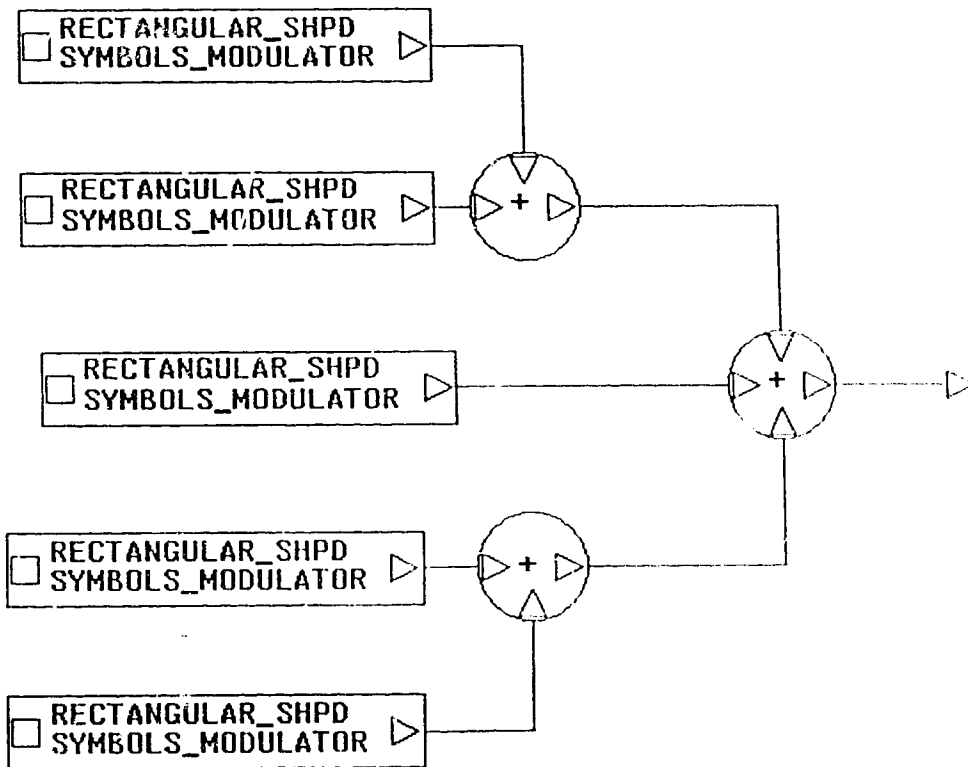
MODULES USED IN BLOCK DIAGRAM:

ADDER
3 INPUT ADDER
RECTANGULAR_SHAPE_SYMBOLS_MODULATOR

INITIALIZATION CODE:

(none)

5_CHANNEL RECTANGULAR_SHAPE



MODULE NAME: 5_CHANNEL_RECT_SHAPE_90_DEG_START_PHASE
GROUP: DIGITAL SOURCES
DATABASE: /home/suns/benterud/DROF-project/
AUTHOR: benterud
CREATION DATE: 28-Aug-1990 16:21:25

DESCRIPTION:

This module outputs 5 individual channels each sourcing a 200 Mbit/s pulse sequence modulating a carrier. The pulse shape is rectangular and the signalling is antipodal, ie it takes on values of +1 or -1. The carriers are spaced according to the parameter "channel spacing" and alternate sine, cosine, sine, etc. Channel spacing must be set to 200 MHz for the modified orthogonal SCM configuration to work. No quadrature subchannels are present.

The phase of the first carrier in this group is 90 degrees

REVISIONS:

Author : benterud
Date : 18-Oct-1990 21:05:01
Description:

Edited 18-Oct-1990 21:05:01, No Edit Description Entered.

Author : benterud
Date : 18-Oct-1990 21:04:15
Description:

18-Oct-1990 21:04:15
This Save done with Checker Off.

Author : benterud
Date : 28-Aug-1990 16:21:25
Description:

28-Aug-1990 16:22:02
Module CREATION.

INPUT SIGNALS:
(none)

OUTPUT SIGNALS:

FIVE SINESHAPED BPSK'S

Type: REAL

MODULE NAME: RECTANGULAR SHAPE
GROUP: DIGITAL SOURCES // *INTERNALS*
DATABASE: /home/suns/benterud/DROF-project/
AUTHOR: benterud
CREATION DATE: 12-Oct-1990 11:27:58

DESCRIPTION:

This module outputs a BPSK modulated random data signal ~~which has been "prefiltered" by raised cosine multiplication.~~ This filtered baseband data has been multiplied up in frequency to $f_{carrier}$, which is specified by the an exported parameter. The seed for the random data is also exported, for the option of having different seeds for different channels to ensure uncorrelated data.

REVISIONS:

Author : benterud
Date : 12-Oct-1990 11:27:58
Description:

12-Oct-1990 11:28:31
Module CREATION.

INPUT SIGNALS:
(none)

OUTPUT SIGNALS:

SINE SHAPED BPSK OUTPUT Type: REAL
Lower Limit: -1.7E38
Upper Limit: 1.7E38

This output is a random bit stream which has been shaped by a cosine multiplier for filtering purposes and multiplied up in frequency to the desired carrier frequency specified by an imported parameter "carrier". The output is scaled by the gain which converts the signal to a modulating current that drives the laser.

PARAMETERS:

FCARRIER Type: REAL
Lower Limit: 0.0
Upper Limit: 1.7E38

The frequency of the generated sinusoidal tone in Hertz which is the center frequency of the desired channel allocation.

CARRIER PHASE Type: REAL
 Lower Limit: -1.7E38
 Upper Limit: 1.7E38

The phase of the generated sinusoidal tone in radians.

ISEED Type: INTEGER
 Lower Limit: 1
 Upper Limit: 2147483647

Initial seed for the uniform random number generator. Should be a large odd integer.

CHANNEL CURRENT Type: REAL
 Lower Limit: -1.7E38
 Upper Limit: 1.7E38

output = gain constant * input

This is a scaling coefficient which converts the output signal of the modulated random data into a signal drive current which is fed into the laser

PROBABILITY OF FALSE Type: REAL
 Lower Limit: 0.0
 Upper Limit: 1.0

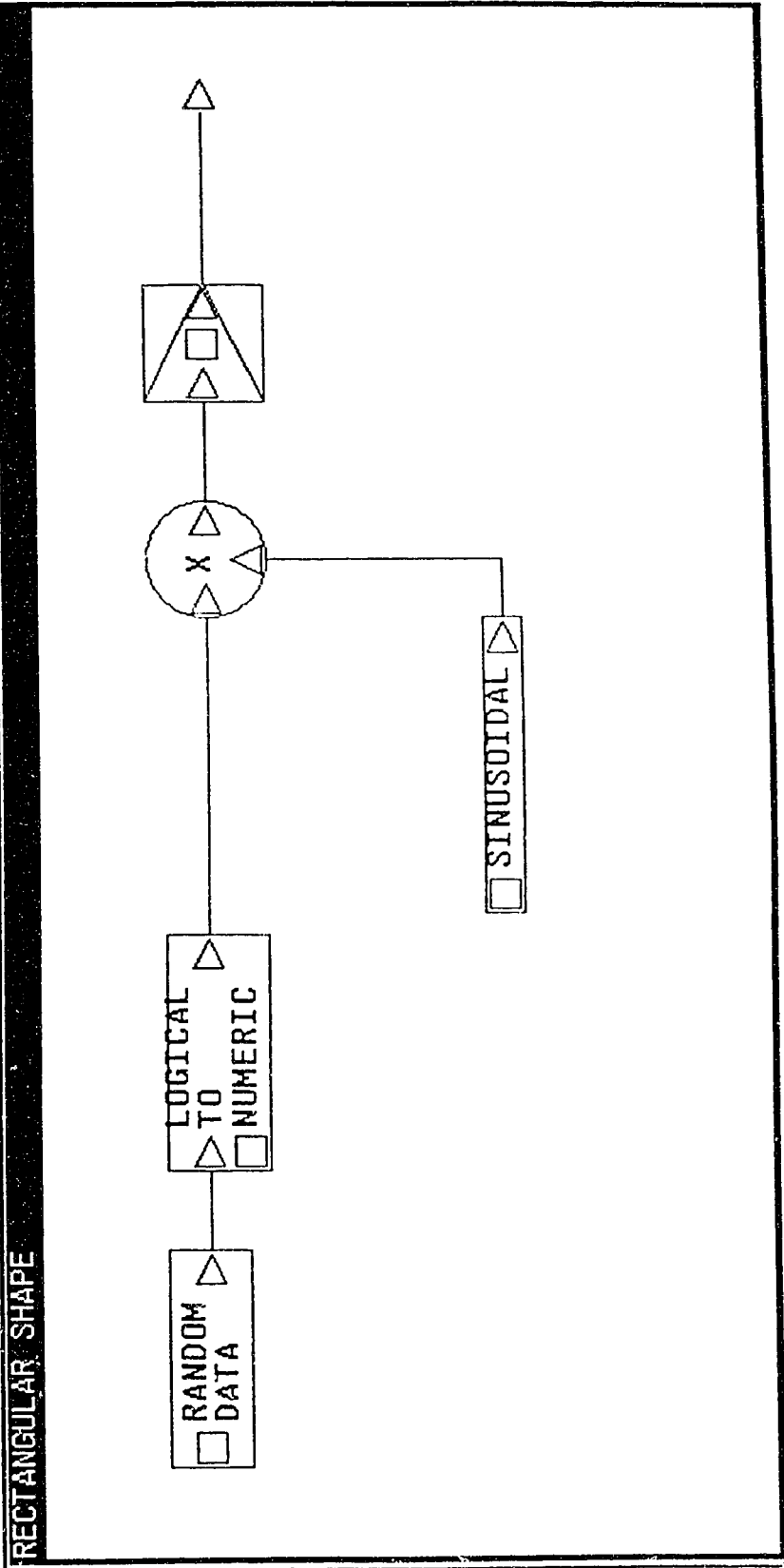
Probability the the output will be a .false.

MODULES USED IN BLOCK DIAGRAM:

RANDOM DATA
 LOGICAL TO NUMERIC
 GAIN
 SINUSOIDAL
 MULTIPLIER

INITIALIZATION CODE:

(none)



A3.4 Description of Laser Model in BOSS

SMALL_SIGNAL LASER_RATE EQUATION_MODEL Page 1

MODULE NAME: SMALL_SIGNAL LASER_RATE EQUATION_MODEL
GROUP: ANALOG MODULATORS
DATABASE: /home/suns/benterud/DROF-project/
AUTHOR: benterud
CREATION DATE: 28-Aug-1990 19:10:11

DESCRIPTION:

THIS IS A LASER DISTORTION MODULE BASED ON THE RATE EQUATIONS. The parameters entered at the simulation level will determine the characteristics of the laser, thus the threshold current of the laser. Therefore it is necessary to export the bias current and the lasers parameters up to the system level, and hence will be specified at that level. The laser parameters used were those measured by Tucker as described in the thesis; chapter 4.

The output of the photon density is scaled by the optical scaling coefficient defined as one of the module parameters.

REVISIONS:

Author : benterud
Date : 28-Aug-1990 19:15:11
Description:

28-Aug-1990 19:10:52
Module CREATION.

INPUT SIGNALS:

LASER SIGNAL DRIVE CURRENT Type: REAL
Lower Limit: -1.7E38
Upper Limit: 1.7E38

Is the a.c. input signal to the laser, and must be a current in amps. The laser is biased on at DC LASER BIAS, therefore the input signal magnitude must not be larger than this bias. If the current magnitude is close to the bias current level, severe distortions will result! So ensure that the laser is biased well above the magnitude of any incoming signal.

OUTPUT SIGNALS:

NORMALIZED OUTPUT PHOTON DENSITY Type: REAL

Lower Limit: 0.0
Upper Limit: 1.7E38

This is the photon density internal to the laser, normalized by the photon scaling coefficient. By choosing this scaling coefficient properly, the output power of the laser can be arbitrarily chosen.

PARAMETERS:

DC BIAS CURRENT Type: REAL
Lower Limit: -1.7E38
Upper Limit: 1.7E38

This is the value to be output by the module and is the dc bias current for the laser which is constant throughout the simulation.

INITIAL INJECTION CURRENT Type: REAL
Lower Limit: 0.0
Upper Limit: 1.7E38

Initial value for unit delay. This value will be the output of the unit delay precisely the first time the module is executed.

INITIAL CARRIER DENSITY Type: REAL
Lower Limit: 0.0
Upper Limit: 1.7E38

Initial value for unit delay. This value will be the output of the unit delay precisely the first time the module is executed. This value will be pre-defined by user as the initial carrier density, $N(0)$.

INITIAL PHOTON DENSITY Type: REAL
Lower Limit: 0.0
Upper Limit: 1.7E38

Initial value for unit delay. This value will be the output of the unit delay precisely the first time the module is executed. This initial value of photon density must be consistent with the other input parameters, if it is not, the result will be erroneous.

OPTICAL SCALING COEFFICIENT Type: REAL
Lower Limit: 0.0
Upper Limit: 1.7E38

This is the scaling coefficient to translate the average photon density to the expected received photo current at the receiver.

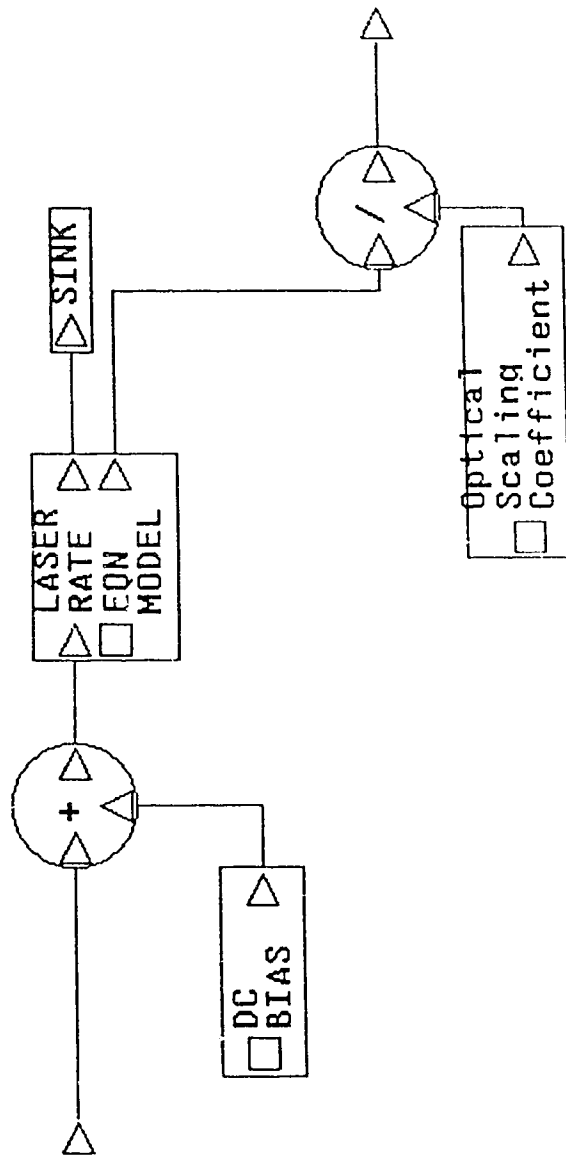
MODULES USED IN BLOCK DIAGRAM:

SINK
ADDER
CONST GEN
DIVIDER
LASER RATE EQN MODEL

INITIALIZATION CODE:

(none)

SMALL_SIGNAL_LASER_RATE_EQUATION_MODEL



A3.4 Description of Demodulator in BOSS

ORTHOX_MUXED DEMODULATOR_WITH_DELAY

Page 1

29-Oct-1990

MODULE NAME: ORTHOG_MUXED DEMODULATOR_WITH_DELAY
GROUP: DEMODULATORS
DATABASE: /home/suns/benterud/DROF-project/
AUTHOR: benterud
CREATION DATE: 28-Aug-1990 18:55:04

DESCRIPTION:

The channel of interest may be examined by choosing a carrier demodulation frequency the same as the center frequency of the channel of interest. Since homodyne demodulation is assumed the output symbols may be observed by simply removing any of the higher frequencies by a lowpass Butterworth filter. The local oscillator is delayed by a number of samples specified by the user to compensate for any absolute time delay introduced onto the information signal.

REVISIONS:

Author : benterud
Date : 28-Aug-1990 18:55:04
Description:

28-Aug-1990 18:55:47
Module CREATION.

INPUT SIGNALS:

DOWNCONVERT INPUT Type: REAL
Lower Limit: -1.7E38
Upper Limit: 1.7E38

This input is a wideband signal which is downconverted by a delayed sinusoid and filtered by an output LPF.

OUTPUT SIGNALS:

DOWNCONVERT OUTPUT Type: REAL
Lower Limit: -1.7E38
Upper Limit: 1.7E38

This is the downconverted and LPF'd signal of the input signal.

PARAMETERS:

DEMOM FREQ Type: REAL
Lower Limit: 0.0
Upper Limit: 1.7E38

The frequency of the generated sinuoidal tone in Hertz and
is the carrier used to demodulate the channel of interest

DEMOM CARRIER PHASE Type: REAL
Lower Limit: -1.7E38
Upper Limit: 1.7E38

The phase of the generated sinusoidal tone in radians.

SAMPLES OF DELAY Type: INTEGER
Lower Limit: 0
Upper Limit: 2147483647

Is the number of simulation samples that the local
oscillator is to be delayed to match the absolute time
delay that is introduced by passing the signal through the
laser.

DEMOM FILTER BANDWIDTH Type: REAL
Lower Limit: 2.999998E-39
Upper Limit: 1.7E38

3 db bandwidth (single sided) of lowpass filter (Hertz) whi
ch is used to remove all higher frequency components that
are produced by down-conversion.

DEMOM FILTER ORDER Type: INTEGER
Lower Limit: 0
Upper Limit: 2147483647

Order of filter.

OUTPUT SCALING COEFFICIENT Type: REAL
Lower Limit: -1.7E38
Upper Limit: 1.7E38

output = gain constant * input

MODULES USED IN BLOCK DIAGRAM:
MULTIPLIER

GAIN
BUTWTH FILTER (REAL)
DELAYED LOCAL OSCILLATOR
CONST GEN

INITIALIZATION CODE:

(none)

ORTHOG_MUXED_DEMODULATOR_WITH_DELAY

